

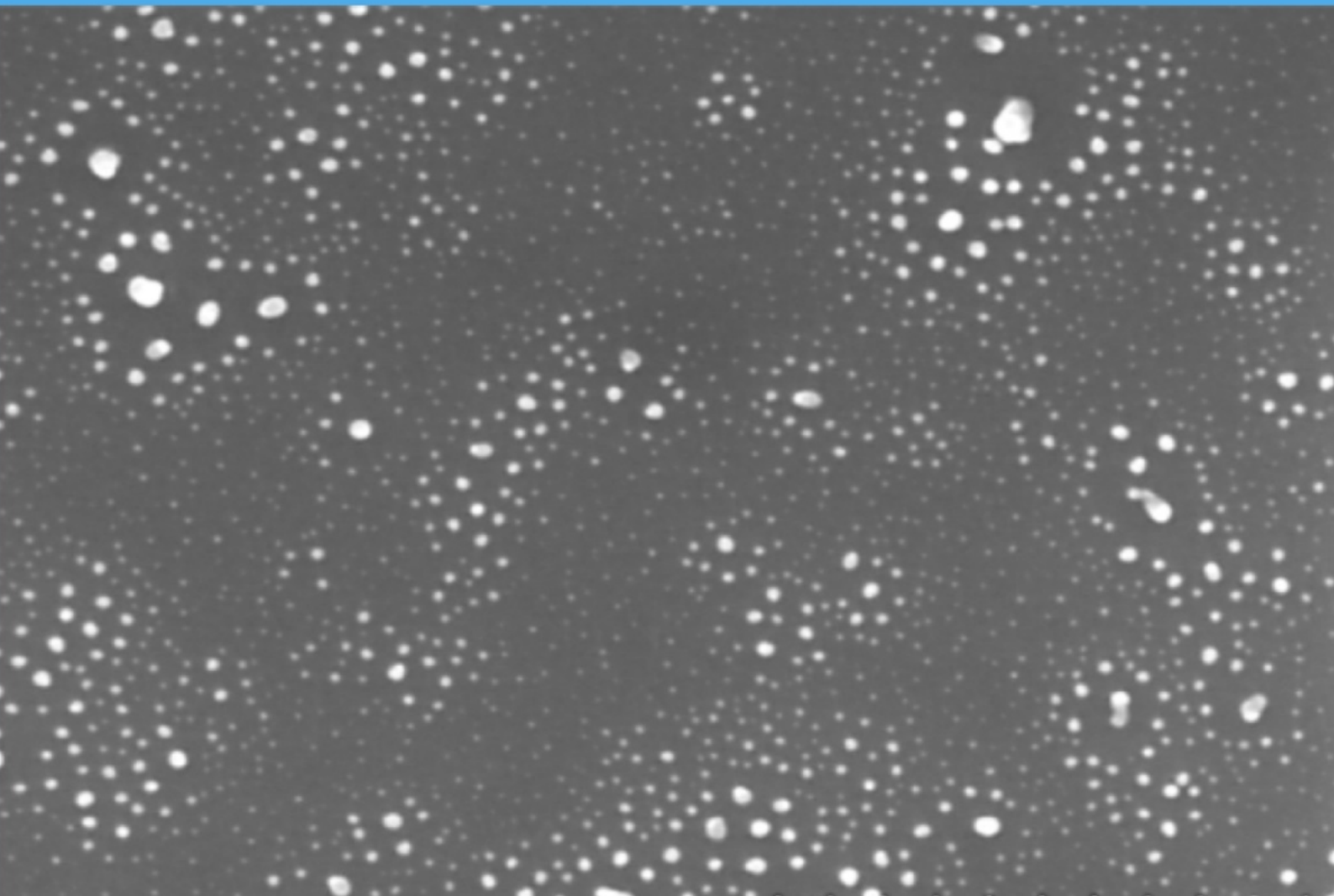
Metal-oxide Nanoparticle- based CO₂ gas sensor

Via Spark Ablation

Xuanzi He

Master of Material Science and Engineering

January 2025



Metal-oxide Nanoparticle-based CO₂ gas sensor

Via Spark Ablation

by

Xuanzi He

Student Name	Student Number
Xuanzi He	5704049

Project Duration: January, 2024 - January, 2025
Faculty: Faculty of Mechanical Engineering, Delft
Thesis committee: Dr. ir. S. Vollebregt
Dr. Peyman Taheri
Dr. Leandro Sacco
Dr. ir. Prasaanth Ravi Anusuyadevi

Abstract

Carbon dioxide (CO₂) detection plays a vital role in various fields, for example, environmental monitoring, healthcare, and industry. Metal oxides are used as the sensing material because of their high sensitivity and stability. However, they have limitations in detecting CO₂ as CO₂ is a chemically stable gas, which can be mitigated by post-treatment such as annealing or doping noble metals. Spark ablation, a versatile technique for synthesizing nanoparticles with controlled size and composition, was utilized in this study to produce SnO₂ nanoparticles, which were subsequently integrated into a specifically designed interdigitated electrode (IDE) structure for CO₂ sensing. The IDE configuration featured a fixed finger width of 5 μm, with the gap width ranging from 2 to 15 μm, and devices were fabricated with SnO₂ sensing areas of 1×1 cm and 1×4 cm. Noble metals such as Ag and Ru were decorated on the SnO₂ layer to enhance the catalytic activity and promote the CO₂ adsorption reaction. Surface densities of Ag and Ru under various printing conditions were analyzed using spark ablation. Based on these results, decorated SnO₂ layers were fabricated with surface coverages of 19% Ag and 12% Ru, respectively. Annealing was performed later at 450°C and 600°C, and XRD results revealed that the grain size of SnO₂ increased from 7 nm at 450°C to 12 nm at 600°C. Gas tests conducted in an N₂ atmosphere demonstrated CO₂ detection at 200°C, with a higher response observed for samples with Ru nanoparticle decoration, approximately twice that of the undecorated sample. However, no recovery was observed. Overall, samples annealed at 450°C exhibited higher responses compared to the one annealed at 600°C. In an N₂/O₂ atmosphere, the sensor exhibited almost no response to CO₂. Further investigation revealed a response to O₂, suggesting that the low operating temperature may hinder the reaction between CO₂ and adsorbed oxygen species, failing CO₂ sensing. An anomalous p-conductive behaviour was also observed in response to O₂. Experimental results showed no correlation between device area, gap width, and sensing performance.

Contents

Preface	i
Abstract	ii
Nomenclature	viii
1 Introduction	1
1.1 Research Questions	2
1.2 Outline	3
2 Literature Review	4
2.1 Sensing Mechanism	4
2.1.1 Ionosorption model	4
2.1.2 Oxygen-vacancy model	7
2.1.3 Other sensing mechanism	8
2.2 Sensing Performance	8
2.2.1 Sensing Parameters	8
2.2.2 Sensitization methods	10
2.2.3 Conclusion	10
2.3 Sensing Materials	10
2.3.1 Pristine MO_x	11
2.3.2 Composite MO_x	13
2.3.3 Summary	17
3 Methods	18
3.1 Nanoparticle Synthesis	18
3.2 Material Characterization	20
3.2.1 Scanning Electron Microscopy	20
3.2.2 Image Processing	21
3.2.3 X-ray Diffraction	23
3.3 Functional Test	24
3.4 Summary	25
4 Device Design and Fabrication	26
4.1 Mask Design	26
4.1.1 IDE Configurations	27
4.1.2 TLM Structure	29
4.2 Fabrication Process	30
4.2.1 Clean Room Fabrication	31
4.2.2 Printing Speed Selection	32

4.3	Summary	36
5	Annealing Conditions	37
5.1	Material Characterization	37
5.1.1	SEM Results	37
5.1.2	XRD Results	38
5.2	Electricity Properties	41
5.3	Au electrode	43
5.4	Summary	44
6	Results and discussion	45
6.1	Response to CO ₂	45
6.1.1	N ₂ atmosphere	45
6.1.2	Synthetic Air	46
6.2	Response to O ₂	47
6.3	Geometry Influence	50
6.4	Discussion	51
6.5	Summary	52
7	Conclusion and Recommendations	54
	References	56
A	Flow Chart	64
A.1	Part 1: Cleaning Step	64
A.1.1	CLEANING PROCEDURE: HNO ₃ 100% and 65%	64
A.2	Part 2: OXIDATION	64
A.2.1	OXIDATION	64
A.2.2	MEASUREMENT: OXIDE THICKNESS	65
A.3	METALLIZATION	65
A.3.1	COATING AND BAKING	65
A.3.2	ALIGNMENT AND EXPOSURE	65
A.3.3	DEVELOPMENT	66
A.3.4	INSPECTION	66
A.3.5	Cr/Au evaporation	66
A.3.6	LIFT-OFF	66
A.3.7	INSPECTION	66
B	XRD Calculation	67
B.1	Samples annealed at 450°C	67
B.2	Samples annealed at 600°C	69
C	V-I Graph	71
D	Gas Sensing Graphs	74

List of Figures

1.1	Studies on metal oxide-based gas sensors[6]	1
2.1	Temperature-Dependent transformation of oxygen ions [13]	5
2.2	Schematic of sensing process (a) Changes within grain when $D \gg 2\delta$ (b) Changes within grain when $D > 2\delta$ (c) Changes within grain when $D \leq 2\delta$ (d) Band structure diagram	6
2.3	Schematic of simplified gas sensing mechanisms (a) n-type metal oxide (b) p-type metal oxide	7
2.4	Studies on metal oxide-based gas sensors[6]	11
2.5	Schematic of n-BaTiO ₃ /p-CuO sensing material[53]	15
2.6	Response of BaTiO ₃ /CuO for different gases and its concentration	15
3.1	Schematic of the oscillator circuit used to activate spark ablation and the coagulation process of the particles[59]	19
3.2	(a) VSP-P1 NanoPrinter (b) Generator inside (c) Different configurations for printing [61]	20
3.3	(a) The electron signal intensity varies with the energy of electrons escaping from the sample surface;(b) The electrons in different signals from various regions within the analysis volume.[62]	21
3.4	Unsuitable image processed before and after using the Matlab script	22
3.5	Image processed with ImageJ	23
3.6	Diffraction of X-rays on a set of lattice planes with interplanar space.	23
3.7	Schematic of the gas flows	25
3.8	Main components of the gas sensing setup	25
4.1	Typical structure of the interdigitated electrode (IDE)	26
4.2	layoutA	27
4.3	layoutB	29
4.4	Deatail of the Transmission Line Model (TLM) structure	30
4.5	Fabrication Process	31
4.6	(a) Sample for measurement (b) 200 μ m/s (c)100 μ m/s (d)50 μ m/s	33
4.7	(a) Defined s-shape printing toolpath (b) Thickness of the printed square obtained from Dektak	34
4.8	SEM images of the printed Ru NP taken from line samples of a silicon die (at 50,000 magnification). The percentages shown are the surface coverage	35
4.9	SEM images of the printed Ag NP taken from line samples of a silicon die (at 50,000 magnification). The percentages shown are the surface coverage	35
4.10	Surface Coverage of Ru and Ag Nanoparticles as a Function of Printing Speed and Power	35

5.1	SEM Images of Samples before and after annealing (a) Before Anneal, x 5k (b) Before Anneal, x 60k (c) Anneal at 450°C, x 60k (d) Anneal at 600°C, x 60k (e) Anneal at 450°C, x 200k (f) Anneal at 600°C, x 200k	38
5.2	XRD results of the sample before annealing	39
5.3	XRD results after annealing at 450°C	40
5.4	XRD results after annealing at 600°C	40
5.5	(a) V-I relation 1mm*1mm, gap=2um (b) V-I relation 1mm*4mm, gap=2um (c) Energy-band diagram of a metal and semiconductor before contact; (d) ideal energy-band diagram of a metal-n-semiconductor junction for ϕ_m and ϕ_s [66]	41
5.6	V-I relation of the device annealed at 450°C and 600°C	42
5.7	Au electrode after annealing	43
5.8	EDS mapping image.	44
6.1	Response to CO ₂ in N ₂ atmosphere (a) C450, Device No.5 (b) Calculated response of Device No.5 of different samples	46
6.2	Response to CO ₂ in synthetic air, (a) C600, Device No.5 (b) C450 Device No.2	47
6.3	Response to O ₂ with different annealing temperature (a) Resistance change, Device No.5 (b) Response of these samples, Device No.5	48
6.4	Response to O ₂ with NPs (a) Resistance change of different samples, C600-Ag and C600 (b) Absolute Resistance change of these two samples	48
6.5	Response to O ₂ with NPs (a) C600, Device No.5 (b) C600-Ag, Device No.5 (c) C600-Ru, Device No.5 (d) Absolute Resistance change of these two samples	49
6.6	Resistance response of devices with different configurations under identical testing conditions.	50
B.1	XRD Pattern with Multiple Peak Fit	67
B.2	Linear Fitting Result	68
B.3	XRD Pattern with Multiple Peak Fit	69
B.4	Linear Fitting Result	70
C.1	V-I relation of the device before annealing at 450°C	71
C.2	V-I relation of the device annealed at 450°C	72
C.3	V-I relation of the device annealed at 600°C	72
C.4	V-I relation of the device annealed at 600°C	73
D.1	Response to CO ₂ in N ₂ atmosphere, Device No.5 (a) C450 (b) C600 (c) C600-Ru (d) Calculated response of these samples	74
D.2	Sudden increase in noise After high-temperature transition, C450, Device No.2	75
D.3	Gate Voltage Dependence of Source and Drain Currents (a) Case1 (b) Case2 with Hysteresis Effect	75
D.4	Raman spectra of pure and Ag, Ru decorated SnO ₂ sensing layers	76

List of Tables

2.1	Main Parameters of Gas Sensing	9
2.2	Pristine Chemiresistors	13
2.3	Compound Chemiresistors	16
4.1	Specifications of sensing device electrodes present in design A	28
4.2	Specifications of sensing device electrodes present in design B	29
4.3	Varying distances of the mirror-like TLM structure in Fig 4.4(a)	30
4.4	Oxide thickness measured with Woollam Ellipsometer	31
4.5	Height Trends with Different Speed	33
5.1	Chips Number and Printing Conditions	37
5.2	Device Number and its configuration	37
5.3	Resistance Results Derived from 10V-20V Linear Fit (Related V-I graphs are listed in Appendix C)	43
6.1	The anomalous gas sensing behaviour reported in recent literature.	52
A.1	Program name: WET1000	65
B.1	T450	68
B.2	T600	69

Introduction

Carbon dioxide (CO_2) is the key component of the atmosphere. The impact of CO_2 on daily life and industry production is manifested in various aspects. Excessive CO_2 concentrations have negative effects on human health and the environment, so it is vital to monitor both indoor and atmospheric air quality. There is also a great demand for CO_2 detection in other fields such as medical care, industrial processes, and agriculture. In the medical field, the inhalation and exhalation of respiratory CO_2 can reflect a patient's pulmonary conditions[1]. In some industrial processes, monitoring the CO_2 concentration is an effective method to assess the integrity of the packaging, as CO_2 is used for food packaging[2][3]. In modern agriculture, CO_2 is also the main raw material for photosynthesis; changes in CO_2 levels can strongly influence the growth of crops[4]. The increasing demand for CO_2 sensors has been promoting research efforts to develop sensors with a wide range of detection concentrations and enhanced performance.

Various CO_2 gas sensors have been developed based on different sensing mechanisms. Metal oxide-based gas sensors predominantly operate on a chemiresistive principle, which relies on changes in resistance to correlate with gas concentration. Fig 1.1 illustrates the distribution of commonly studied metal oxides for gas sensors. Among these, SnO_2 is one of the most historically established and widely used n-type metal oxides. These metal oxide-based gas sensors offer many advantages, such as higher response, easier fabrication, smaller size, and greater cost-effectiveness[5].

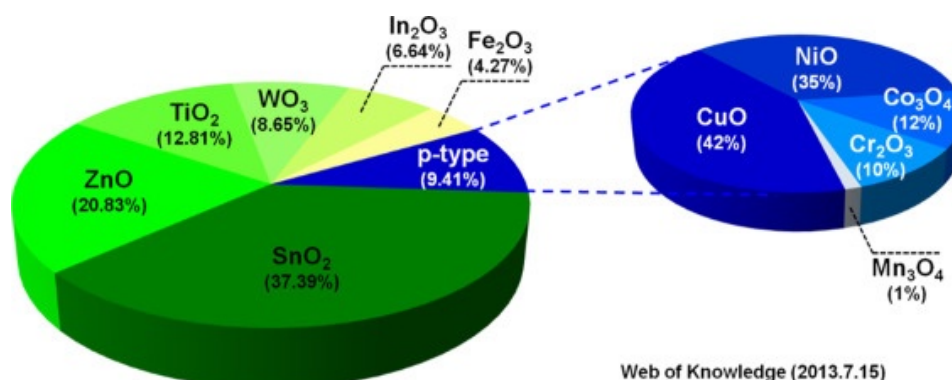


Figure 1.1: Studies on metal oxide-based gas sensors[6]

Currently, nanostructured metal oxides have attracted significant attention in this field due to their unique properties. Characterized by a high surface area-to-volume ratio, these nanomaterials offer an abundance of surface-active sites, leading to heightened surface reactivity. This enhances the sensitivity and effectiveness of CO₂ detection. These nanostructured metal oxides can be synthesized through chemical or physical methods[7]. Chemical methods, such as hydrothermal synthesis and coprecipitation, allow for precise control of particle structures or straightforward production. Hydrothermal synthesis uses high-temperature aqueous solutions under high vapour pressure to produce diverse structures like nanoparticles, nanorods, and nanocubes by adjusting reaction conditions. Coprecipitation involves adding a base to a metal salt precursor to obtain metal precipitates. Physical methods, including plasma spraying, laser ablation, and spark ablation, rely on melting the target material but differ in energy sources. Plasma spraying utilizes an electric arc to create high-temperature plasma for coatings; laser ablation uses a focused high-energy beam to vaporize the material; and spark ablation employs electric discharges to vaporize and cool material into nanoparticles.

Spark ablation is used in this project, which is discussed in detail in Chapter 3. Unlike chemical methods, spark ablation offers superior purity, requires less power, and provides precise control over material deposition. Without chemical solutions, it can effectively address the impurity concerns and achieve high-resolution printing. Moreover, targeting specific areas that need to be printed can simplify the fabrication process and reduce material waste. Unlike inkjet printing, which relies on solutions, spark ablation utilizes a solid electrode to generate nanoparticles directly.

1.1. Research Questions

This project focuses on the SnO₂-based gas sensor. As CO₂ is chemically stable, pristine metal oxides exhibit certain limitations for CO₂ sensing. In most studies, noble metal nanoparticles (NPs) have been introduced as dopants into the base material, thereby altering the matrix properties to improve gas sensing performance[8][9][10]. In contrast, this study used noble metal NPs as surface decorations. Additionally, the annealing process can significantly influence the microstructure of nanoparticles, such as grain size, defect density, and crystallinity, which will influence the gas sensing performance. Another possible way to improve the response is to find an optimal electrode spacing[11]. These considerations lead to the following research questions:

- How do different annealing conditions influence the structural, morphological, and gas-sensing performance of SnO₂ nanoparticles synthesized via spark ablation?
- What role do noble metal nanoparticles play as surface decorations in enhancing the sensitivity and selectivity of SnO₂-based gas sensors?
- How will the configuration influence the sensing performance?

By addressing these questions, this study aims to optimize the material properties and fabrication processes of SnO₂-based CO₂ sensors, contributing to the development of high-performance devices with enhanced detection capabilities for environmental monitoring.

1.2. Outline

The structure of this paper is as follows: Chapter 2 explains the chemiresistive sensing mechanism for CO₂ and provides an extensive review of the state-of-the-art research on MO_x materials. Chapter 3 details the experimental methods and instruments utilized in this study. Chapter 4 focuses on the design and fabrication process of the devices. In Chapter 5, the effects of different annealing conditions are analyzed in relation to the research questions. Chapter 6 presents the gas sensing performance to CO₂ of the fabricated devices. Finally, Chapter 7 concludes the paper by summarizing the main findings, highlighting the contributions, and proposing directions for future research.

2

Literature Review

In this chapter, various sensing mechanisms are introduced, with particular attention on the chemiresistive sensing mechanism for CO₂. Understanding this mechanism is crucial for revealing the factors that influence its sensing properties. Therefore, two models, namely, the ionosorption model and the oxygen-vacancy model, are discussed in detail. Moreover, key parameters essential to quantifying the sensing performance are introduced.

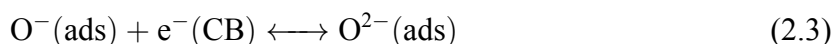
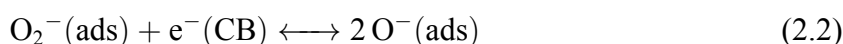
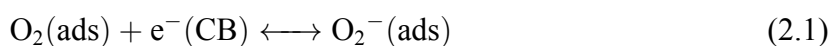
2.1. Sensing Mechanism

The gas sensing principle of the metal oxide-based gas sensor, whether p-type or n-type, is based on the change in their resistivity in response to the presence of different gases. The behaviour of these sensors differs for reducing and oxidizing gases, and the mechanism varies slightly between p-type and n-type semiconductors. The gas sensing mechanism can be explained by two models: the ionosorption model and the oxygen-vacancy model. Although CO₂ conduction in metal oxides(MO_x) is a complicated process and these two models cannot fully cover all experimental findings, they are crucial for understanding the sensing performances.

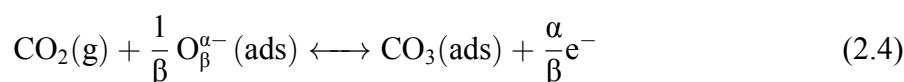
2.1.1. Ionosorption model

The ionosorption model involves two functions: reception and transduction.

Reception Function



Transduction Function



Here, SnO_2 is used as an example to illustrate the ionosorption model. In the reception, the oxygen molecules are absorbed on the surface of the MO_x . Then they accept the electrons from the conduction band from metal oxide to form "ionisorbed" oxygen ions: superoxide molecular oxygen (O_2^-), charged atomic oxygen (O^- , O^{2-}). The ionization behaviour of oxygen exhibits a profound dependence on temperature, as Fig 2.1 shows. O_2^- dominates below 150°C , while O^- mainly exists at the range 150°C to 450°C [12]. As eq.4 indicates, larger values of α and smaller values of β correlate with a greater release of electrons when exposed to CO_2 . Consequently, when O^{2-} is present at higher temperatures, the resistivity experiences a more significant decrease, thereby leading to higher sensitivity.

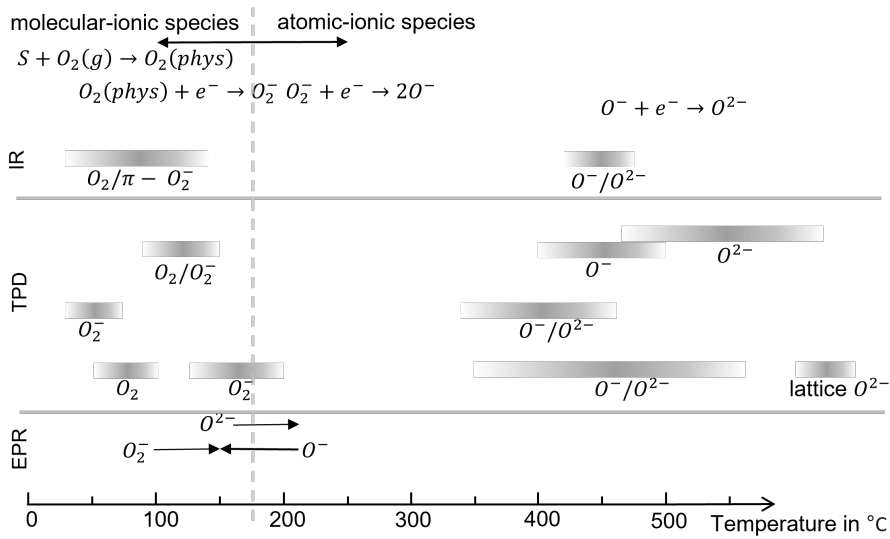


Figure 2.1: Temperature-Dependent transformation of oxygen ions [13]

The working temperature for a gas sensor is normally high ($100\text{--}500^\circ\text{C}$), so oxygen ions exist as O^- . As Fig 2.2a shows, the oxygen ion adsorption resulted in the formation of charged species, leading to the accumulation of negative charge on the surface. Consequently, electrons in the conduction band are repelled, causing an upward bending in the energy band diagram as shown in Fig 2.2b. This segment of the energy barrier represents the energy that electrons need to overcome to participate in conduction. The width of this depleted region is denoted as L , which can be determined by eq.2.5[14]. In this equation, k is the Boltzmann constant, T is the temperature, e is the electron charge, and V_s is the surface potential. T is also directly influenced by the Debye length δ , calculated by eq.2.6, where ϵ denotes the permittivity and n denotes the electron density.

$$L = \delta \left(\frac{2eV_s}{kT} \right)^{\frac{1}{2}} \quad (2.5)$$

$$\delta = \left(\frac{\epsilon kT}{ne^2} \right)^{\frac{1}{2}} \quad (2.6)$$

After the reception of an analyte through the change in ion-adsorbed oxygen concentration, the conductivity of MO_x is quantitatively varied in compliance with the transduction function. When MO_x are exposed to CO_2 , CO_2 will react with preadsorbed oxygen ions to form CO_3

while releasing electrons back to the semiconductor, as eq.2.4 shows[15].

To conclude, the formation of anionic oxygen adsorption on the surface of MO_x creates a surface potential barrier, which results in the bending of the oxide band structure within the Debye length. According to the report of Tricoil et al., if metal oxide particles have grain sizes G smaller than twice the Debye length δ ($D < 2\delta$), the sensitivity of the sensor will significantly increase[16]. For large grains ($D \gg \delta$) in Fig 2.2a, because of the existence of the scattering electrons with the Debye length of MO_x , the impact of the interactions with the analyte is limited, leading to low sensitivity to the analyte. If $D > 2\delta$ as shown in Fig 2.2b, it has moderate sensitivity with the conduction channel measured L_c , which is determined by the oxygen ion concentration on the surface. In the case of $D \leq 2\delta$, the whole grain is depleted, and a conduction channel will be created through the oxygen, remarkably increasing the electron mobility and conductivity. Therefore, it has a high sensitivity to the analyte.

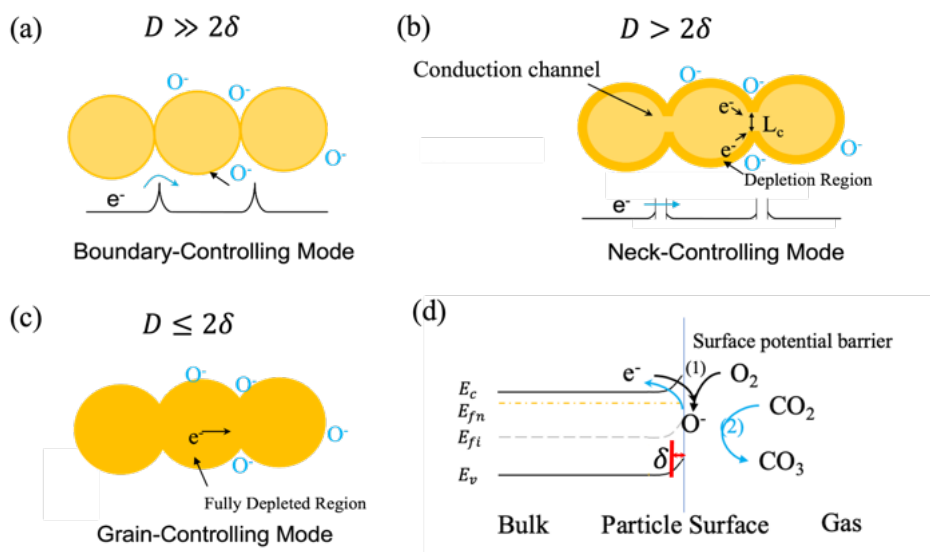


Figure 2.2: Schematic of sensing process (a) Changes within grain when $D \gg 2\delta$ (b) Changes within grain when $D > 2\delta$ (c) Changes within grain when $D \leq 2\delta$ (d) Band structure diagram

The conduction mechanism of p-type metal oxide is slightly different from that of n-type. Fig 2.3a illustrates the conduction mechanism controlled by the depletion layer, while Fig 2.3b depicts the conduction mechanism controlled by the accumulation layer. The resistance of an n-type semiconductor can be simplified as a series of particle cores and resistance shells. When exposed to reducing gases, the electrons released by the reducing gas are injected into the core, reducing the sensor's resistance. In the case of p-type conductors, there are two conduction paths: through the resistance core or the surface hole accumulation layer. Therefore, its resistance can be considered in parallel. Moreover, as current mainly flows through the accumulation layer, Barsan et al. proposed the simple assumption that the conductivity is directly related to the average electron concentration in the accumulation layer[17]. Therefore, when exposed to reducing gases, the released electrons recombine with the holes in the accumulation layer, reducing the concentration of holes and leading to an increase in resistance. Huber et al. investigated the relationship between n-type and p-type sensitivity under the same conditions

and derived the following relationship[18]:

$$S_p = \sqrt{S_n} \quad (2.7)$$

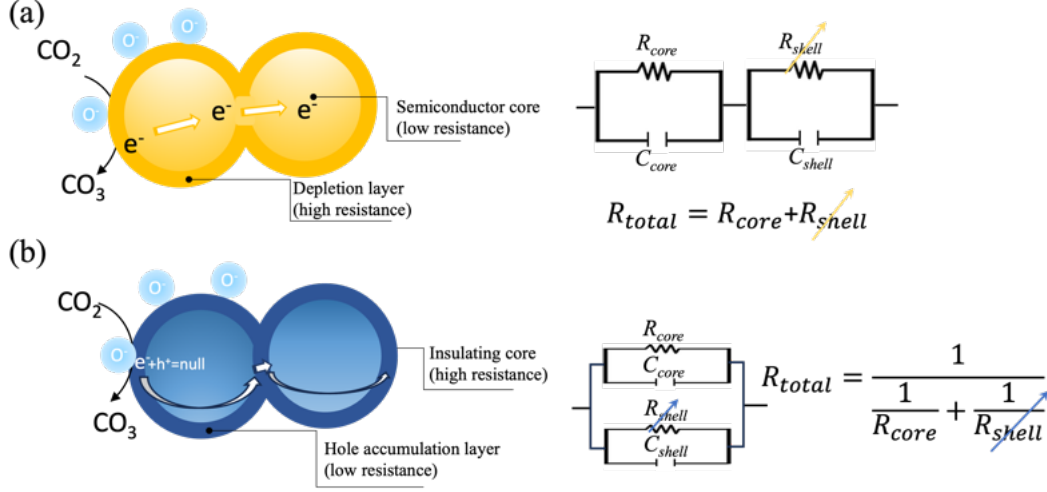
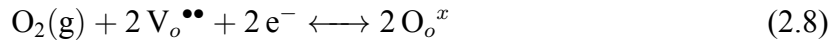


Figure 2.3: Schematic of simplified gas sensing mechanisms (a) n-type metal oxide (b) p-type metal oxide

2.1.2. Oxygen-vacancy model

The sensing mechanism can also be explained by a direct reaction between the donor species that forms the metal oxide surface and the reducing gas. Take n-type SnO_2 for example, oxygen vacancies $V_o^{\bullet\bullet}$ most probably act as donor species, with its nonstoichiometry (SnO_{2-x} , $0 < x < 2$). In the presence of oxygen, O_o^x dominates in the bulk, as eq.2.8 indicates. When CO_2 is introduced, it will react with the oxygen (O_o^x) in the lattice, forming a meta-stable compound (CO_3) and neutral oxygen vacancies (V_o^x). Then, V_o^x will be transformed into $V_o^{\bullet\bullet}$ and release electrons, which later participate in the formation of O_o^x . In this process, more oxygen vacancies are formed, which inject free electrons into its conduction band, increasing its conductivity.



The diffusion of oxygen vacancies will significantly influence the sensitivity of the gas sensor. According to Oprea et al[19], the sensitivity will be significantly reduced if the conduction mechanism ($[V_o^{\bullet\bullet}] < [V_{surf}^{\bullet\bullet}]$) switches to the accumulation layer controlled ($[V_o^{\bullet\bullet}] > [V_{surf}^{\bullet\bullet}]$). Understanding the diffusion of vacancies in bulk metal oxides becomes paramount in this context, with material properties and temperature emerging as key influencers. Notably, the lattice parameters of the material determine the jump distance and the number of jump directions. Furthermore, temperature regulation directly impacts the frequency of these jumps. This interconnected understanding provides insights into how the diffusion of vacancies can

impact the overall performance of gas sensors.

For the ionosorption model and the oxygen vacancy model, the eq.2.5 and eq.2.6 are applicable, and the impact of grain size on gas sensing is consistent. However, the former considers chemisorbed oxygen on the surface of MO_x as the primary active species inducing the response, while the oxygen vacancy model emphasizes that the response of MO_x is because of subsequent reduction and oxidation reactions occurring on the surface in the presence of reactive gas species.

2.1.3. Other sensing mechanism

Apart from metal oxide-based chemiresistive gas sensors, Table shows two other mechanisms, optical and electrochemical. Within the realm of electrochemical sensing, three prominent methods emerge: potentiometric, calorimetric, and acoustic. Note that the other two sensor types do not primarily utilize metal oxides in their operation, but metals also play a crucial role in these sensors. Mishra et al. categorized gas sensors based on different principles into six major classes, chemiresistive (resistance change), electrochemical (electromotive force or current change), piezo-electric (mass change), field effect transistor (work function change), capacitance (capacitance change) and optical sensors (shown in Table.x [20]. As this article mainly focuses on metal oxide-based gas sensors, other sensing mechanisms are not overly elaborated here.

2.2. Sensing Performance

2.2.1. Sensing Parameters

To quantify the sensing performance of gas sensors, several key parameters have been introduced. While Table.2.1 defines these parameters, further clarification is required for some of them.

Sensitivity is one of the most important parameters, which is presented by the Response (S). For the response, it is important to note that different articles and studies may use varying definitions and standards, as eq.2.11 shows. Normally, for a reducing-type gas sensor, the S is defined as R_a/R_g , where R_a is the reference resistance and R_g is the resistance when exposed to the analyte atmosphere.

$$S = \frac{R_a}{R_g}, \frac{R_g}{R_a} \quad \text{or} \quad \frac{|R_a - R_g|}{R_a} \quad (2.11)$$

Sensitivity can be influenced by various factors, to name a few, the sensing material itself, operating temperature, and environmental conditions, especially temperature and humidity. This phenomenon that a sensor's response to one stimulus is affected by the presence of another is called cross-sensitivity. Regarding the sensing material, increasing the surface area (high area-to-volume ratio) is a common strategy to enhance sensitivity.

For selectivity, some CO_2 sensors exhibit cross-sensitivity to other gases. Cross-sensitivity occurs when a gas other than the one being monitored triggers the gas sensor to register a reading even in the absence of the target gas. Take SnO_2 and ZnO_2 for example; they can respond

not only to CO₂, but also to humidity and other gases like methane (CH₄), hydrogen (H₂), and nitrogen dioxide (NO₂)[21].

The limit of detection (LOD) can be defined by eq 2.12, which is usually reported in concentration units(ppm)[22]. RMS refers to the root mean square (RMS) value of the noise in a system. This formula can indicate the smallest signal it can reliably measure.

$$LOD = \frac{3 \times \text{RMS noise}}{\text{Sensitivity}} \quad (2.12)$$

The response time is defined as the time required for a certain percent of the output change in resistance after exposure to the target gas, a 90% final response is commonly used; however, sometimes 63% can also be found. Similarly, the recovery time refers to the time it takes for the sensor to return from its response state to the baseline.

Working temperature is another important issue regarding the performance of a sensor. Gas sensors typically operate at high temperatures, resulting in high power consumption. To tackle this issue and enhance sensitivity, researchers explore sensing materials suitable for room temperature conditions[23][24]. Additionally, microheaters are introduced to precisely control the operating temperature of the sensor[21][25].

Repeatability, usually associated with precision, represents the ability of a gas sensor to maintain stable and consistent measurements multiple times under the same conditions. It is defined by the variance in values obtained under the same measurement conditions.

In general, an ideal gas sensor should exhibit high sensitivity, exceptional selectivity, a rapid response time, and the capability to operate stably over extended periods.

Table 2.1: Main Parameters of Gas Sensing

Parameters	definition
Sensitivity	The variations that occur in the detected signal output per concentration of the target analyte.
Selectivity	A sensor's ability to act selectively to single or multiple target analytes.
Stability	The ability to reproduce the data for a particular time limit is a sensing device's significant characteristic and is termed stability.
Detection limit	Typically defined as the minimum signal that can still be resolved above the noise floor.
Response time	the time taken for a certain percentage of the output resistance change after exposure to the target gas
Recovery time	the time taken for output resistance change upon returning to the air
Working temperature	The temperature with maximum sensitivity.
Repeatability	The ability of a sensor to replicate a measurement when put back in the same circumstances.

2.2.2. Sensitization methods

Many efforts have been made to optimize the design and materials of gas sensors to meet these criteria. Regarding the structural design of sensors, there has been an evolution in transducer technology from pellets to microhotplates. The first-generation sensor structures were relatively simple, involving metal deposition as thick films on Al_2O_3 tubes and substrates. This kind of sensor is still commercially available now[26]. In recent years, MEMS-based sensors have emerged, facilitating the miniaturization of gas sensors. A crucial component introduced in the design is the microhotplate, which will be discussed in detail in Chapter . Apart from this, plastic foils are considered the supporting material due to their flexible design, lightweight, and high transparency, which offer promising applications. However, its current limitation is the inability to withstand temperatures over 400°C [27]. To overcome the challenges of the high working temperature, ultraviolet (UV) irradiation is used as an alternative to provide the required energy. Therefore, it can notably avoid adverse changes that may occur in sensing materials during heating. It also offers many other advantages, for example, low energy consumption and enhanced selectivity[28].

From the perspective of materials science, the structure of a material determines its properties. Doping is an effective strategy to change material structure. As dopants usually have different radii and valence states with the base metal oxides, more oxygen vacancies are introduced into the lattice. According to the oxygen-vacancy model, more active sites are generated in this process because of the increasing vacancies. Morphology control is another strategy to improve performance. As mentioned in 2.1.1, when the particle size is smaller than twice the Debye length, the gas sensitivity will be improved remarkably. In addition to controlling the particle size, researchers also carefully design various geometric shapes of sensing materials. Taking the heterojunction $\text{BaTiO}_3/\text{CuO}$ for example, Joshi et al. manipulate the deposition process to form CuO spheroids and BaTiO_3 microleaves[29]. This designed morphology significantly enhances sensing performance.

2.2.3. Conclusion

The gas sensing mechanism of metal oxide-based gas sensors, whether p-type or n-type, relies on the change in resistivity in response to the analyte. The resistance of n-type metal oxide will decrease when exposed to the reducing gas, while p-type semiconductors exhibit the opposite effect in the presence of it. The gas sensing mechanism is explained through models such as ionosorption and oxygen-vacancy, illustrating the reception, transduction, and direct reactions between donor species and gases. Sensing parameters, for example, sensitivity, selectivity, stability, detection limit, response time, recovery time, working temperature, and repeatability, are crucial for evaluating gas sensor performance. To enhance the performance of a gas sensor, there are mainly two strategies. The first involves the structural design of the sensor such as including the microhotplate. The second entails modifications to the material itself, such as doping and morphology design.

2.3. Sensing Materials

The following chapter will focus on pristine and composite metal oxide materials used in gas sensors. The earliest recorded use of metal oxide as a gas sensor dates back to the 1960s. [30].

SnO₂ was first used as a gas sensing material for H₂ detection at that time. Over the years, more and more metal oxides have been used for gas detection as Fig 2.4 shows. Currently, the most representative metal oxide materials in gas sensors typically exhibit characteristics of n-type semiconductors. According to Hubner, the response of an n-type gas sensor is equivalent to the square of the response of a p-type sensor. Though they have less response, p-type metal oxide-based gas sensors possess unique advantages, particularly enhanced selectivity. CuO and rare earth oxides are two p-type metal oxides studied for CO₂.

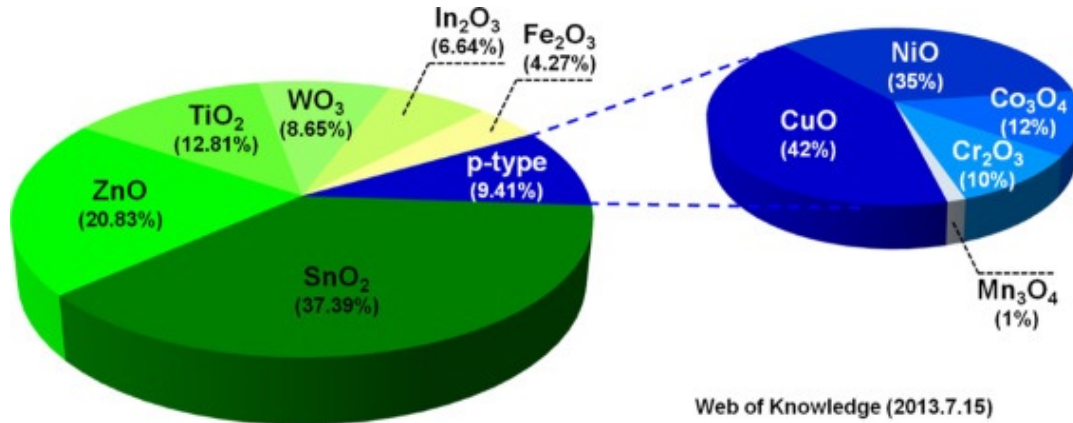


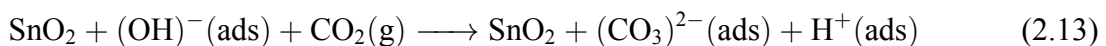
Figure 2.4: Studies on metal oxide-based gas sensors[6]

2.3.1. Pristine MO_x

Tin Oxide

SnO₂ is an n-type semiconductor with a bandgap of 3.6 eV and abundant surface oxygen vacancies. According to the oxygen-vacancy model, such defects can help form active sites for the adsorption of atmospheric oxygen (O₂), thereby maximizing the sensitivity of the sensor. SnO₂ also exhibits excellent thermal stability. It is stable in the air for at least up to 500 °C with a melting point as high as 1630 °C [31]. The first commercially sintered SnO₂ gas sensor was manufactured in 1962[32]. Since then, extensive research has been conducted on SnO₂ because of its high sensitivity and stability.

Wang et.al fabricated the thick-film sensor with SnO₂ nanopowder, which was prepared by the co-precipitation method[33]. They found that the CO₂ response is strongly affected by the relative humidity values in the ambient. The calculations according to Density functional theory (DFT) reveal a significant relationship between the surface configuration of SnO₂ and oxygen concentration. The preadsorbed O₂⁻ exhibits minimal responsiveness to CO₂, indicating a very weak interaction between them. However, when preadsorbed OH⁻ exists, as eq.2.13 shows, CO₂ can react with O in OH⁻ and release electrons on the SnO₂ surface. However, as the humidity increases, the sensing response worsens as the OH⁻ occupies most of the active adsorption sites[33]. Moreover, the sensing performance is significantly enhanced when the grain size is below 10nm. The influence of the grain size on sensing properties can be explained by the ionosrption model discussed in section 2.1.1.



Zinc Oxide

ZnO is also an n-type metal oxide with a direct band gap of 3.37 eV at room temperature[34]. Kannan et al. fabricated ZnO film using DC sputtering to make a CO₂ gas sensor[35]. In this process, particle size and crystal orientation can be controlled by varying the thickness of the ZnO film (10nm, 100nm, 300nm); as the film thickness decreases, the response is significantly improved. For the film of 40nm, the particle size was calculated to be 22nm using Debye Scherrer's equation. However, the value derived from AFM was 290nm. This significant difference is attributed to the migration of the grain boundaries during the annealing process. Unlike SnO₂ with a reducing resistance in CO₂, ZnO demonstrates an increasing resistance. This is because CO₂ here acts as an oxidizing gas. The sensing mechanism can be explained by the following equations:



Xu et al. showed the feasibility of the suspension plasma spraying (SPS) process for fabricating finely structured porous ZnO coatings[1]. ZnO powder was prepared by hydrothermal reaction and then dispersed in deionized water to form the injecting materials. With SPS, the sensitivity to carbon dioxide (CO₂) analyte gas was raised (6.87 to 400 ppm, RT 20%). The ZnO also exhibits similar synergistic behaviour between OH- and CO₂ to that observed in SnO₂. Moreover, as the Relative Humidity (RH) increases, the response-recovery time becomes longer. This is attributed to the higher RH leading to an increased presence of OH- ions and hydroxyl groups, requiring more time to reach equilibrium. Xu et al. also noted the presence of nitrogen (N) in the coatings. According to the study by Xia et al., when nitrogen (N₂) is used as the carrier gas, the response of ZnO to CO₂ is nearly twice as high as when air is used as the carrier gas. This phenomenon can be explained by the Density Functional Theory (DFT) calculations. The DFT results revealed that on the surface of nitrogen-doped ZnO, nitrogen's sp² hybridized orbitals and 2p orbitals form σ and ϕ bonds with the carbon and oxygen atoms in CO₂ molecules, promoting CO₂ adsorption and reaction. However, in the presence of pre-adsorbed oxygen (O₂), nitrogen's orbitals mix with the 2s/2p orbitals of oxygen atoms in O₂ molecules, hindering the interaction between CO₂ and nitrogen-doped ZnO, thereby limiting the response in air. Detailed mechanisms are explained by Xia et al.'s DFT calculations[36].

Bagheri et al. investigated the response of ZnO to CO₂ under UV irradiation with increasing temperature[37]. They found that ZnO behaves like a p-type metal oxide at room temperature but transitions from p-type to n-type as the temperature rises to 80 °C. This can be attributed to V_{zn}, which acts as an acceptor, leading to ZnO exhibiting p-type conductivity.

Copper Oxide

CuO has a narrow band gap of 1.10 eV to 1.26 eV at room temperature. As one of the most promising sensing materials, CuO is distinguished by its low cost and abundant natural availability. Tanvir et al. investigate the properties of CuO-NPs for CO₂ gas sensing at room temperature[33]. The FTIR measurements show that the formation of hydroxocarbonate species (malachite and azurite) influences the response. Currently, CuO plays more of a role as a catalyst in CO₂ gas sensing than as a direct gas sensing material.

Other pristine MO_x

Rare-earth metals are also promising candidates for gas sensors. La₂O₃ has a large band gap of 5.5 eV. It exhibits good sensitivity to CO₂. Yadav et al. reported excellent sensitivity (0.48/350 ppm) with microrod-like La₂O₃ thin films constructed by chemical bath deposition [38]. Their study focused on a relatively narrow concentration range, specifically between 100 and 350 ppm. Other MO_x that can be used for CO₂ detection include CdO, CeO₂, and In₂Fe₃. Due to the chemical stability of CO₂, the reactivity of CO₂ to pristine is usually limited. Consequently, research in CO₂ sensor has gradually expanded to include composite MO_x materials.

Table 2.2: Pristine Chemiresistors

Sensing Material	Synthesis route	Morphology	temp. (°C)/AT.	Response	t _{res} /t _{rec}	Analyte	Ref.
SnO ₂	Co-precipitation	nanoparticles	240/RH14%	1.24/2000	350/4	CO ₂	[33]
	Mini-arc plasma	nanoparticles	250	5.8 [*] /100	8/15	ethanol	[39]
	Spark ablation	nanoparticles	450/RH30%	8/100		H ₂	[40]
	pulsed laser ablation deposition	film	320	210.5/2500	64.2/0.3	H ₂	[41]
	Sol-gel spin coating	thin film	200	0.19/100	7/1202	NO ₂	[42]
ZnO	Magnetron sputtering	nanoparticles	300/N ₂	1.3 ^b /1000	20/20	CO ₂	[35]
	Plasma spraying	thin film	300			NO ₂	[43]
	hydrothermal method	nanoparticles	80/UV	22 ^c /8,000	<10/<10	CO ₂	[37]
	hydrothermal method	hollow sphere	RT/RH60%	1.42 ^d /50,000	900.3/978.2	CO ₂	[1]
CuO	atmospheric plasma spraying	nanoparticles	150	110 ^b /500	280/665	CO	[44]
	atmospheric plasma spraying	nanoparticles	RT/RH20%			CO ₂	[45]
CeO ₂	Coprecipitation	nanoparticles	400	34 [*] /800		CO ₂	[46]
La ₂ O ₃	Chemical bath	microrods	250	0.48/350	50/73	CO ₂	[38]
WO ₃	Spark ablation	nanoparticles	200	511 ^d /10	354/480	NO ₂	[47]
In ₂ Te ₃	Flash evaporation	Thin film	200	11 ^c */1000		CO ₂	[48]

In column 'Response', 1.24/2000 means that with a concentration of the target gas at 2000 ppm, the response is 1.24.

* indicates that the corresponding value has been obtained from the figure, rather than directly cited from the passage

$$^b S = (R_g - R_a) / R_a * 100$$

$$^c S = (R_a - R_g) / R_a * 100$$

$$^d S = R_g / R_a$$

2.3.2. Composite MO_x

As CO₂ is a chemically stable gas, it is less sensitive for the pristine chemiresistors to detect CO₂. Therefore, many composite metal oxide-based CO₂ gas sensors come into view, as Table 2.3 shows. The two most common composites involve doping La (lanthanum) into SnO₂ and mixing BaTiO₃ with other metal oxides.

La-doped SnO₂

Early in 1993, Sugai et al. approved that doping with a certain concentration of rare earth elements can enhance the sensing sensitivity of SnO₂ for CO₂ detection[49]. Kim et al. produced the sensing film with powder mixing of SnO₂ and La₂O₃ by mechanical milling. With 2.2 mol% La₂O₃, the sensitivity increased from 1.14 to 1.52 at 400°C. However, [50]. Xiong et al. compared the sensing properties with three different doping elements: La, Gd, and Lu[51]. La was proven to be the most effective additive at a concentration of 4 at.%. The main reasons can be attributed to two aspects, as Eqs(2.16) and Eqs(2.17) show. Firstly, due to the larger ionic radius of La³⁺ (0.106 nm) compared to Gd³⁺ (0.0938 nm) and Lu³⁺ (0.0848 nm), the lattice expansion is more distinct, introducing more oxygen vacancies. Secondly, La exhibits stronger alkalinity, which enhances its tendency to react with acidic CO₂, thereby increasing the concentration of CO₃²⁻.



BaTiO₃/CuO

Among the recently studied heterostructures, n-BaTiO₃/p-CuO exhibits excellent performance for CO₂ detection. When BaTiO₃ and CuO come into contact, a p-n junction is formed, and the work function of this p-n junction changes in response to different gas environments.

Herran et al. first synthesized BaTiO₃/CuO thin film for CO₂ detection and studied the influence of Ag additives on this thin film[10] in 2007. The BaTiO₃/CuO layer was fabricated by RF magnetron and Ag additives were deposited by DC sputtering. Results show that the response of film with Ag additives increases from 20 to 27 at 250 °C. This is attributed to the formation of the metal-semiconductor junction between Ag and BaTiO₃/CuO film. However, the presence of Ag does not affect the response and recovery time, as well as the reaction temperature, indicating its independence from catalytic effects. At 225 °C, the detection of CO₂ concentration relies on capacitance changes, while at 250 °C, it relies on resistance variations. Notably, the capacitance sensor exhibits a higher response. Later in 2009, they successfully developed a thinner film (125nm), with a significantly reduced response time of 2 minutes (320nm, 15 minutes)[52]. The BaTiO₃/CuO layer shows higher sensitivity than practical low-cost commercial CO₂ sensors in the main application range, which is between 500 and 5000 ppm. It can be used for monitoring indoor air quality and packaging industries.

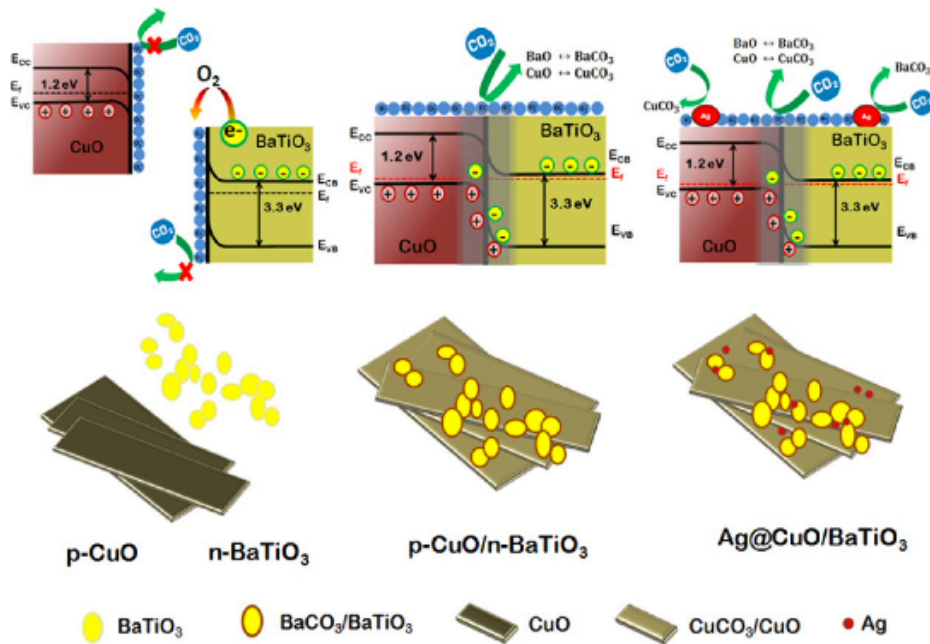


Figure 2.5: Schematic of n-BaTiO₃/p-CuO sensing material[53]

Joshi et al. investigated a nanostructured sensitive layer consisting of spherical barium titanate (BaTiO₃) decorated on copper oxide microwaves with Ag additives[53]. The sensitivity of the BaTiO₃/CuO composite with 1 wt % Ag is six times higher than that without Ag. Additionally, this sensor exhibits outstanding selectivity against gases such as CO, NO₂, and SO₂ and demonstrates long-term (180 days) stability at 120 °C. Shwetha et al. utilized Plasma-Enhanced Chemical Vapor Deposition (PECVD) to fabricate the sensing film and integrated a platinum micro-heater onto the sensor film. This sensor demonstrated low power consumption (250 °C with 4.8 mW). It exhibited remarkable sensitivity performance, achieving 21% at 400 ppm, and displayed high selectivity as Fig 2.6 shows.

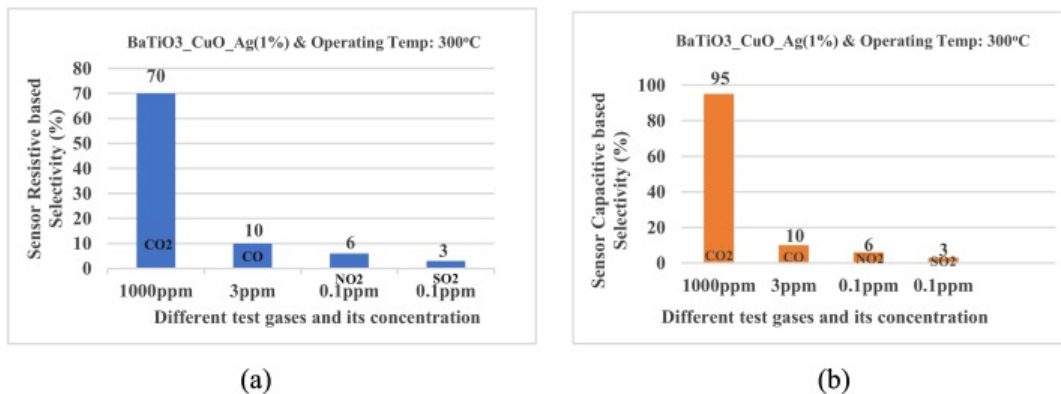


Figure 2.6: Response of BaTiO₃/CuO for different gases and its concentration

Other composites

In the preceding section, the fabrication of CuO/BaTiO₃ thin films was discussed, where CuO spheroids and BaTiO₃ microleaves constituted the microstructure by Joshi et al. They replaced

BaTiO₃ with ZnO, creating a heterojunction with a similar configuration[29]. While CuO/ZnO exhibits high repeatability, accuracy, and long-term stability, CuO/BaTiO₃ shows slightly better performance in gas sensing applications.

A Cr-doped TiO₂ sensor at room temperature was studied by Mardare et al. Normally, TiO₂ exists in two phases, namely anatase and rutile. The latter one exhibits a larger dielectric constant. Cr dopants can not only increase the number of oxygen vacancies but also facilitate the transformation of TiO₂ towards the rutile phase. A Cr concentration of 4% can achieve a pure rutile structure.

Table 2.3: Compound Chemiresistors

Sensing Material	Synthesis route	Morphology	temp. (°C)/AT.	Response	t_{res}/t_{rec}	Ref.
SnO ₂ @La ₂ O ₃	mechanical milling	nanoparticles	400	1.51/1000		[50]
SnO ₂ @La	hydrothermal	nanoparticles	250/N ₂	29.8 ^c /500	30s/75s	[51]
SnO ₂ @LaOCl	electrospinning	nanofiber	250	3.7/1000	24s/92s	[54]
CuO/BaTiO ₃	RF sputtering	Thin film	250	1.095 ^d /5000		[10]
CuO/BaTiO ₃ @Ag	RF sputtering	Thin film	250	1.22 ^d /5000		[10]
CuO/BaTiO ₃ @Ag	RF sputtering	Thin film	300/40% RH	1.17 ^{d*} /5000	2min/3min	[52]
CuO/BaTiO ₃ @Ag	hydrothermal route	Spheroids and microleaves	120	1.53 ^d /1000	10s	[53]
CuO/BaTiO ₃ @Ag	PECVD	nanoparticles	300	1.70 ^d /1000		[21]
CuO/ZnO@Ag	hydrothermal route	ZnO microspheres CuO nanoleaves	320	1.28 ^d /1000	76s/256s	[29]
CuO/CuFe ₂ O ₄	RF sputtering	Thin film	250	1.40 ^d /5000	55min/8min	[55]
TiO ₂ @Cr	RF sputtering	Thin film	60	1.80 ^{c*} /50,000	1s/63s	[23]
TiO ₂ @Fe	RF sputtering	Thin film	35	2.4 ^{c*} /50,000		[24]
TiO ₂ /Al ₂ O ₃	Atomic Layer Deposition(ALD)	Thin film	RT/air, UV light	1.306/5ppm		[56]
TiO ₂ /Pd	Thermal evaporation	Thin film	RT/N ₂	3.72/25,000ppm		[9]

* indicates that the corresponding value has been obtained from the figure rather than directly cited from the passage

@ indicates doping

/ indicates heterojunction

^b S = (R_g-R_a)/R_a*100

^c S = (R_a-R_g)/R_a*100

^d S = R_g/R_a

2.3.3. Summary

Compared with other pristine metal oxides such as ZnO and CuO, SnO₂ often exhibits higher sensitivity to CO₂. It also demonstrates excellent performance in terms of response time, stability, and detection range. These advantages have made SnO₂ a widely studied material. However, SnO₂ also faces certain challenges. Firstly, the CO₂ response of SnO₂ sensors is strongly influenced by the relative humidity of the environment[33]. Secondly, as a gas sensor, SnO₂ exhibits poor selectivity for CO₂, with its responses to ethanol and H₂ far exceeding those to CO₂ [39][40]. To enhance the overall performance of sensors, doping has emerged as an effective strategy. In the current research, La-doped SnO₂ has proven to be the most favourable combination[9][51][54]. However, as of now, there is no research available on a humidity-insensitive CO₂ gas sensor. Instead, studies have focused on effectively utilizing the humidity-sensitive properties of SnO₂ gas sensors for humidity detection[57] [58] . Another promising approach for composite sensing materials is to construct heterojunctions using CuO and BaTiO₃, with Ag serving as dopants. This combination enables the sensor to resist interference from other gases, enhancing its selectivity for CO₂. While resistive-based sensitivity is already high, measurements based on capacitance provide even better results[21].

3

Methods

This chapter presents the methodologies employed in this thesis, including the instruments and techniques used for nanoparticle synthesis, the material and electrical characterization methods, and the gas sensing setup utilized for functional testing.

3.1. Nanoparticle Synthesis

Spark ablation is employed here to synthesize metal nanoparticles. The equivalent circuit is shown in Fig 3.1[59]. The target material is prepared as two solid electrodes. Then an electrical spark excites plasma, ablating the electrode material to form nanoparticle aerosol. Each spark only takes a few microseconds with a high temperature of 20,000K or higher[60]. This short-duration, high-energy spark rapidly heats the electrode material, causing it to almost instantaneously reach its boiling point. In the presence of a flowing inert gas, the vaporized material is rapidly quenched. This fast cooling suppresses the nucleation and growth of equilibrium crystalline phases, leading to the condensation of the material into nanoparticles. These particles collide and grow to reach stability, and then deposit onto the substrate. As the synthesis process occurs entirely in the dry gas phase, it eliminates the need for surfactants or precursors, ensuring the nanoparticles' purity. Additionally, due to the extremely high operating temperatures (20,000 K or even higher), there are virtually no restrictions on the types of metals that can be used.

For a given electrode material, the key parameters influencing the nanoparticle layer include spark energy, printing speed, and the number of printing repetitions. Higher spark energy generates stronger plasma, increasing the ablation rate and producing more nanoparticles. According to the study by T.V. Pfeiffer et al.[60], spark energy also plays a critical role in controlling the primary particle size, which is crucial for determining the material properties of spark-formed nanoparticles. Printing speed determines the spatial distribution of these nanoparticles on the substrate, with slower speeds resulting in thicker and denser layers. Meanwhile, the number of printing repetitions directly influences the final layer thickness. Selecting appropriate printing conditions is therefore crucial for fabricating a sensing layer.

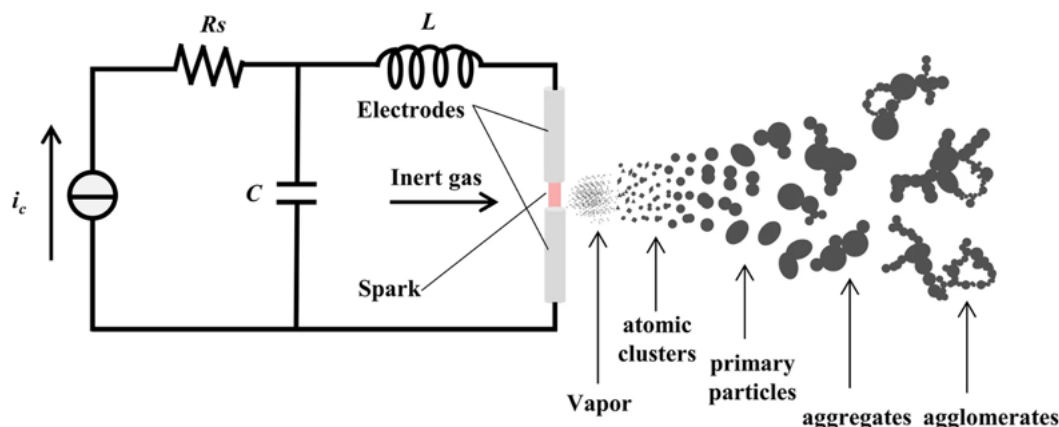


Figure 3.1: Schematic of the oscillator circuit used to activate spark ablation and the coagulation process of the particles[59]

In this work, the VSP-P1 NanoPrinter by VSPARTICLE was used for generating metal nanoparticles ranging in size from 1 to 20 nm. Fig 3.2a shows the VSP-P1 used in this project, with its core component being the generator, which is illustrated in detail in Fig 3.2b. This generator allows for the placement of two electrodes, which can be made of the same or different materials. Consequently, with a single generator, the first three configurations depicted in Fig 3.2c can be easily achieved, such as bimetals and nanoalloys. By equipping the NanoPrinter with two generators, more advanced configurations, such as sequential deposition or mixing of streams, can also be realized. The VSP-P1 currently used in this project is equipped with three generators, enabling more complex operations.

Regardless of the printing configuration, after the electrode material is manually loaded, the process can be fully controlled through the control panel with a customized script, making the operation extremely straightforward and user-friendly. For example, spark power can be manually adjusted through the control panel, while the deposition path and speed are defined in advance via a customized script. This programmable dry-printing system provides precise control over material distribution and pattern formation, enabling a high level of printing precision for fabricating complex structures and advanced sensing layers. In this project, the constructed sensing layer consists of a base layer of Sn, decorated with Ag or Ru nanoparticles. To fabricate this layer, three generators of the VSP-P1 NanoPrinter were loaded with pure Sn, Ag, and Ru electrodes, respectively. The deposition process was precisely controlled by defining the required spark energy, deposition path, and printing speed for each metal using a customized script. This approach enabled the efficient and accurate fabrication of the desired multilayered structure.

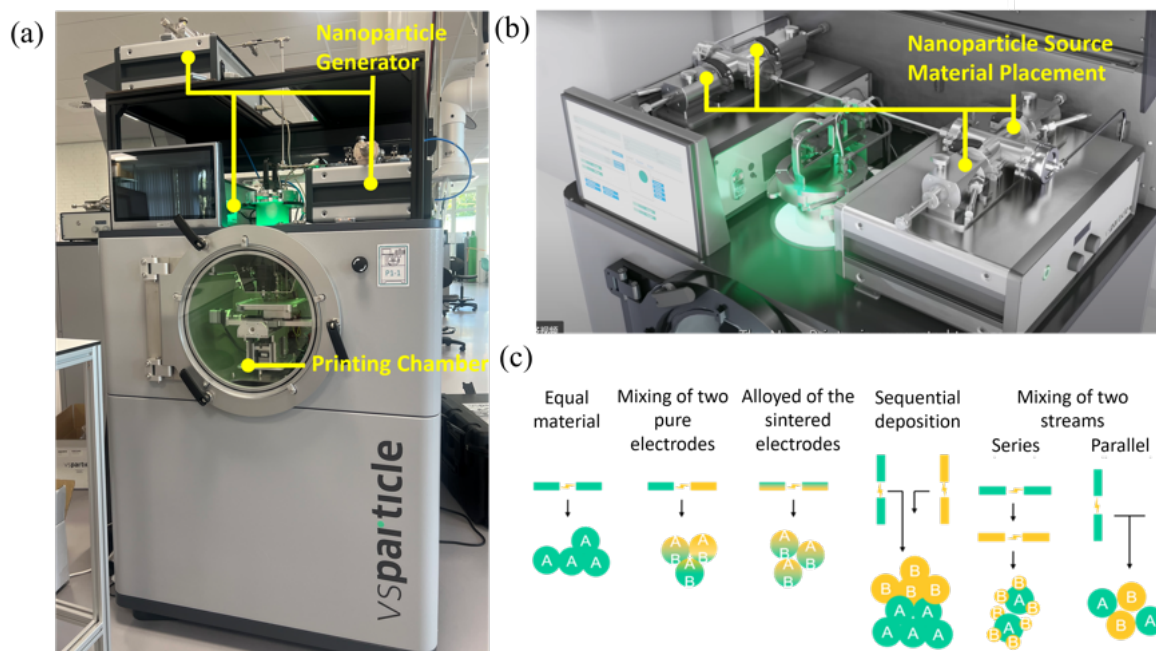


Figure 3.2: (a) VSP-P1 NanoPrinter (b) Generator inside (c) Different configurations for printing [61]

3.2. Material Characterization

3.2.1. Scanning Electron Microscopy

Scanning electron microscopy (SEM) is a typical investigation tool in materials research. It can provide information about the structure morphology on a microscopic scale. First, an electron gun generates electrons with a thermionic emission or a field emission. Then these electrons interact with the sample's atoms, generating electrons because of collisions. These emitted electrons are then detected and processed to form an image.

The interaction of the primary electron beam with matter, as shown in Fig 3.3, mainly produces three types of electrons: back-scattered electrons, secondary electrons, and Auger electrons. Back-scattered electrons undergo elastic scattering, theoretically without energy loss. Therefore, most back-scattered electrons have energy similar to that of the primary electrons, resulting in an energy peak near E_0 . A higher atomic number will result in a greater number of back-scattered electrons. Secondary electrons are the result of inelastic collisions between the primary electrons and the atoms in the sample material. Due to these inelastic collisions, part of the primary electron's energy is absorbed. However, these lower-energy electrons can still move within the sample and ionize other atoms, generating secondary electrons. The movement of these secondary electrons within the sample is limited due to their low energy, resulting in a shallow escape depth typically below 5 nm. Such shallow depth can provide abundant surface morphology information. Based on the above process, the production of secondary electrons is highly related to the primary electrons' energy and the sample's density. In SEM, Auger electrons are not the primary imaging mechanism. The energy of Auger electrons is determined by the specific energy level differences of the electron shells the element. By detecting the energy of Auger electrons, elemental composition analysis can be performed,

which forms the basis of Auger Electron Spectroscopy (AES).

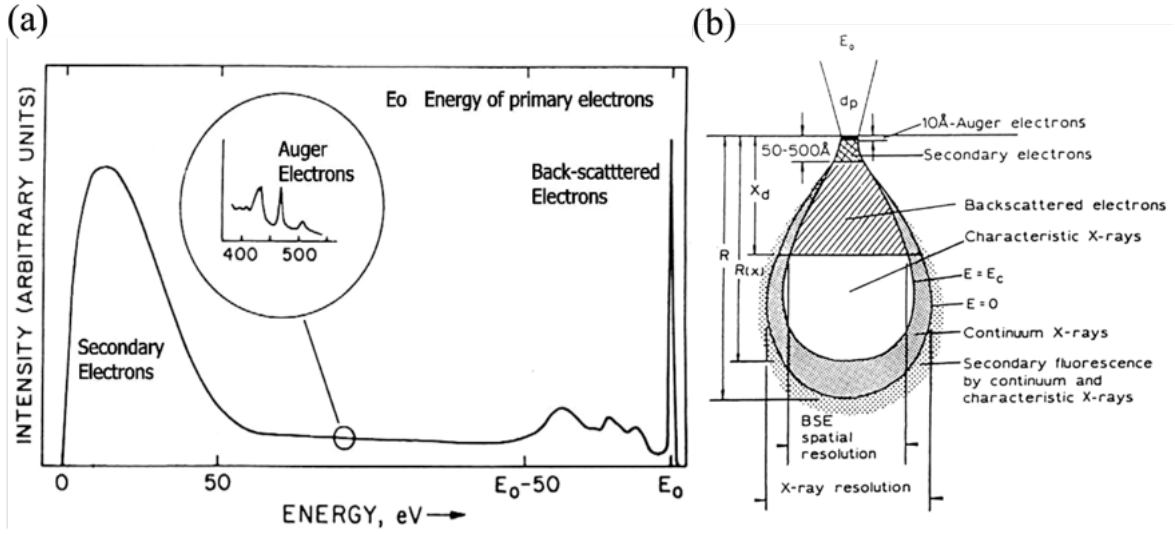


Figure 3.3: (a) The electron signal intensity varies with the energy of electrons escaping from the sample surface; (b) The electrons in different signals from various regions within the analysis volume. [62]

3.2.2. Image Processing

The coverage rate of the noble metal particles on a substrate can be calculated using a customized MATLAB script [63]. The imported images were captured using a scanning electron microscope (SEM Hitachi Regulus 8230) with a 1.5 kV beam at a magnification of 30,000x, 50,000x and 100,000x.

When importing these images into MATLAB, the SEM image will first be cropped from its original resolution of 1280x960 pixels to 1280x860 pixels. This cropping removes the scale bar from the image. The jpg image is then converted to an 8-bit bmp grayscale file. This format ensures the pixel intensities are within a range of 0 (black) to 255 (white). The intensity of each pixel is then calculated. With a well-chosen intensity threshold, this grayscale image is converted to a binary image. For binary images, each pixel value is either 0 (black) or 1 (white). In this case, for the SEM image to be analysed, the nanoparticles have a pixel value of 1 (foreground) while the silicon is 0 (background). The coverage of the particles in the substrate can be derived by calculating the percentage of pixel points with 1.

The core of this process is to find the optimal threshold to classify the pixels in an image into foreground and background categories. This can be accomplished by MATLAB's built-in function 'graythresh'. This function computes the global threshold from a grayscale image based on Otsu's method [64]. It calculates the between-class variance σ_B corresponding to each possible threshold t as shown in Eq. 3.1.

$$\sigma_B^2(t) = W_B(t)W_f(t)[\mu_b(t) - \mu_f(t)]^2 \quad (3.1)$$

- W_b and W_f are the foreground and background pixels weights, respectively.
- μ_b and μ_f are the mean intensities of the foreground and background pixels, respectively.

The σ_B measures the difference in means between the foreground and background. Therefore, a larger σ_B indicates a clearer distinction between these classes, resulting in better classification. To sum up, Otsu's method selected a threshold that maximizes the σ_B . In the case of scanning electron microscope (SEM) images, some nanoparticles may not have clear boundaries with the background due to their blurry edges. Therefore, finding an optimal threshold is crucial for distinguishing nanoparticles from the background. Moreover, using the MATLAB script eliminates human error and establishes a consistent standard for processing all images.

However, in practical applications, the MATLAB script was found unsuitable for calculating Ag particles. For instance, as shown in Fig 3.4, smaller particles around the silver particles are visible in the SEM image to the naked eye but are challenging for the code to identify.

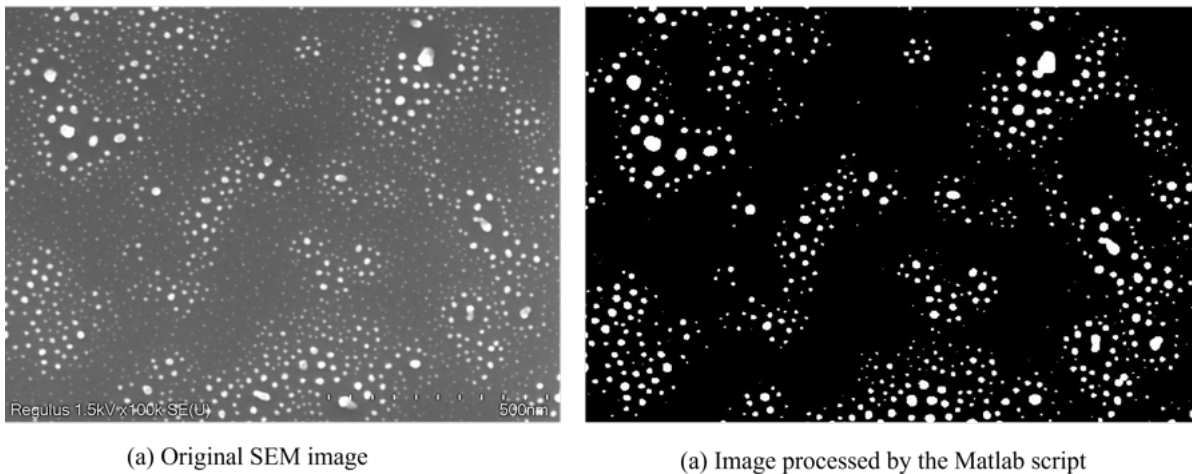


Figure 3.4: Unsuitable image processed before and after using the Matlab script

To solve this problem, further processing of Ag SEM images was conducted using ImageJ, where the threshold was manually adjusted, see Fig 3.5. The specific steps are detailed as follows:

1. Import the image into **ImageJ**. Navigate to **Image** → **Type** → **8-bit** to convert the image to an 8-bit format.
2. Under the **Image** → **Adjust** menu, select **Threshold** to manually adjust the threshold value, as shown in Fig 3.5(a).
3. Navigate to **Process** → **Binary** → **Make Binary** to convert the image into a binary format.
4. Select **Analyze** → **Analyze Particles** to get the surface density.

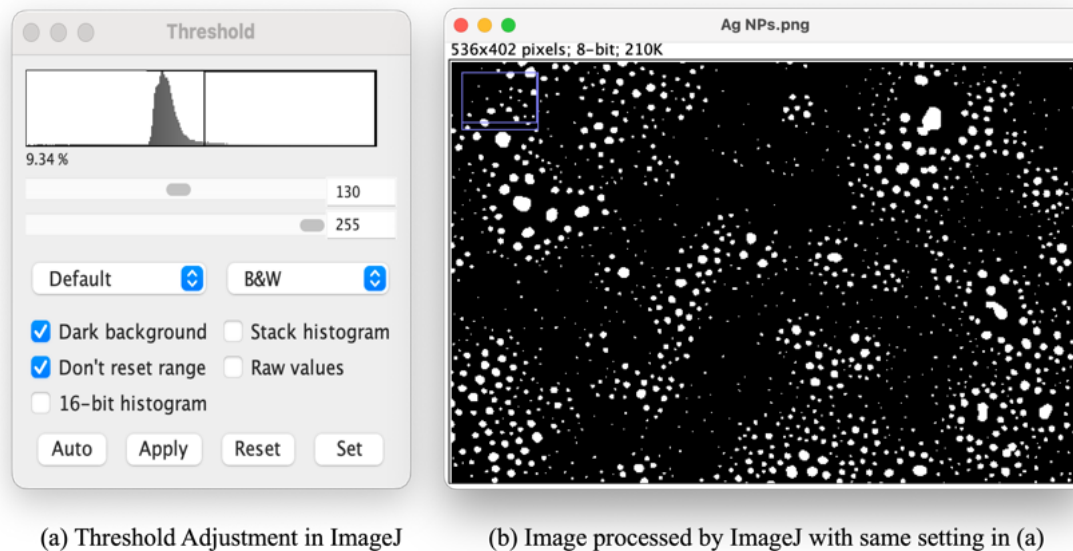


Figure 3.5: Image processed with ImageJ

3.2.3. X-ray Diffraction

XRD is a non-destructive technique that is commonly used in materials research. With the X-ray diffraction pattern, information about the crystal structure, lattice parameters, particle and crystallite size, measure stresses, stacking fault, and so on.

The wavelength of the X-ray is from 0.01 nanometers to 10 nanometers, which is similar to the spacing between atoms in the sample. This similarity allows X-rays to interact with the crystal lattice, leading to diffraction patterns. Bragg's Law is the fundamental principle governing this process in X-ray diffractometers. Diffraction only occurs when Bragg's Law is satisfied as the fig.3.6 shows

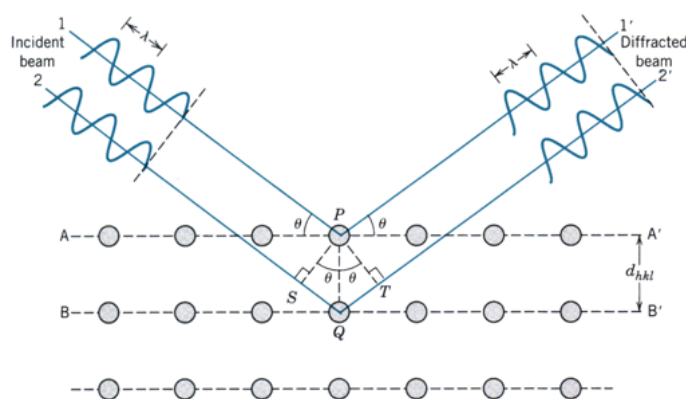


Figure 3.6: Diffraction of X-rays on a set of lattice planes with interplanar space.

The Williamson-Hall method can be used to calculate crystal size from XRD data. It assumes that peak broadening is caused by a combination of grain size and lattice strain, as Eq.3.2

shows.

$$\beta_T = \beta_D + \beta_\xi \quad (3.2)$$

In this formula, β represents the full width at half maximum (FWHM) of the XRD peak. The subscript T represents the total FWHM, the subscript D refers to the FWHM caused by the crystal grain size, and ξ represents the FWHM due to lattice strain.

According to Scherrer equation, the β_D can be presented by:

$$\beta_D = \frac{K\lambda}{D \cos \theta} \quad (3.3)$$

The strain can be presented by:

$$\beta_\xi = 4\xi \tan \theta \quad (3.4)$$

Substitute Eq.3.3 and Eq.3.4 into Eq.3.2, the Williamson-Hall equation could be written:

$$\beta_T \cos \theta = \xi(4 \sin \theta) + \frac{K\lambda}{D} \quad (3.5)$$

In this equation, K is the Scherrer constant, which is a function of crystal structure. For spherical particles, K is usually set as 1. λ is the X-ray wavelength, and θ is the diffraction angle. By plotting $4 \sin \theta$ against $\beta \cos \theta$ and fitting the data, the crystal size D can be calculated.

3.3. Functional Test

The gas testing setup was manually constructed and consists of three main components: the Owlstone gas sensor test system, the reaction chamber, and the electrical measurement instruments.

The gas testing is conducted using the Owlstone gas sensor test system, which consists of a V-OVG gas generator, an OHG-4 humidity generator, an OFC-1 additional dilution line, and a test chamber equipped with electrical feedthrough and a heater. The schematic of the gas flow is shown in Fig 3.7. In the CO₂ gas testing, the OFC-1 was used to control the flow of 'air', which was simulated as a mixture of 80% N₂ and 20% O₂. The OHG-4 humidity generator can provide relative humidity levels from 10% to 99% ($\pm 1\%$), enabling the testing of device sensitivity to varying humidity concentrations. An external CO₂ bottle with a 5% concentration in N₂ was also connected, with the gas diluted by air. Different gas concentrations can be achieved in subsequent tests by adjusting the flow rates of the OFC-1 and the CO₂ bottle.

The platform in the reaction chamber can accommodate a 2 cm \times 2 cm chip and features 25 probes on each side, spaced 800 μ m apart. These probes can be used as voltage/current sources and for voltage, current, or resistance measurements. Additionally, the platform can be heated up to 200°C to provide the necessary operating temperature for gas sensors.

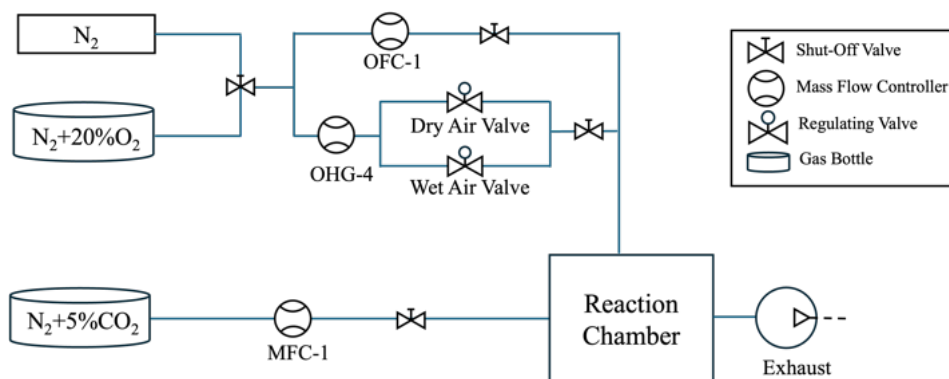


Figure 3.7: Schematic of the gas flows

The Keithley 2612B is used here for sourcing and measurement. It supports single- and dual-channel configurations, with a maximum current source/measure range of 10 A and a maximum voltage source/measure range of 200 V. To enhance testing efficiency, the Keysight 34901A Multiplexer Module is connected to the Keithley 2612B. This configuration allows for simultaneous testing of up to 20 channels.



(a) Owlstone gas sensor test system



(b) Keithley 2612B with 34901A Multiplexer

Figure 3.8: Main components of the gas sensing setup

3.4. Summary

In this project, the VSP-P1 is used to synthesize nanoparticles. SEM and XRD are employed for material characterization. SEM is used to analyze the surface morphology and particle size distribution of the synthesized noble metal NPs, providing detailed imaging at the nanoscale. Through XRD, the crystal structure, phase composition, and crystallinity of the materials can be determined. The crystal size can also be calculated using the Williamson-Hall method. The Owlstone, together with the Keithley, are assembled for the gas-sensing test. Two gas cylinders are prepared: one is 5% CO₂ + N₂, and the other is 20% O₂ + N₂.

4

Device Design and Fabrication

This chapter outlines the device design and the fabrication process depicted. The fabrication process consists of two main parts: the Au electrode fabrication conducted in the clean room, and the final step entails nanoparticle printing using the VSP-P1, performed at the company.

4.1. Mask Design

To transfer the gold electrode pattern to the substrate, a mask is required for the fabrication. In this project, the software kLayout is used here to draw the pattern.

In MEMS-based gas sensors, electrodes contact directly with the sensing materials and transmit the resistance signals of the sensing materials. The interdigitated electrode (IDE) is a common structure for gas sensors, as Fig 4.1 shows. It allows a bigger contact area within a limited area and avoids damage to the sensing materials as the sensing material is deposited after the fabrication of the electrode. In the following design, the finger width is fixed at $5\ \mu\text{m}$, and the finger length is $1\ \text{mm}$. As the four-probe electrode configuration is employed, the interdigitated structure is connected at its extremities to two separate electrodes. Therefore, the term 'Fingers per electrode' cited in the Table 4.1 and Table 4.2 should be interpreted as fingers per pair of electrodes.

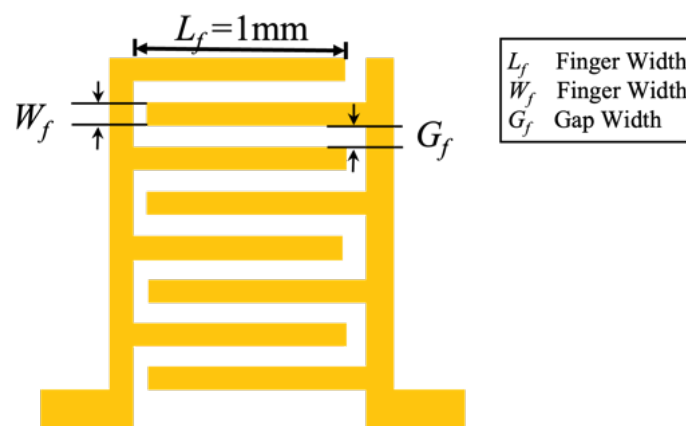


Figure 4.1: Typical structure of the interdigitated electrode (IDE)

4.1.1. IDE Configurations

In Design A and Design B, the contact pad is designed with dimensions of $200\mu\text{m}$ by $200\mu\text{m}$ which can be directly used with a microprobe.

Design A

Design A consists of 12 IDE structures, each with electrodes of unique dimensions. This design is configured to study the effects of electrode characteristics, such as finger width and contact area, on gas sensitivity. The detailed specifications of each electrode pair within Design A are provided in Table 1.

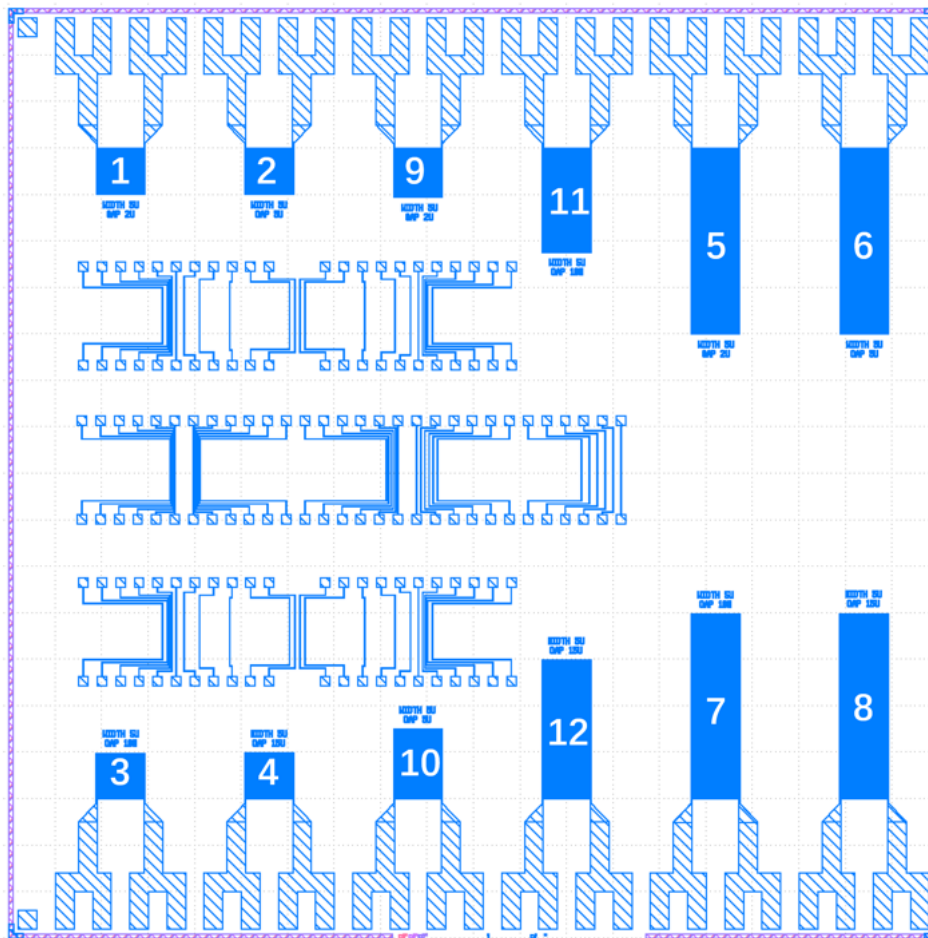


Figure 4.2: layoutA

Electrode pair	Finger Gap [μm]	Finger length [mm]	Total width [mm]	Fingers per electrode	Real length [mm]	Area per electrode [mm^2]
1	2	1	1	71	992	0.355
2	5	1	1	50	995	0.25
3	10	1	1	33	980	0.25
4	15	1	1	25	985	0.125
5	2	1	4	286	4002	1.43
6	5	1	4	200	3995	1
7	10	1	4	133	3980	0.665
8	15	1	4	100	3985	0.5
9	2	1	1.05	75	1048	0.375
10	5	1	1.5	75	1495	0.375
11	10	1	2.25	75	2240	0.375
12	15	1	3	75	2985	0.375

Table 4.1: Specifications of sensing device electrodes present in design A

Design B

There are two identical quarters in Design B, as illustrated in Fig.4.3. The electrode specifications of the IDE structures within each quarter are detailed in Table 2. This design is intended to verify the reproducibility of the sensing performance when using the same sensing material on identical devices.

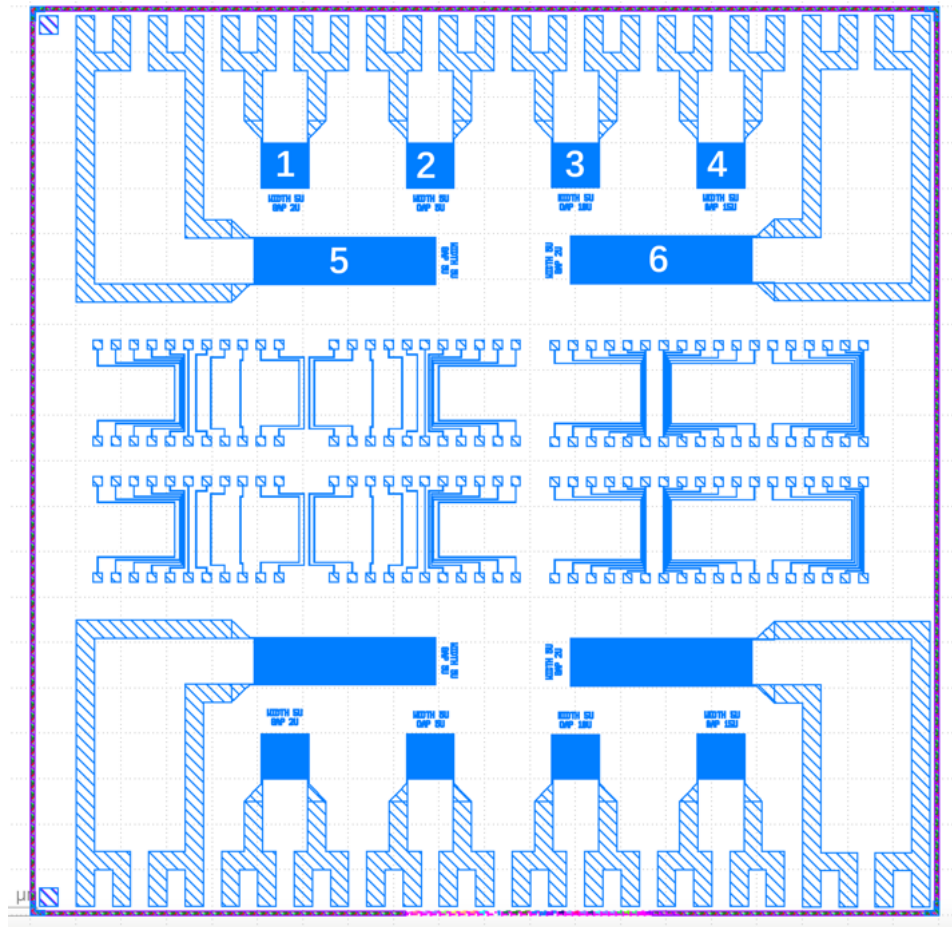


Figure 4.3: layoutB

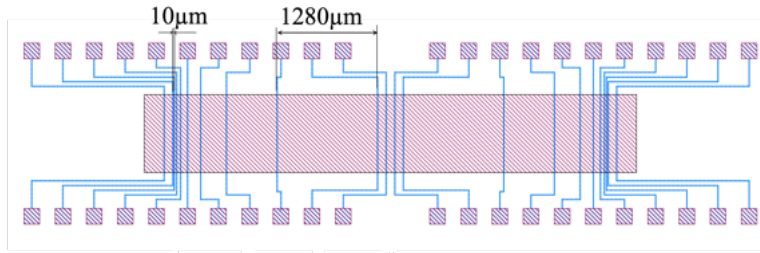
Electrode pair	Finger Gap [μm]	Finger length [mm]	Total width [mm]	Fingers per electrode	Real length [mm]	Area per electrode [mm^2]
1	2	1	1	71	992	0.355
2	5	1	1	50	995	0.25
3	10	1	1	33	980	0.25
4	15	1	1	25	985	0.125
5	2	1	4	286	4002	1.43
6	5	1	4	200	3995	1

Table 4.2: Specifications of sensing device electrodes present in design B

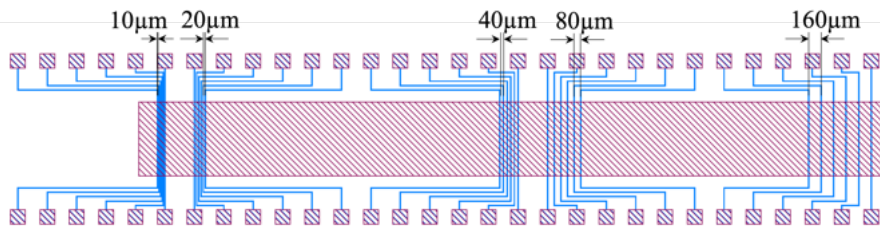
4.1.2. TLM Structure

Fig 4.4 shows the detail of the Transmission Line Model (TLM) structure. The first part is characterized by varying distances between electrodes, which is explained in Table 4.3. This configuration is used to deduce the sheet resistance of the nanoparticle layer. Fig 4.4b presents a TLM structure with uniform electrode spacings, which detect uniformity issues across a printed line by facilitating measurement across a consistent distance. Note: No space to set the mirror-

like structure for this TLM group. Additionally, each electrode possesses a line width of $10\ \mu\text{m}$.



(a) mirror-like TLM structure with varying distance



(b) 5 groups of TLM structure with same distance

Figure 4.4: Detail of the Transmission Line Model (TLM) structure

Electrode pair	Spacing width [μm]
1	10
2	20
3	40
4	80
5	160
6	320
7	640
8	1280

Table 4.3: Varying distances of the mirror-like TLM structure in Fig 4.4(a)

4.2. Fabrication Process

The fabrication process is mainly divided into two stages as Fig 4.5 shows: the cleanroom work for constructing metal electrodes and the later stage of target metal printing. The initial work follows cleanroom protocols and is completed according to the flowchart in Appendix.A. In the later stage, metal printing is carried out using the VSP-P1 which is discussed below.

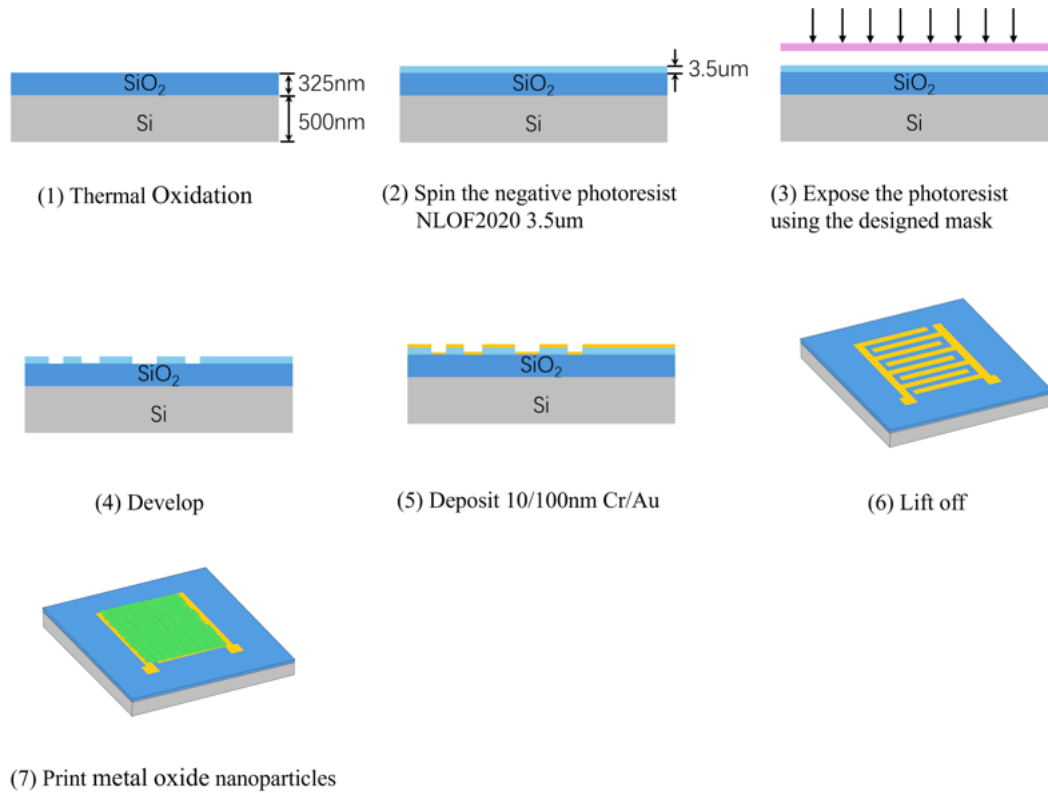


Figure 4.5: Fabrication Process

4.2.1. Clean Room Fabrication

The clean room fabrication starts with four 4-inch p-type silicon wafers. First, thermal oxidation is applied to these four wafers. Wet oxidation is performed here to obtain a thin oxide layer on the Si wafer, which acts as an insulating layer. The thickness of these SiO_2 layers is measured by the Wollam Ellipsometer, see Table 4.4.

Wafer No.	Oxide Thickness [nm]
1	357
2	357
3	365
4	365

Table 4.4: Oxide thickness measured with Woollam Ellipsometer

Subsequently, a $3.5 \mu\text{m}$ thick negative photoresist layer is spun onto the SiO_2 layer. The photoresist is then exposed using a mask designed in section 4.1. It was observed that exposure energy of 88 J/cm^2 provided the best development results. For negative photoresists, the exposed areas undergo cross-linking and hardening, making them insoluble in the developer, while the unexposed areas dissolve. Therefore, when using an energy level of 55 J/cm^2 , the $2 \mu\text{m}$ gaps in the interdigitated structure were removed, indicating that the energy was too low, resulting in insufficient exposure. Conversely, if the energy is too high, it can lead to overexposure, causing the features to expand and lose definition, thus affecting the precision of the

pattern.

Finally, a 10 nm layer of Cr and a 100 nm layer of Au are deposited. Cr is used here to enhance the adhesion between the SiO₂ layer and the Au layer. Liftoff is then carried out using a NI555 heated bain-marie set to 50°C in an ultrasonic bath to obtain the Au electrodes.

4.2.2. Printing Speed Selection

As mentioned before, a VSP-P1 is used to print the sensing layer. The sensing layer is mainly the SnO₂ layer decorated with the noble metal nanoparticles Ag, Ru on the surface. As the printing speed influences the layer significantly, primarily the thickness and the morphology, choosing the right printing speed is necessary. Several lines with a fixed length of 2000 μm are printed on silicon chips (1 cm*1 cm) with different speeds to find the optimal speed. The coverage is calculated using the Matlab script mentioned in the Chapter 3.2.2.

SnO₂

A thin SnO₂ layer is expected for this device. Five different speeds are tested here with a Dektak profilometer, applying a 3.00 mg force to the probe. The measurements are taken along the path indicated by the red line, as the Fig 4.6a shows. Thickness measurements were manually observed three times, and their average was calculated as shown in Table 4.5. The main objective of this step is to investigate the relationship between printing speed and both the thickness and width of the printed layer. This will help determine the optimal printing parameters, including speed and path. SEM is also used here as a complementary way to confirm the accuracy of the Dektak results at higher printing speeds.

Table 4.5 summarizes the thickness information obtained from Dektak and SEM. For Dektak, the average height is calculated as the mean of all height values within the peak range, automatically determined using Origin. The width information is not listed here because the line width at different printing speeds is approximately 200 μm. Dektak results show that excluding the 50 μm/s data point, the products of Speed × Peak Height and Speed × Average Height are approximately constant, around 80,000 and 50,000, respectively. However, the 50 μm/s data point deviates significantly from this trend. To verify the accuracy of the Dektak measurements, SEM was used to examine the cross-section. Fig 4.6bcd shows the thickness detail of lines with printing speeds of 200μm/s, 100μm/s, and 50μm/s. The results from SEM closely matched those obtained from Dektak.

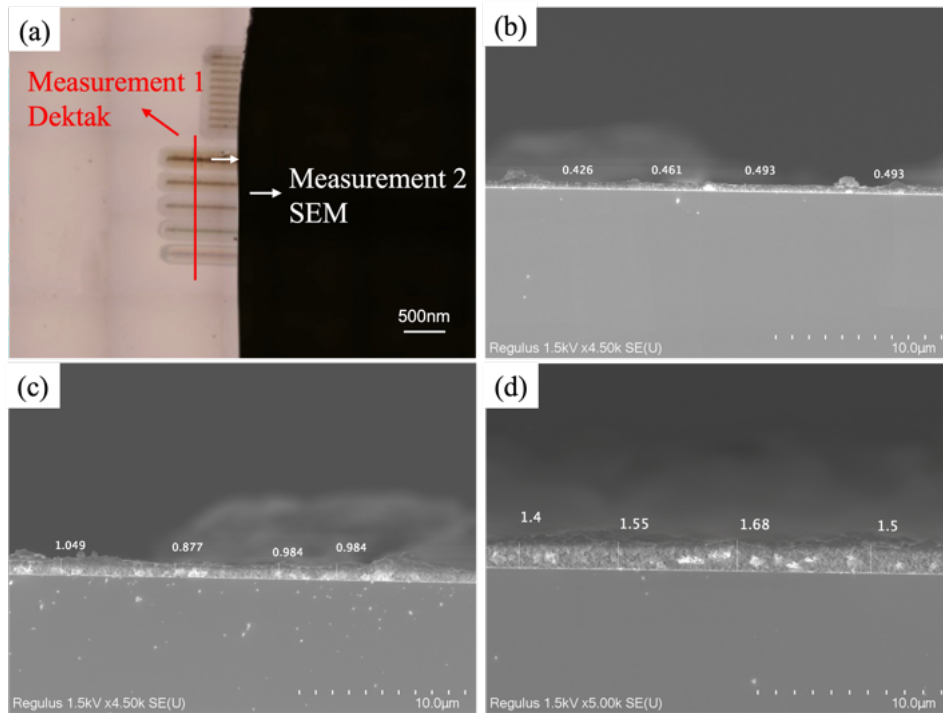


Figure 4.6: (a) Sample for measurement (b) 200 $\mu\text{m/s}$ (c) 100 $\mu\text{m/s}$ (d) 50 $\mu\text{m/s}$

Speed [$\mu\text{m/s}$]	Dektak		SEM
	Peak Height [μm]	Average Height [μm]	Thickness [μm]
10	8.1	4.5	
20	4.1	2.4	
50	1.5	0.7	1.5
100	0.8	0.5	1.0
200	0.4	0.3	0.5

Table 4.5: Height Trends with Different Speed

Normally, the film thickness of SnO_2 gas sensors ranges from a few hundred nanometers to several micrometres. Thinner films can accelerate the response time, while thicker films generally have better stability and durability. Considering these factors, a layer with a thickness of a few μm is expected. Therefore, a printing speed of 50 $\mu\text{m/s}$ is selected to form this layer, with lines printed every 100 μm . Since the line width is 200 μm , this 100 μm spacing helps to achieve a more uniform distribution. The detail of the printing toolpath is illustrated in Fig 4.7a. According to the Dektak measurement, the thickness of the sensing layer is around 2.5 μm .

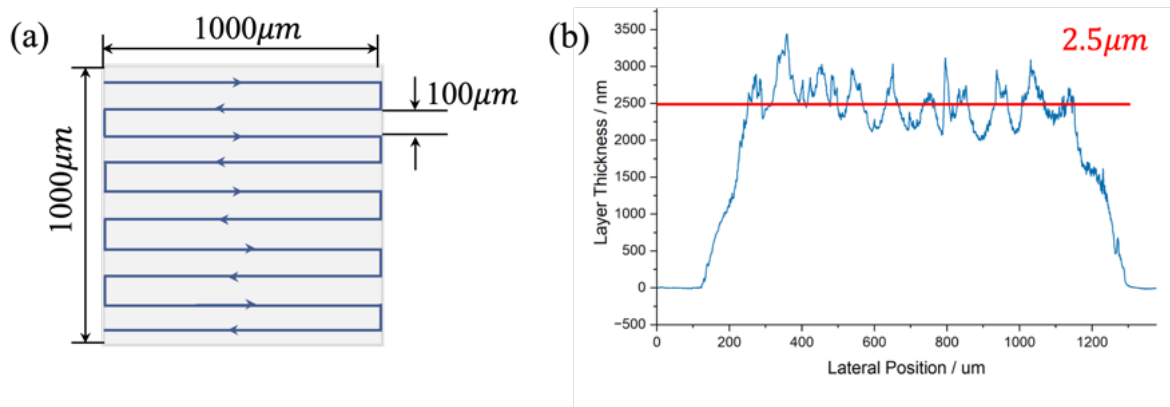


Figure 4.7: (a) Defined s-shape printing toolpath (b) Thickness of the printed square obtained from Dektak

Noble metal nanoparticle

Noble metal Ag and Ru NPs are used here as the surface-functionalized material. Therefore, it is expected to be dispersed and uniform nanoparticles instead of a layer which prevents the reaction between CO_2 and the SnO_2 sensing layer. To reduce the printing mass, lower power (1kV, 2mA) and faster speed are applied.

Fig 4.8 and Fig 4.9 shows the particle distribution with varying energy levels and speeds. From these two figures, it can be observed that the output mass of Ru is significantly greater than that of Ag, and there is a big difference in their morphologies. For example, the printed Ru particles tend to aggregate, forming porous agglomerates, whereas Ag particles are distributed individually. As mentioned before, the amount of nanoparticles used for surface modification needs to be optimal—not too little to be ineffective, nor too much to cover the entire sensing layer, which would potentially prevent CO_2 from interacting with SnO_2 . Therefore, an energy setting of 1 kV and 2 mA was selected for this experiment. For Ru, printing speeds of 2000 $\mu\text{m/s}$ and 3000 $\mu\text{m/s}$ were found to be more appropriate, whereas for Ag, 1000 $\mu\text{m/s}$ or 2000 $\mu\text{m/s}$ were determined to be more suitable. In this study, a printing speed of 2000 $\mu\text{m/s}$ was selected for Ag and 3000 $\mu\text{m/s}$ for Ru. At these respective speeds, both types of particles achieved comparable surface coverage, with the surface density measured at approximately 19% for Ru and 12% for Ag, as confirmed through comparative analysis.

Fig 4.10 shows the surface coverage of Ru and Ag nanoparticles as a function of printing speed and power. The plot shows that Ag exhibits greater changes in surface coverage under the same variation in printing speed. This indicates Ag has a higher sensitivity to printing speed. For the linear fitting results, the R^2 values for Ru are higher with a stronger linear correlation. Overall, the error bars for the four datasets are relatively small, suggesting reliable linear fitting results. Therefore, the linear fitting data can be used to adjust the printing energy and speed to achieve the desired surface coverage.

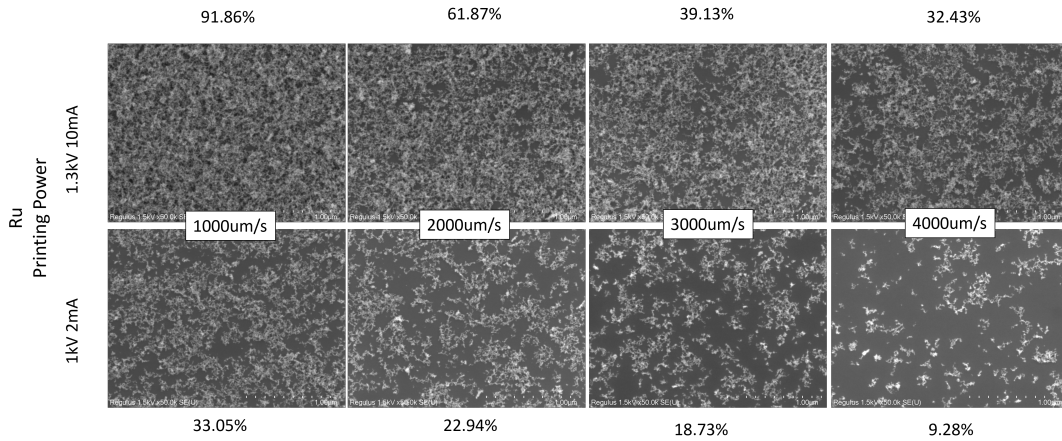


Figure 4.8: SEM images of the printed Ru NP taken from line samples of a silicon die (at 50,000 magnification). The percentages shown are the surface coverage

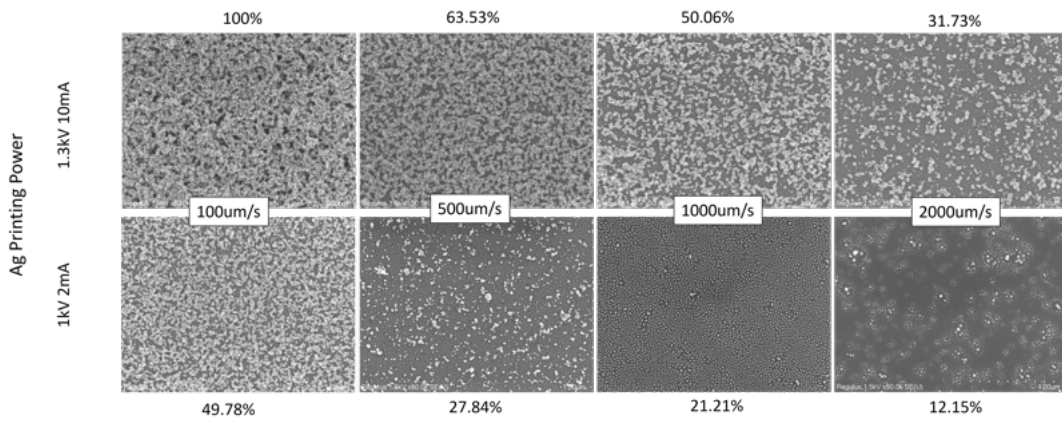


Figure 4.9: SEM images of the printed Ag NP taken from line samples of a silicon die (at 50,000 magnification). The percentages shown are the surface coverage

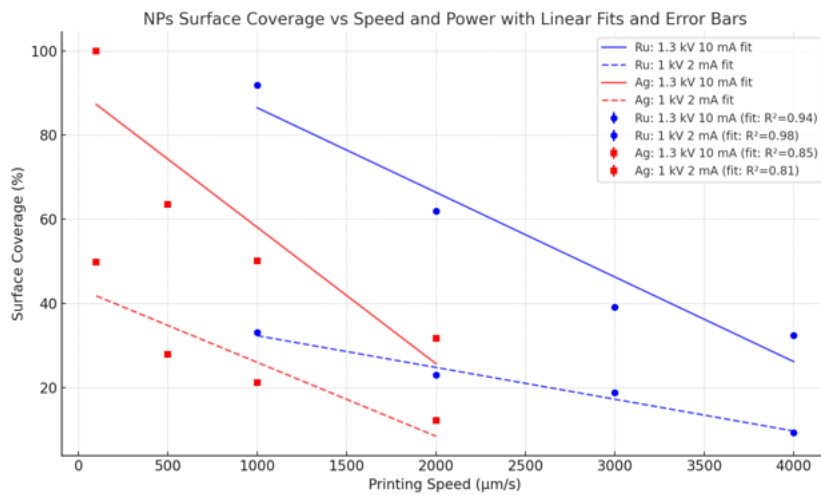


Figure 4.10: Surface Coverage of Ru and Ag Nanoparticles as a Function of Printing Speed and Power

4.3. Summary

This chapter begins with mask design and introduces the cleanroom work to fabricate the gas sensor, along with the optimization of related printing parameters. The final printing parameters were determined as follows: for tin, a printing speed of 50 $\mu\text{m/s}$ was selected with 1.3 kV and 10 mA; for Ag, a printing speed of 2000 $\mu\text{m/s}$ was used; and for Ru, a speed of 3000 $\mu\text{m/s}$ was chosen, both with 1 kV and 2 mA. A total of four chips were fabricated, including two chips with pure SnO_2 , one SnO_2 chip decorated with Ag, and one SnO_2 chip decorated with Ru.

5

Annealing Conditions

The electrode material used in the VSP-P1 process is pure Sn. As a result, the printed sensing layer in the chamber is theoretically composed of Sn. Although Sn is prone to oxidation in the air, annealing is required to achieve a fully oxidized SnO₂ layer. Additionally, annealing can increase bulk and surface oxygen vacancies, enhancing free electron generation and providing more active sites on the material's surface, which promotes oxygen chemisorption[65]. Based on the literature research in Chapter 2, the annealing temperature for SnO₂ is normally from 400°C to 600 °C. The fabricated chips were divided into two groups, with annealing temperatures set at 450°C and 600°C, respectively. The detail of these chips and devices in each chip is shown in Table 5.1 and Table 5.2.

Chip.No	Printing NPs
C600 C450	SnO ₂
C600-Ag	Ag NPs on SnO ₂
C600-Ru	Ru NPs on SnO ₂

Table 5.1: Chips Number and Printing Conditions

Device.No	Area/mm ²	Gap Width/μm
1	1	15
2		10
3		5
4		2
5	4	2
6		5

Table 5.2: Device Number and its configuration

5.1. Material Characterization

5.1.1. SEM Results

Fig 5.1 shows the SEM images of the sensing layer before and after annealing. Fig 5.1b provides an in-situ magnified view of the black box area highlighted in Fig 5.1a. In these two figures, a melting phenomenon is observed in the unannealed samples. This can be attributed to the existence of pure tin in the sensing layer and the exposure to the electron beam. Fig. 5.1f shows that after annealing at 600°C, the diameter of the nanoparticles is approximately 12 nm, with clearly defined boundaries. In contrast, for the sample annealed at 450°C, shown in Fig 5.1e, the particle sizes appear to remain within a smaller range. As the boundaries between

particles are less distinct, it is hard to determine the specific particle size directly from the SEM image.

Theoretically, when the surface of the printed tin layer is exposed to air, a thin, stable, and dense oxide layer of SnO or SnO₂ forms, which can act as a barrier to further oxidation. However, the observed melting suggests that this oxide layer either did not form completely or was not sufficient to prevent deeper oxidation of the tin. Considering the melting points of Sn (232°C) and SnO₂ (1630°C), it is speculated that under the applied voltage of 1 kV, localized heating occurred, causing the unoxidized Sn beneath the surface to melt. This implies that the tin was not fully oxidized in the unannealed samples. This phenomenon has also been observed in the work of Esad[7].

In contrast, the samples annealed at 450°C and 600°C do not exhibit this phenomenon. This indicates that the tin underwent complete oxidation during the annealing process, forming SnO₂ and eliminating the unoxidized Sn responsible for the melting. According to the gas sensing mechanism discussed in Chapter 2, a stable n-type SnO₂ sensing layer is essential for reliable CO₂ gas sensing performance. This highlights the critical role of achieving complete oxidation during post-treatment.

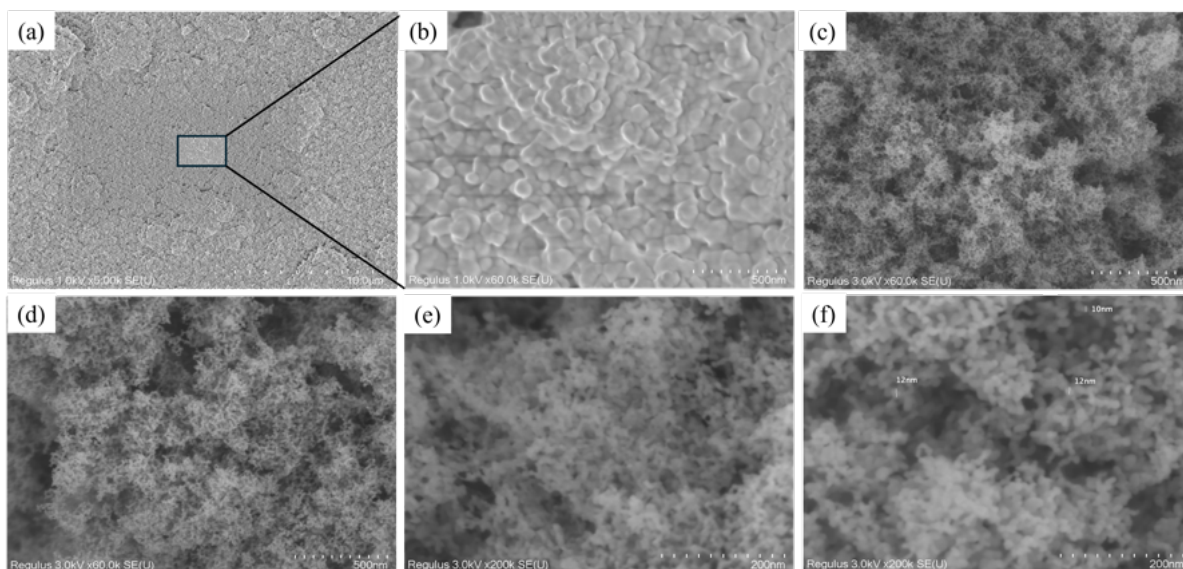


Figure 5.1: SEM Images of Samples before and after annealing (a) Before Anneal, x 5k (b) Before Anneal, x 60k (c) Anneal at 450°C, x 60k (d) Anneal at 600°C, x 60k (e) Anneal at 450°C, x 200k (f) Anneal at 600°C, x 200k

5.1.2. XRD Results

The SEM results reveal the changes in Sn before and after annealing. To further explore these observations, XRD analysis was performed to confirm the phase composition and oxidation state of Sn in the samples. Considering that XRD analysis requires a substantial sample mass, a printing speed of 100 $\mu\text{m/s}$ was employed to deposit 10 layers of SnO₂.

Before Annealing

As mentioned before, the XRD results should primarily show Sn with some SnO_2 . However, the XRD results indicate that the printed material is not pure tin but almost a metal oxide. In this XRD pattern, the red vertical lines represent the standard diffraction peaks of SnO_2 (cassiterite phase), which fits the black curve. Additionally, the shape of this curve shows significant background noise. The background noise could be attributed to the amorphous phase of the sample or irregular structures on the sample surface, both of which suggest a lower degree of crystallinity.

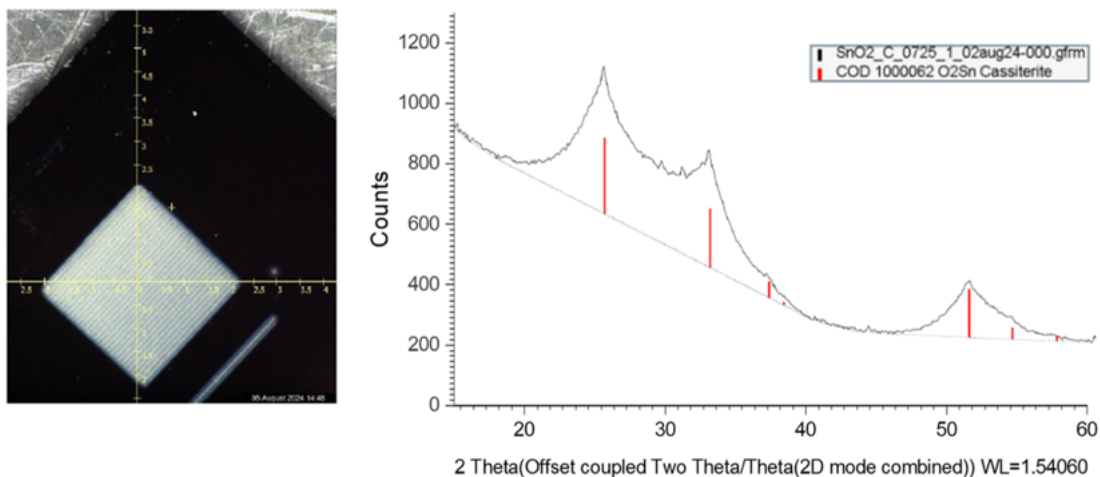


Figure 5.2: XRD results of the sample before annealing

After Anneal

The spectra of SnO_2 show good consistency with the XRD results of samples after annealing at 450°C . The blue lines indicate the standard peaks of SnO (tin(II) oxide) and there are no significant corresponding peaks in the black curve, suggesting that very little SnO is present. Compared with the unannealed sample, the diffraction peaks are more intense and sharper. According to the Williamson-Hall equation, the crystal size is calculated to be 7 nm.

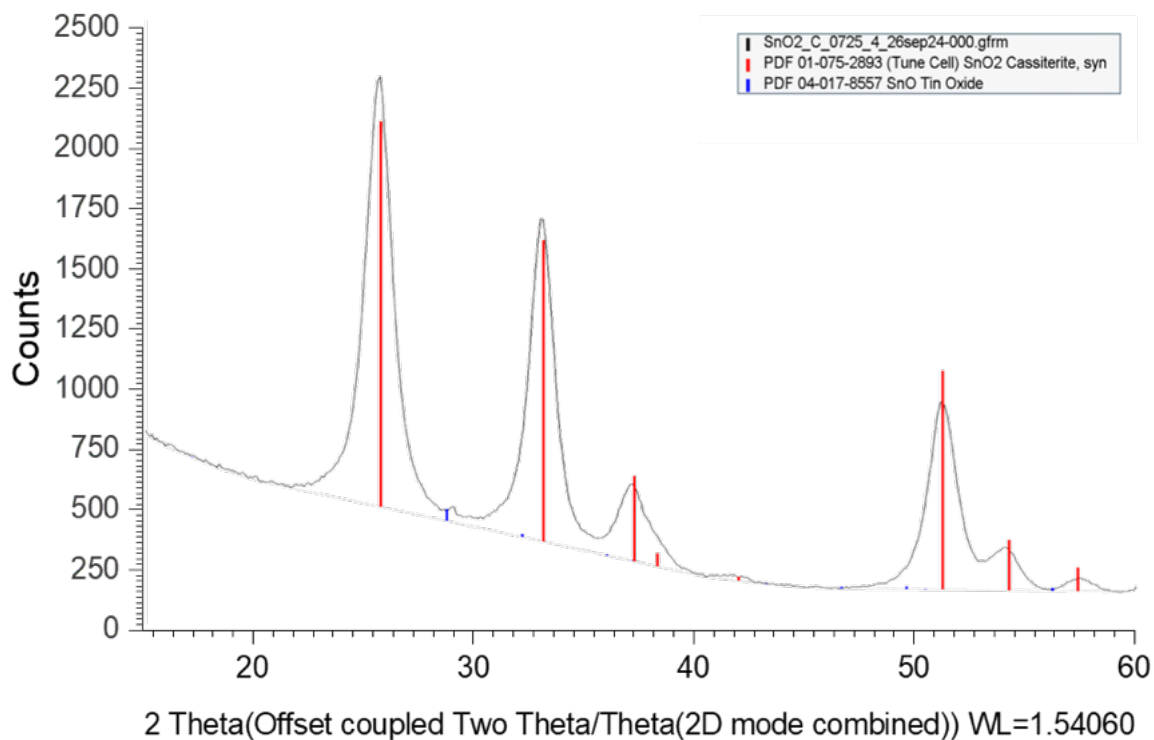


Figure 5.3: XRD results after annealing at 450°C

After annealing at 600°C, the spectra of SnO₂ show excellent agreement with the XRD results. Compared with the sample annealed at 450°C, the diffraction peaks become more intense and sharper, implying an increase in crystallite size and improved crystallinity due to annealing. The crystal size was calculated to be 12 nm using the Williamson-Hall equation. This further proved crystal growth at the elevated annealing temperature.

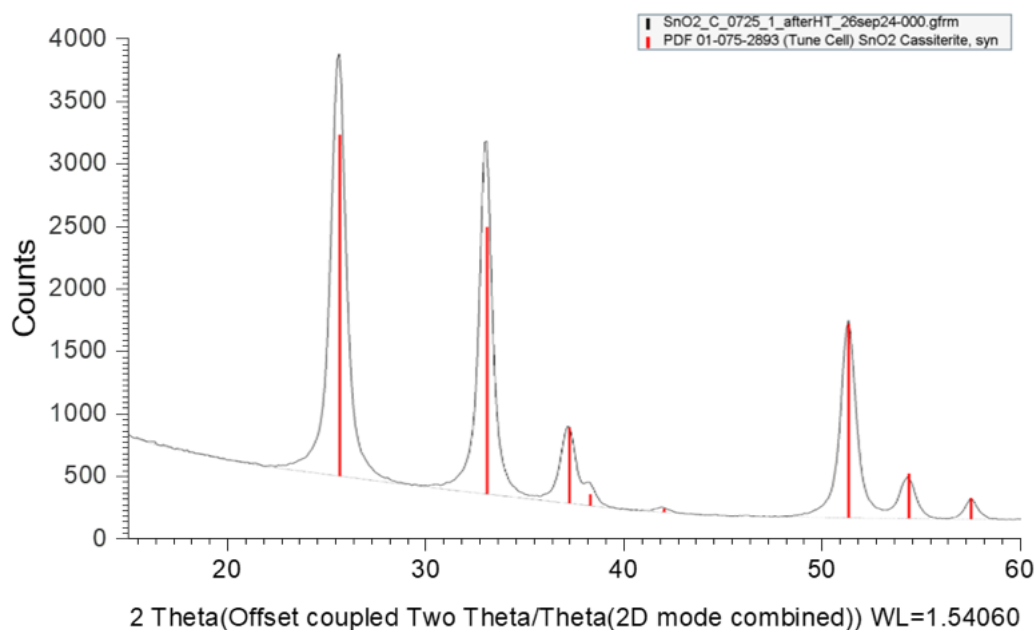


Figure 5.4: XRD results after annealing at 600°C

5.2. Electricity Properties

As mentioned in Chapter 4.1, devices with different surface areas were designed: one with a small area of $1\text{mm} \times 1\text{mm}$ and another with a larger area of $1\text{mm} \times 4\text{mm}$. These devices were measured using a two-probe configuration on the Cascade probe station with a B1500A semiconductor parameter analyzer, with a voltage sweep from -20V to 20V .

The unannealed samples exhibited unstable electrical performance. The current-voltage characteristics showed two types of behaviour: one resembling a Schottky diode and the other displaying a linear relationship, as shown in Fig 5.5.

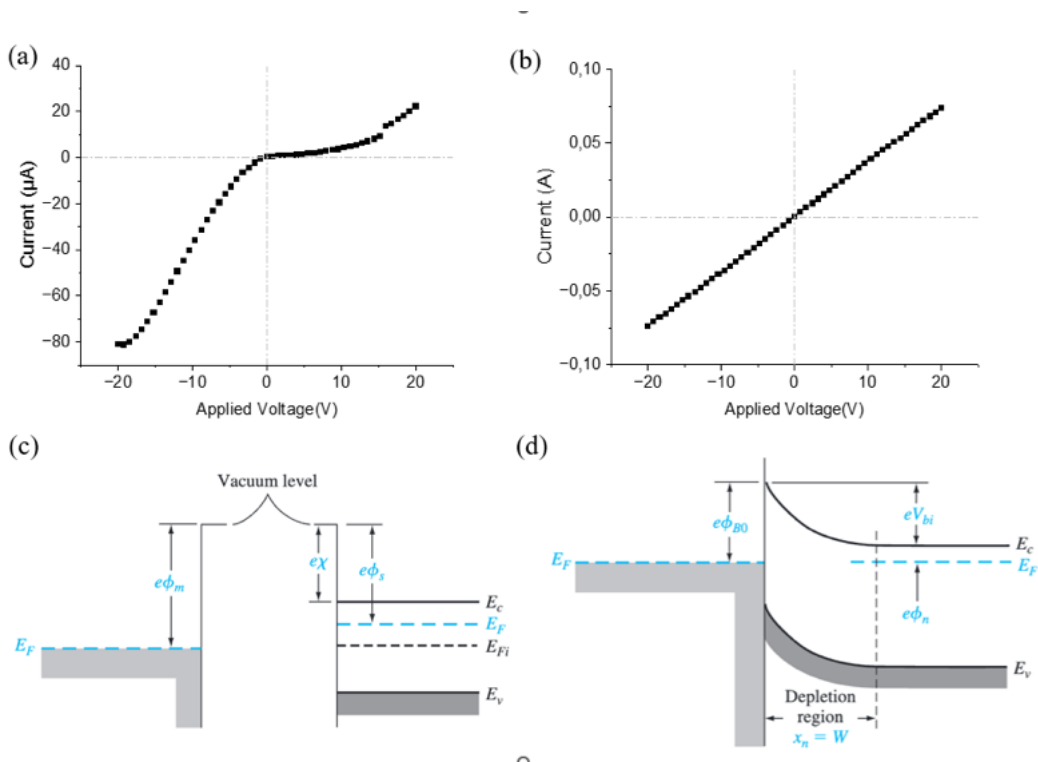


Figure 5.5: (a) V-I relation $1\text{mm} \times 1\text{mm}$, $\text{gap}=2\mu\text{m}$ (b) V-I relation $1\text{mm} \times 4\text{mm}$, $\text{gap}=2\mu\text{m}$ (c) Energy-band diagram of a metal and semiconductor before contact; (d) ideal energy-band diagram of a metal-n-semiconductor junction for ϕ_m and ϕ_s [66]

Previous XRD results indicated that the printed device is not pure Sn but rather an oxide of Sn. The work function (Φ_m) of SnO_2 is usually from 4.4eV to 4.9eV while the Au (χ) is around 5.1eV to 5.47eV . The difference ($0.2\text{eV} \sim 1.07\text{eV}$) between SnO_2 and Au leads to the formation of the Schottky barrier at the interface, as Fig 5.5cd shows. Therefore, the Schottky diode-like behaviour is reasonable. However, due to the significant instability of unannealed samples, devices with the same configuration often exhibit large variations in measurement results for this Schottky-like behaviour, see Appendix C.

The linear relationship only appears in the 4mm^2 device, while all the 1mm^2 devices exhibit characteristics similar to a Schottky diode. To explain the difference in the electrical performance of samples with different areas, it is important to investigate the oxidation process of the thin film. According to the study by P. A. Chernavskii et al.[67], the oxidation behaviour

of metal nanoparticles is significantly influenced by particle size, surface-area-to-volume ratio, and oxygen diffusion rate. The more severe oxidation observed in smaller-area devices may be attributed to the following two primary factors: First, the model presented by P. A. Chernavskii et al. suggests that the activation energy (E_a) for oxidation can be affected by the distribution of defects on the particle surface. In the 1 mm^2 device, the higher edge effects and defect density provide more active sites on the particle's surface. These active sites effectively lower the activation energy (E_a) of the oxidation reaction, thereby accelerating the process, resulting in a bigger oxidation rate (k). This rate can be described by the Arrhenius equation Eq 5.1. In this equation, A is the pre-exponential factor related to molecular vibrations, R is the gas constant ($8.314 \text{ J/mol}\cdot\text{K}$) and T is the absolute temperature. Second, the more severe oxidation in the 1 mm^2 device can also be attributed to the shorter oxygen diffusion path. In the 1 mm^2 device, the smaller total area results in a shorter diffusion path, allowing oxygen to penetrate more quickly into the interior of the thin film. Consequently, the oxidation process in the smaller device becomes more uniform and rapid.

$$k = A \exp\left(-\frac{E_a}{RT}\right) \quad (5.1)$$

The annealed samples all exhibit current-voltage behaviour similar to a Schottky diode. Compared with the ones before annealing, Schottky diode characteristics of these annealed samples are more stable and evident, as shown in Fig 5.6. The configuration of Device No.4 and No.5 can be checked in Table 5.2.

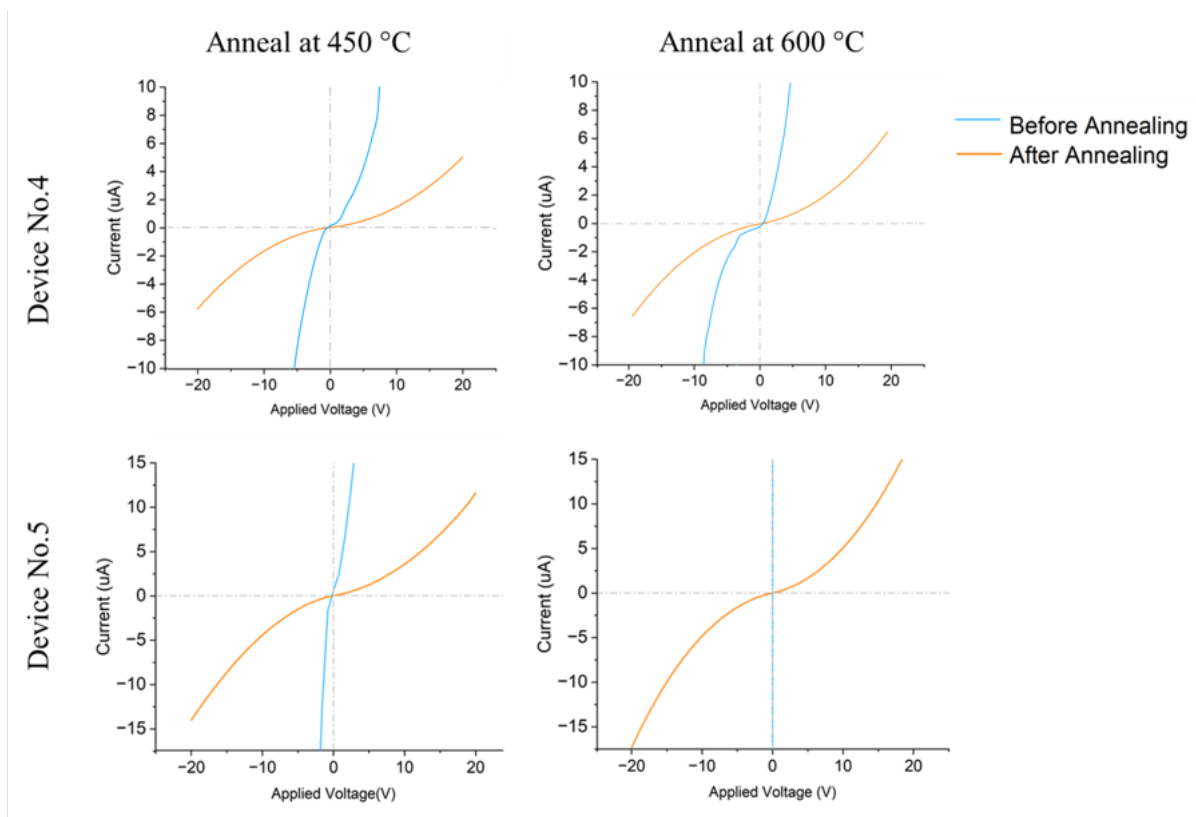


Figure 5.6: V-I relation of the device annealed at 450°C and 600°C

Table 5.3 lists the resistance results obtained through linear fitting within the range of 10V to 20V (the VI graphs can be found in Appendix C). This range is chosen because the I-V curve in this region is more linear, allowing for more accurate and reliable resistance calculations. From Table 5.3, it can be concluded that as the annealing temperature increases, the resistance in the linear region decreases. Additionally, the resistance values before annealing are not included in the table because, for most devices, the V-I relationship before annealing exhibits significant nonlinearity, as Fig 5.5a shows, making it unsuitable for effective resistance extraction through a linear fitting.

Device No.	Resistance[M Ω]	
	Anneal at 600°C	Anneal at 450°C
1	1.73	3.5
2	1.61	2.6
3	1.53	2.3
4	2.2	2.8
5	0.79	1.2
6	0.65	1.2

Table 5.3: Resistance Results Derived from 10V-20V Linear Fit (Related V-I graphs are listed in Appendix C)

5.3. Au electrode

After annealing, the samples were examined under an optical microscope. All six appeared similar to Fig 5.7a, with many black spots on the gold electrodes. SEM analysis revealed that these black spots had the structure shown in Fig 5.7b. To explore the cause, the samples were heated in a furnace at temperatures ranging from 300°C to 600°C, with a 100°C increment, and held at each temperature for two hours. The black spots started appearing on the gold electrodes at 400°C and above. It was suspected that high temperatures might have damaged the adhesion of the Cr layer or there is something wrong in the fabrication process. To test this, the new group of gold electrodes were redeposited using a CHA evaporator and subjected to the same heating conditions. The new samples remained stable and free of black spots. This points to a possible issue with the Cr layer in the earlier batch, which may have caused the adhesion to fail.

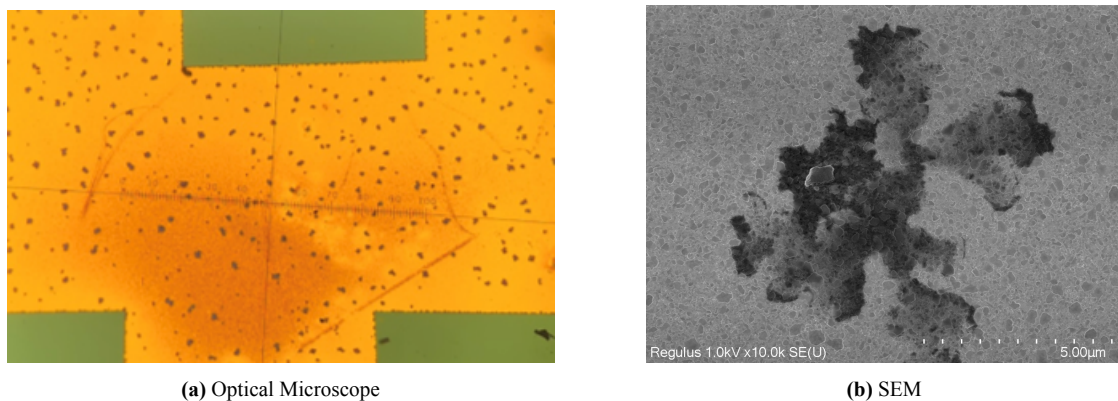


Figure 5.7: Au electrode after annealing

To further verify this, EDS analysis was performed on the gold electrodes. The results revealed that the black spots were rich in oxygen, and elements such as Si and Cr were also detected. This confirms that the black spots correspond to areas where the gold layer had delaminated, exposing the underlying layers. Despite the delaminated areas exposing the underlying layers, the majority of the gold electrode remains intact. Therefore, this delamination does not affect the electrical measurements mentioned above and the later gas-sensing test.

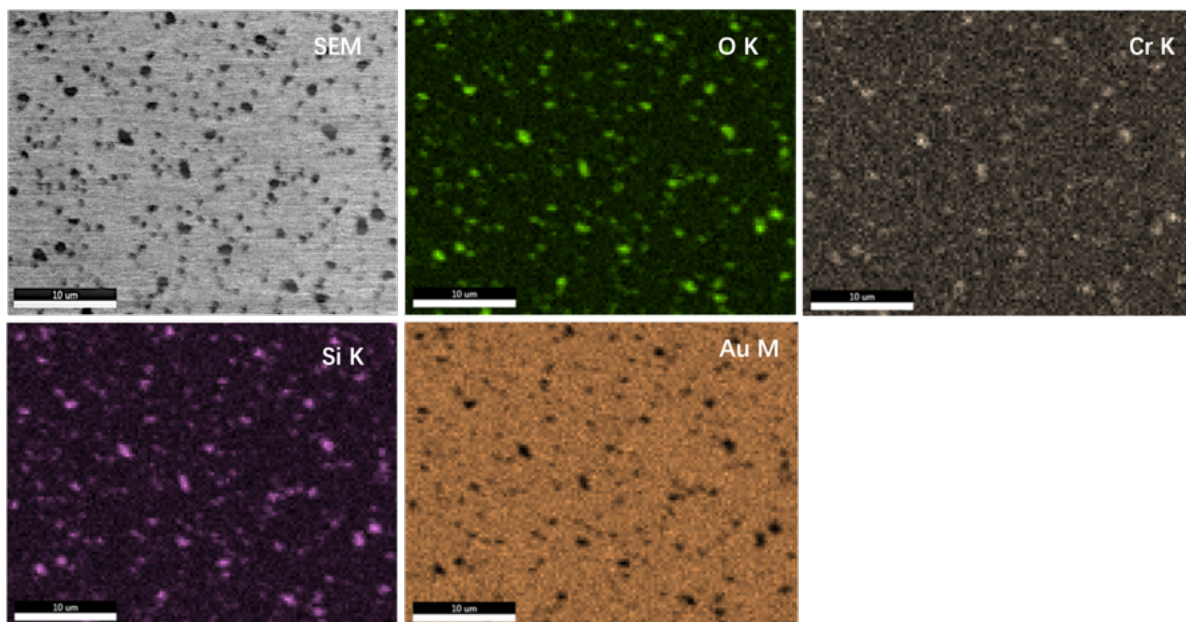


Figure 5.8: EDS mapping image.

5.4. Summary

XRD tests were performed on samples that were not annealed and those annealed at temperatures ranging from 450°C to 600°C. The results indicated that annealing led to an increase in crystallite size and improved crystallinity. Additionally, as the annealing temperature increased, grain size also grew from 7nm to 12nm. Electrical property tests revealed that annealed samples exhibited greater stability compared to unannealed ones, with minimal differences observed between samples annealed at 450°C and 600°C. However, some abnormalities were noted on the surface of the annealed gold electrode, though these did not affect the material's overall properties.

6

Results and discussion

During the experimental design phase, humidity control was taken into consideration. However, in practice, due to the high working temperature of 200°C, even with the OHG-4 humidity control set to its maximum, the relative humidity in the reaction chamber could only reach 50% at most. As a result, all experiments were conducted in a dry gas environment with a relative humidity of approximately 28%. All the results presented here were obtained using the four-probe measurement.

6.1. Response to CO₂

Chapter 2 discussed the mechanism of SnO₂ as a CO₂ gas sensor, where CO₂ reacts with preadsorbed oxygen ions, influencing the surface resistance. To verify the role of oxygen in this process, experiments were conducted under two different conditions: a pure N₂ atmosphere and a synthetic air atmosphere, to observe the resistance changes induced by CO₂. The response is defined by the formula:

$$\text{Response} = \frac{|R - R_{\text{CO}_2}|}{R} \times 100\% \quad (6.1)$$

Here, R refers to the resistance before introducing CO₂ for each pulse, While R_{CO₂} refers to the resistance in CO₂.

6.1.1. N₂ atmosphere

As Fig 6.1a shows, each cycle lasted 1 hour, with 30 minutes of N₂ and 30 minutes of 5% CO₂. It was observed that at a temperature of 200°C, the device can detect CO₂ until the detected CO₂ reaches saturation. However, as shown in Fig. 6.1, the entire process is irreversible. C450, C600, and C600-Ru all exhibit similar behaviour, see Fig D.1 in Appendix D. From the calculated response shown in Fig.6.1b, except for the first cycle, the responses of C450 and C600 are similar. In contrast, C600-Ru exhibits a higher response, approximately twice that of the undecorated sample, suggesting that Ru NPs decoration can enhance the sensitivity.

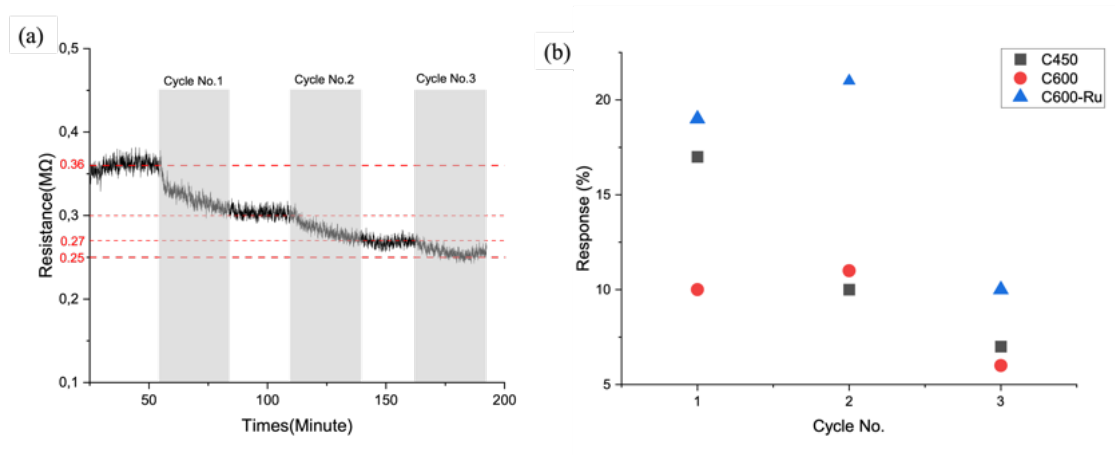


Figure 6.1: Response to CO₂ in N₂ atmosphere (a) C450, Device No.5 (b) Calculated response of Device No.5 of different samples

The irreversible behaviour can be explained as follows: According to the reaction mechanism described in Chapter 2, detection of CO₂ by SnO₂ requires surface-adsorbed oxygen as a prerequisite. However, under a nitrogen background, the contribution of surface oxygen ions can be largely excluded. Instead, this phenomenon could be attributed to the chemical reaction between CO₂ and lattice oxygen in SnO₂. According to research conducted by Song et al., some lattice oxygen reacts with CO₂ at high temperature to produce CO and form oxygen vacancies[68]. Although SnO₂ sensors have been extensively studied, most research has been conducted in the context of synthetic air. There is limited literature on CO₂ detection in an N₂ background.

The higher response of C450 compared to C600 can be explained based on the findings of Ke et al.[69]. Their study indicates that as the annealing temperature (above 500°C) increases, oxygen molecules can gain sufficient energy to react with under-coordinated Sn atoms, thereby reducing the concentration of oxygen vacancies. For SnO₂ layer decorated with Ru NPs, this Ru NPs contact helps to form a Schottky barrier at the interface, which facilitates electron transfer and further enhances the response performance to CO₂. To explain it in detail, the Schottky barrier generates a built-in electric field at the Ru-SnO₂ interface, driving electrons from the bulk region of SnO₂ to the surface. This electron migration increases the number of electrons available at the surface active sites, meeting the need for electrons during CO₂ adsorption and reactions. Therefore, these NPs can significantly enhance the sensing sensitivity and response speed of SnO₂ toward CO₂. This mechanism has been confirmed in the previous study[8].

6.1.2. Synthetic Air

In this experiment, each cycle lasted 1 hour, consisting of 30 minutes of exposure to 'synthetic air' followed by 30 minutes of 5% CO₂ exposure. Note that 'synthetic air' used here did not simulate real air conditions but consisted instead of 12% O₂ and 88% N₂, followed by the introduction of 2% CO₂. All chips exhibited similar behaviour, as shown in Fig 6.2. When CO₂ gas was introduced, a change was detected, but it was very small, nearly negligible.

Although literature indicates that pure SnO₂ thin films can respond to CO₂ at 200°C[70], the working temperature might have been too low in this project. According to Table 2.2 and Table 2.3, the working temperature for SnO₂-based sensing is generally 240°C or higher. Therefore, the temperature was increased to 250°C. However, the test results at 250°C showed significant noise, and a large rotation of the needle was observed. This could be attributed to the poor contact between the needle and the Au electrode, which resulted in significant noise, making the measurements nearly impossible to read, see Appendix D. To prevent further needle damage, subsequent measurements were conducted at 200°C.

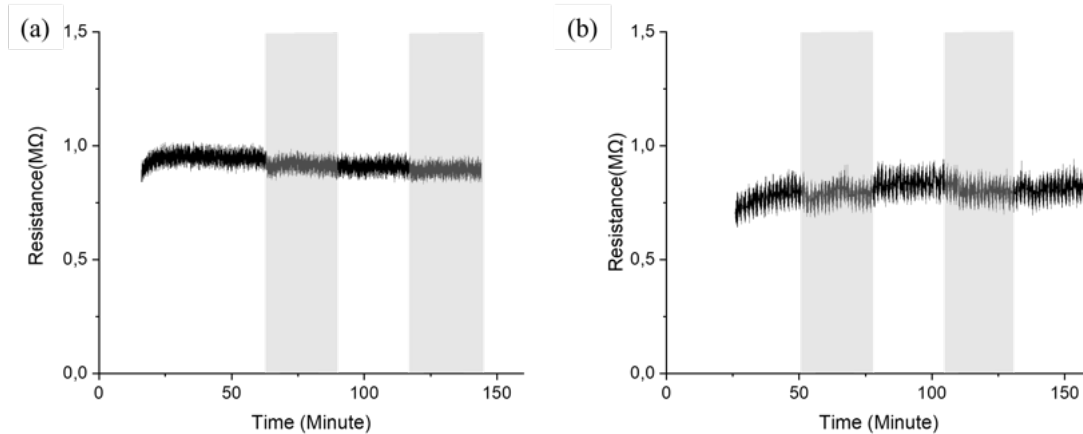


Figure 6.2: Response to CO₂ in synthetic air, (a) C600, Device No.5 (b) C450 Device No.2

To sum up, CO₂ detection in N₂ was observed at 200°C but was irreversible, with enhanced absorption seen with noble metal NPs decoration. In synthetic air, the response was minimal. Increasing the temperature to 250°C caused significant noise due to thermal issues, so subsequent measurements were conducted at 200°C. As indicated in Chapter 2.1.1, the CO₂ sensing mechanism of SnO₂ involves two steps: O₂ pre-adsorption and the reaction of CO₂ with pre-adsorbed oxygen ions. The insufficient sensing performance at 200°C may result from a limitation in one of these steps. To investigate this, the oxygen response of different devices was studied.

6.2. Response to O₂

Fig 6.3 shows the response of two chips, C600 and C450, at different concentrations of O₂, with each cycle lasting 60 minutes (30 minutes of N₂ followed by 30 minutes of N₂/O₂). The two materials exhibited completely different responses to oxygen. C600 exhibited classical n-type semiconductor behaviour, where oxygen adsorption depleted conduction electrons, leading to an increase in resistance. Details of this process can be found in Chapter 2. In contrast, C450 showed more complex behaviour. The resistance decreased when introducing O₂. However, when O₂ was introduced, the resistance of C450 did not immediately decrease. Instead, there was an initial sharp increase, followed by a gradual decrease.

The complex phenomenon of C450 suggests that SnO₂ has a transition from n-type to p-type when introducing oxygen. This change could be attributed to oxygen adsorption, which modifies the surface electron concentration distribution of SnO₂, resulting in a shift of the dominant

charge carriers from electrons (n-type) to holes (p-type). Detail of this assumption will be discussed in Section 6.4.

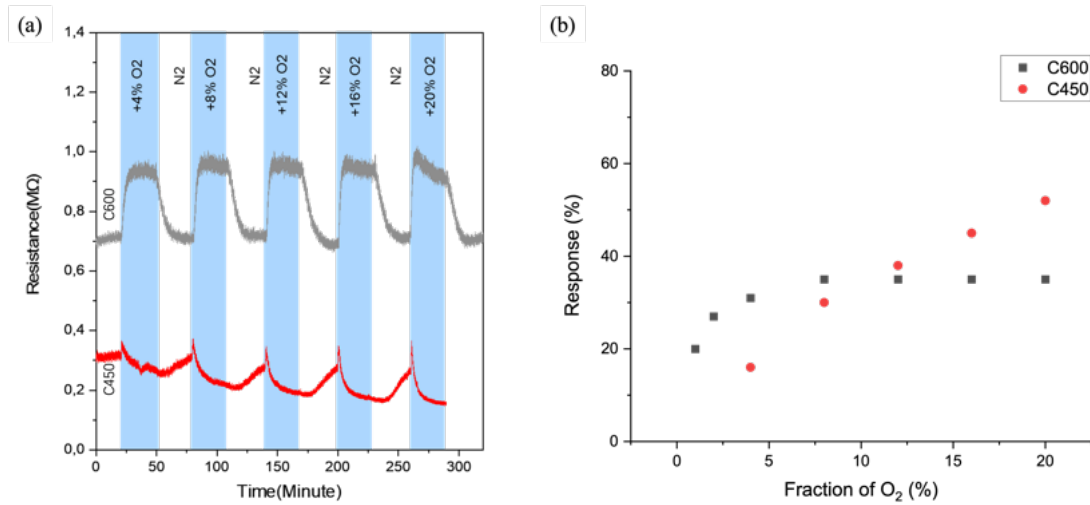


Figure 6.3: Response to O₂ with different annealing temperature (a) Resistance change, Device No.5 (b) Response of these samples, Device No.5

The influence of NPs on the sensing performance was also investigated. Fig.6.4a displays the resistance change of C600 and C600-Ag samples as oxygen concentrations varied. During the measurements, it was observed that the samples could not fully recover in 30 minutes. Therefore, the cycle time was extended to 2 hours, with 1 hour of N₂ and 1 hour of exposure to different oxygen concentrations. Fig. 6.4c quantifies the responses of all three samples to different oxygen concentrations related to 6.4b. Results show that samples annealed at 600°C have saturation at higher concentrations (>6%), with a maximum response of 40%. For those decorated with Ag NPs, the response significantly increases from 40% to 70%.

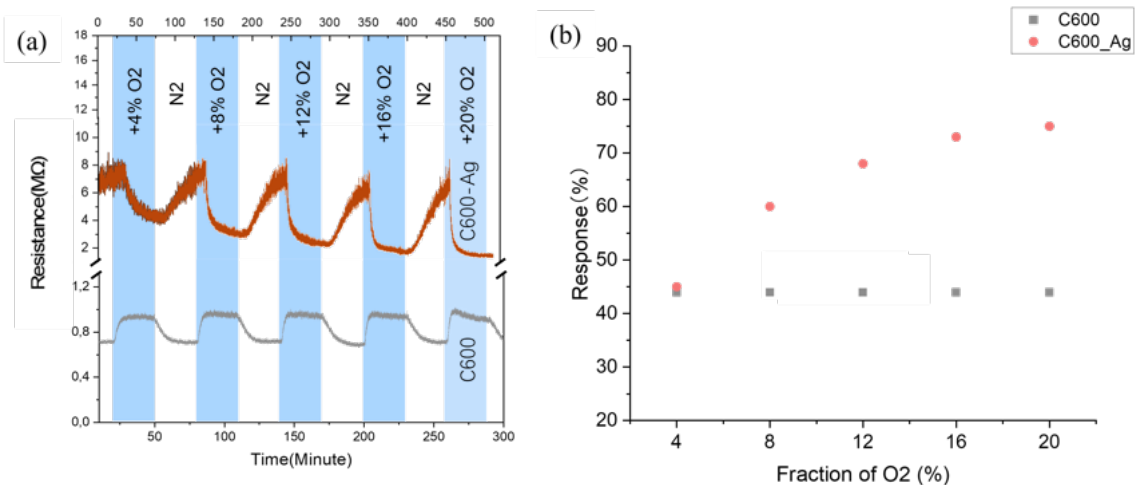


Figure 6.4: Response to O₂ with NPs (a) Resistance change of different samples, C600-Ag and C600 (b) Absolute Resistance change of these two samples

In Fig 6.5, the resistance behaviour of C600, C600-Ag, and C600-Ru samples under various oxygen concentrations is depicted. Unlike the measurements in Fig 6.4a, these measurements involved gradually increasing the oxygen fraction after stabilizing the samples in an N₂ atmosphere, without N₂ intervals between measurements. The results of this experiment are consistent with the previous one. Fig 6.5d shows that Ag and Ru exhibit similar results, indicating that their catalytic activities are comparable. C600 exhibited a typical n-type semiconductor response, while C600-Ag and C600-Ru showed the opposite trend. This opposite trend will also be discussed in Section 6.4.

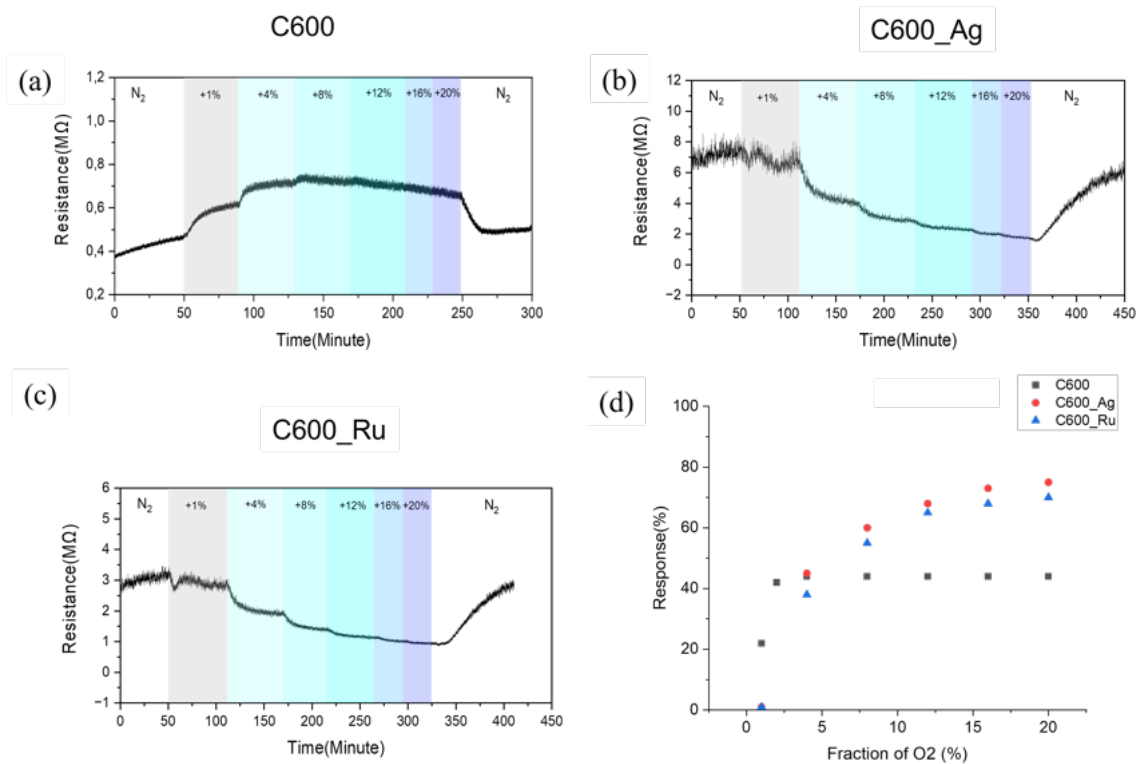


Figure 6.5: Response to O₂ with NPs (a) C600, Device No.5 (b) C600-Ag, Device No.5 (c) C600-Ru, Device No.5 (d) Absolute Resistance change of these two samples

In summary, this section investigates the response of C600, C600-Ag, C600-Ru, and C450 samples to oxygen. Only C600 exhibited typical n-type behaviour with increasing resistance to O₂, while all other samples showed an opposite trend. C450 displayed a complex response, with an initial resistance increase followed by a decrease. The specific mechanisms behind the responses of the other samples require further investigation. For C600, it was observed that at 200°C, the device can quickly reach dynamic equilibrium in air and maintain stability. This suggests that the insufficient sensing performance of C600 for CO₂ at this temperature is likely due to the inability to complete the second step—CO₂ reacting with pre-adsorbed oxygen ions—caused by the low working temperature.

6.3. Geometry Influence

This experiment aims to investigate the influence of the IDE configuration on gas sensing. In Fig 6.6, each cycle lasted 100 minutes, consisting of 50 minutes of exposure to 20% O₂ + 80% N₂, followed by 50 minutes of 5% CO₂ + 95% N₂. Although the gas composition alternated between two conditions, the testing did not maintain a single-variable control. However, this variation was consistent across all measurements, and the study focused on comparing the resistance response trends of devices with different configurations (electrode gap width and device area) under the same test conditions. Since the goal was to evaluate relative response patterns rather than isolate the effects of individual gas variables, the lack of a single-variable control does not compromise the validity of the analysis.

Fig 6.6 shows the resistance response of devices with different configurations under the testing conditions mentioned above. When exposed to CO₂ (gray regions), the resistance did not stabilize within 50 minutes. To get the response, the "Signal Process" averaging function in Origin was used to calculate the resistance values, identifying the minimum resistance point during CO₂ exposure. This minimum value was then compared to the resistance in the O₂ phase (before CO₂ introduction) to calculate the ratio $S = R/R_{CO_2}$. No clear trend can be concluded from Fig. 6.6, as the results show variability across different device configurations.

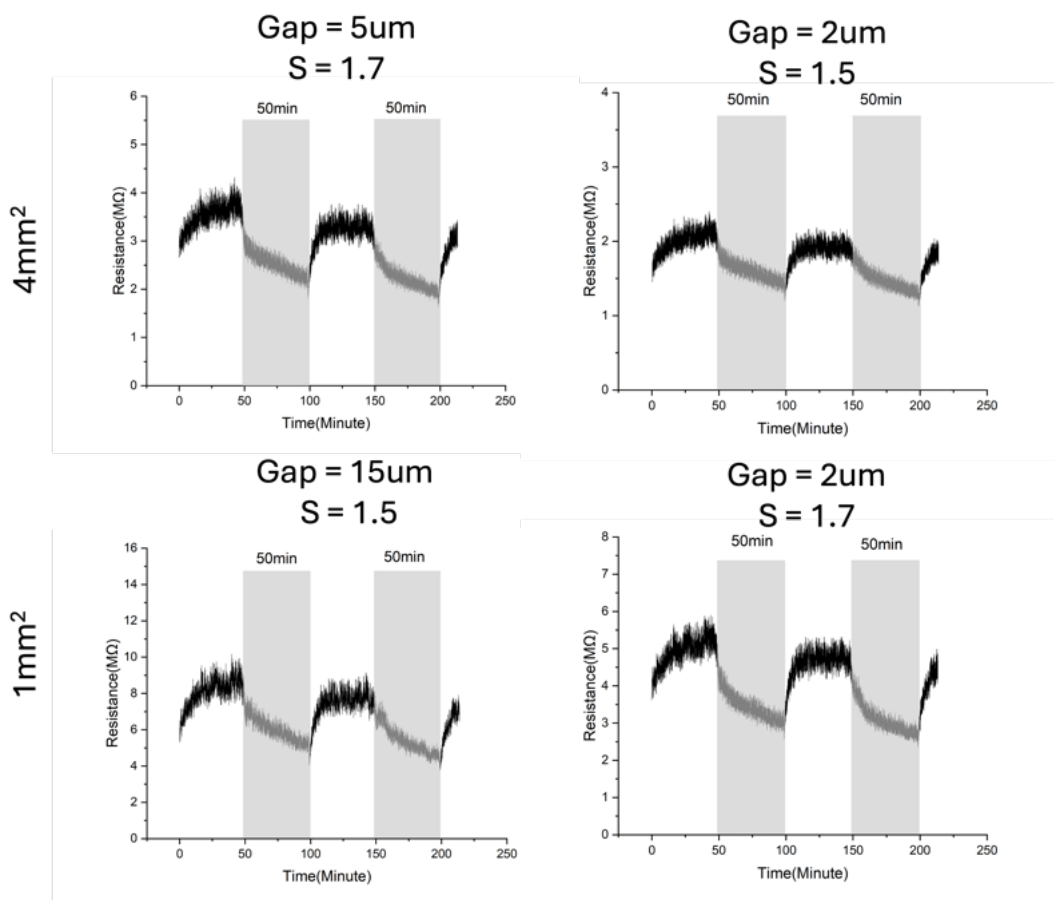


Figure 6.6: Resistance response of devices with different configurations under identical testing conditions.

To further explore the relation between the configuration and gas sensing performance, a more comprehensive dataset could be obtained by testing two groups of devices with areas of 4 mm² and 1 mm², each containing gap widths of 15 μm, 10 μm, 5 μm, and 2 μm. This approach would allow for a broader analysis of the parameters. Although the configuration differences are minor in this project, identifying an optimal structure could still enhance gas sensing performance.

6.4. Discussion

This chapter focuses on CO₂ gas sensing testing, which is divided into two main parts: testing in an N₂ environment and synthetic air. The results show that at 200°C, SnO₂ can detect the presence of CO₂ in N₂ without recovery, but in synthetic air, CO₂ has almost no response, which is expected to be reversed. The different phenomena observed under N₂ and N₂/O₂ backgrounds can be explained as follows: In an environment with only N₂, the introduction of CO₂ allows SnO₂ to directly react with CO₂, forming stable surface compounds or adsorption states. As a result, the sensor signal becomes difficult to recover. In contrast, in synthetic air containing O₂, the higher chemical reactivity of O₂ enables it to preferentially interact with the active sites on the SnO₂ surface, occupying these sites and forming adsorbed oxygen species (e.g., O⁻ or O₂⁻). This hinders the direct reaction between CO₂ and SnO₂. Moreover, the introduced CO₂ is more likely to react with these preadsorbed oxygen ions, and such reactions are typically reversible. Based on this explanation, there should theoretically be a response to CO₂ in synthetic air. However, no such response was observed in this project.

To investigate the cause of failure, the temperature was first increased to 250°C. However, this led to severe needle rotation, significantly increasing measurement noise and rendering the results unreliable. Previous literature emphasized the importance of high temperatures for O₂ adsorption, indicating that 200°C may be insufficient for the formation of the adsorbed oxygen ions. To confirm this, an oxygen gas sensing test was conducted, and results showed that the SnO₂ sensor successfully detected O₂. These findings suggest that the reaction between CO₂ and pre-adsorbed oxygen ions might be hindered, resulting in the failure to detect CO₂. However, an unusual phenomenon was observed during the oxygen sensing test: except for C600, all other samples exhibited an opposite trend in resistance changes upon exposure to O₂. Theoretically, resistance is expected to increase when oxygen is introduced, as explained in previous studies [71] [72].

Although reports on the anomalous phenomenon of SnO₂ nanoparticles are limited, this p-n transition is not an isolated case and has been observed in many other oxides. Table 6.1 lists some reports of anomalous gas sensing behaviours in the literature, which could provide insight into this case. A study by Zhao et al. observed a similar phenomenon, where n-type tungsten oxide nanowires exhibited an anomalous p-type response to NO₂ at room temperature [73]. They proposed that this transition was attributed to the formation of an inversion layer caused by oxygen adsorption, with holes replacing electrons as the primary charge carriers. Based on this study, a plausible assumption is that the conductivity type of C450 and the noble metal-decorated samples (C600-Ag and C600-Ru) annealed at 600°C was altered by exposure to oxygen. In the case of C450, the small particle size enhances the adsorption of oxygen molecules. For C600-Ag and C600-Ru, the noble metals act as catalysts, further

enhancing oxygen adsorption. With the hole concentration increasing, oxygen molecules adsorbed to the surface capture surface electrons, and to maintain charge neutrality, the internal positive charge increases, creating a larger positive charge conduction channel, which reduces the electrical resistance at the macroscopic level and produces a p-type response. The p-n transitions in Table 6.1 highlight that surface conductivity in semiconductor oxides depends on electrons and holes, with changes in majority carrier density potentially reversing the carrier type.

Table 6.1: The anomalous gas sensing behaviour reported in recent literature.

Sensing Material	Gas Type	Anomalous behavior	Mechanism	Ref
Fe@SnO ₂	O ₂	It acted as a p-type semiconductor at oxygen concentrations up to 10% at 300 °C but switched to n-type at 400 °C	As the working temperature increases, a greater number of electrons jump into the conduction band from the valence band.	[74]
α-Fe ₂ O ₃	O ₂	An n- to p-type transition	The oxygen adsorption and formation of a surface inversion layer lead to the inversion of the surface conduction type.	[75]
WO ₃	NO ₂	It exhibited p-type response to NO ₂ at room temperature	The formation of an inversion layer caused by oxygen adsorption leads to the p-type response.	[73]
SnO ₂	H ₂	The work function increases from 50°C to 150°C but decreases at 200°C and 250°C	The sensor's conductivity changes with carrier concentration, influenced by gas adsorption or desorption on the surface.	[76]

To further investigate the assumption, the type of the SnO₂ fabricated in this project needs to be determined. If the anomalous samples are proven to be p-type, this would support the assumption that conductivity type was altered by oxygen adsorption. A gate voltage was applied to the sensing layer to determine the type of the SnO₂ fabricated in this project, and the source and drain current (I_d , I_s) were measured. This method can determine the sensing material's conductivity type (n-type or p-type). However, nearly all the measured samples exhibited a hysteresis effect similar to that shown in Fig D.3b, making it hard to determine whether the material is n-type or p-type. Raman scattering analysis was conducted on C600, C600-Ag, and C600-Ru, see Fig D.4. No significant new peaks were observed in the modified samples of C600-Ag and C600-Ru, indicating that no notable secondary phases or vibration modes specific to composite materials were formed. Since this section is not the primary focus of the study, it is included in the Appendix D for further explanation.

6.5. Summary

C450, C600, C600-Ag, and C600-Ru, are used here for different gas sensing tests. CO₂ detection in N₂ was observed at 200°C but was irreversible. The response of C450 is slightly higher

than that of C600. C600-Ru exhibits a higher response, approximately twice that of the undecorated sample. In synthetic air, the response was nearly negligible for all samples. Increasing the temperature to 250°C caused significant noise, so all measurements were conducted at 200°C. To explore the reasons for failure. Oxygen adsorption was checked first. Results show that C600 has saturation at higher concentrations (>6%), with a maximum response of 40%. For those decorated with Ag NPs, the response significantly increases from 40% to 70%. Ag and Ru exhibit similar results, indicating that their catalytic activities are comparable. However, except for C600, the other three samples C450, C600-Ag and C600-Ru have a p-type response to O₂. The cause of this anomalous behaviour could be attributed to the formation of an electron depletion layer and a hole inversion layer due to O₂ adsorption, making holes the majority carriers. The high response to oxygen suggests that the low operating temperature may prevent the completion of the second step - the reaction of CO₂ with pre-adsorbed oxygen ions. Therefore, it is important to raise the working temperature. For the geometry influence, there is no clear correlation between the device area, gap width, and sensing performance.

7

Conclusion and Recommendations

Many metal oxide-based gas sensors were reported for CO₂ detection. To name a few, SnO₂, ZnO and CuO. Nowadays, nanostructured materials have gained a lot of interest in this field. Characterized by a high surface area-to-volume ratio, these metal oxides at nanoscale offer an abundance of surface-active sites, leading to heightened surface reactivity, therefore enhancing the sensitivity and effectiveness of CO₂ detection. This study explores the application of SnO₂ nanoparticles synthesized via spark ablation, focusing on their potential use in CO₂ sensors. Spherical SnO₂ nanoparticles were successfully synthesized and used to create a 2.5 μm thick SnO₂ sensing layer on a specially designed interdigitated electrode (IDE) structure. The IDE configurations featured a fixed finger width of 5 μm, with gap widths ranging from 2 to 15 μm, and sensing areas of 1×1 cm and 1×4 cm. This aims to explore the relationship between the IDE configuration and gas sensing performance.

The effect of annealing treatment and noble metal decoration on the sensing material is the focus of this study. The grain size of the SnO₂ sensing layer was effectively tuned by controlling the annealing temperature, increasing from approximately 7 nm at 450°C to 12 nm at 600°C. SEM results indicate that the diameter of the particles annealed at 600°C is around 12 nm. The particles annealed at 450 °C are smaller, though their boundaries are not clear enough to determine the precise value. Noble metal Ru and Ag nanoparticles were employed as surface decorations to enhance the sensitivity and selectivity of the SnO₂ sensing layer, with surface densities of 19% for Ru and 12% for Ag.

Gas tests showed that at 200°C, SnO₂ can detect CO₂ in an N₂ environment but without recovery, suggesting the formation of stable surface compounds or adsorption states. However, in N₂/O₂ atmosphere, SnO₂ exhibited almost no response to CO₂, possibly due to insufficient temperature. Most gas sensors show significantly higher responses above 200°C, while room-temperature sensors often require material modifications, unlike the pure SnO₂ NPs used here. Increasing the operating temperature to 250°C did not yield reliable results due to severe needle rotation and high measurement noise. Oxygen sensing tests confirmed the presence of adsorbed oxygen species on the SnO₂ surface at 200°C, supporting the hypothesis that the reaction between CO₂ and preadsorbed oxygen ions may require a higher activation energy, which can only be achieved at elevated temperatures in this case.

Due to the failure of CO₂ sensing in N₂/O₂, the effects of the annealing temperature and noble metal decoration were investigated through O₂ sensing performance. Sample annealed at 600°C showed saturation at higher concentrations (>6%), with a maximum response of 40%, while at 450°C, it has stronger sensitivity and sustained responses, with a maximum of 60%. This suggests that excessively high annealing temperatures may reduce oxygen vacancy concentrations[69]. Experiments also show that the decoration of Ag and Ru NPs can significantly enhance the response with comparable effects, increasing it from 40% to 70%. However, it also extends both the response and recovery times, approximately doubling them compared to the undecorated samples. Note that except for C600, C450, C600-Ag, and C600-Ru showed an anomalous resistance decrease upon O₂ exposure, contrary to the expected increase reported in previous studies. This could be attributed to the adsorption of a large amount of oxygen, which helps to form the electron depletion layer and a hole inversion layer, making holes the main carriers. Additionally, the configuration of IDE has little effect on the sensing performance, which may be attributed to the small finger width of 5 μm. At this scale, the electric field generated across the IDE structure is sufficiently strong and uniform.

This work proves that spark ablation can efficiently synthesize metal nanoparticles. To further improve the CO₂ sensing performance, it is important to increase the working temperature to at least 250°C. A temperature gradient can also be set to identify the turning point at which the CO₂ sensing response increases rapidly. For example, the test can be conducted from 200°C to 400°C with intervals of 50°C. The anomalous sensing behaviour of SnO₂ in response to O₂ is worth further investigation. Recent literature suggests that extensive O₂ adsorption helps to form the inversion layer, making holes the dominant charge carriers. In this project, the adsorption of O₂ is highly dependent on the working temperature. To accurately assess the p-n type of the sample, it is necessary to conduct measurements at the operating temperature, as prior measurements were carried out at room temperature. Additionally, X-ray Photoelectron Spectroscopy (XPS) can also be employed to analyze surface chemical states and identify the adsorbed species, providing deeper insights into the mechanism behind this behaviour.

References

- [1] Kaichun Xu et al. “Suspension Plasma Sprayed ZnO Coatings for CO₂ Gas Detection”. In: *Journal of Thermal Spray Technology* 32.1 (Oct. 2022), pp. 72–81. DOI: 10.1007/s11666-022-01479-w. URL: <https://doi.org/10.1007/s11666-022-01479-w>.
- [2] Suresh Neethirajan, Digvir S. Jayas, and S. Sadistap. “Carbon Dioxide (CO₂) Sensors for the Agri-food Industry—A Review”. In: *Food and Bioprocess Technology* 2.2 (Nov. 2008), pp. 115–121. DOI: 10.1007/s11947-008-0154-y. URL: <https://doi.org/10.1007/s11947-008-0154-y>.
- [3] Xiangpeng Meng et al. “Carbon dioxide and oxygen gas sensors-possible application for monitoring quality, freshness, and safety of agricultural and food products with emphasis on importance of analytical signals and their transformation”. In: 57.6 (Nov. 2014), pp. 723–733. DOI: 10.1007/s13765-014-4180-3. URL: <https://doi.org/10.1007/s13765-014-4180-3>.
- [4] Xin Gao and Yun Wu Li. “Monitoring Gases Content in Modern Agriculture: A Density Functional Theory Study of the Adsorption Behavior and Sensing Properties of CO₂ on MoS₂ Doped GeSe Monolayer”. In: *Sensors* 22.10 (May 2022), p. 3860. DOI: 10.3390/s22103860. URL: <https://doi.org/10.3390/s22103860>.
- [5] Ananya Dey. “Semiconductor metal oxide gas sensors: A review”. In: *Materials Science and Engineering B* 229 (Jan. 2018), pp. 206–217. DOI: 10.1016/j.mseb.2017.12.036. URL: <https://doi.org/10.1016/j.mseb.2017.12.036>.
- [6] Hyo Joong Kim and Jong Heun Lee. “Highly sensitive and selective gas sensors using p-type oxide semiconductors: Overview”. In: *Sensors and actuators. B, Chemical* 192 (Mar. 2014), pp. 607–627. DOI: 10.1016/j.snb.2013.11.005. URL: <https://www.sciencedirect.com/science/article/pii/S0925400513013476>.
- [7] M.E. Beydilli. *Spark ablated metal oxide nanoparticles for gas sensing*. 2022. URL: <https://repository.tudelft.nl/record/uuid:c127d45e-739a-4a35-8f50-8b2df0da70e9>.
- [8] Li-Yuan Zhu et al. “Advances in Noble Metal-Decorated Metal Oxide Nanomaterials for Chemiresistive Gas Sensors: Overview”. In: *Nano-Micro Letters* 15.1 (Apr. 2023). DOI: 10.1007/s40820-023-01047-z. URL: <https://doi.org/10.1007/s40820-023-01047-z>.
- [9] Kwang-Su Kim et al. “Catalytic Pd–TiO₂ thin film based fire detector to operate at room temperature”. In: *Microelectronic Engineering* 86.4-6 (Apr. 2009), pp. 1297–1299. DOI: 10.1016/j.mee.2009.02.014. URL: <https://doi.org/10.1016/j.mee.2009.02.014>.

- [10] J. Herrán, G.G. Mandayo, and E. Castaño. “Physical behaviour of BaTiO₃–CuO thin-film under carbon dioxide atmospheres”. In: *Sensors and Actuators B: Chemical* 127.2 (Nov. 2007), pp. 370–375. DOI: 10.1016/j.snb.2007.04.035. URL: <https://doi.org/10.1016/j.snb.2007.04.035>.
- [11] S Shukla et al. “Significance of electrode-spacing in hydrogen detection for tin oxide-based MEMS sensor”. In: *International Journal of Hydrogen Energy* 33.1 (Oct. 2007), pp. 470–475. DOI: 10.1016/j.ijhydene.2007.07.043. URL: <https://doi.org/10.1016/j.ijhydene.2007.07.043>.
- [12] Norman G. Moll, Dale R. Clutter, and Warren E. Thompson. “Carbon trioxide: its production, infrared spectrum, and structure studied in a matrix of solid CO₂”. In: *The Journal of Chemical Physics* 45.12 (Dec. 1966), pp. 4469–4481. DOI: 10.1063/1.1727526. URL: <https://doi.org/10.1063/1.1727526>.
- [13] Ahalapitiya Jayatissa and Tarun Gupta. “Metal-Oxide-Semiconductor (MOS) Gas Sensors Advances in sensors, Chemical Sensor and Biosensor, (ISBN: 978-84-09-03030)”. In: Sept. 2018.
- [14] David G. Rickerby and Alessandra M. Serventi. *Nanostructured Metal Oxide Gas Sensors for Air-Quality Monitoring*. Jan. 2010, pp. 99–136. DOI: 10.1016/b978-0-08-054820-3.00006-x. URL: <https://doi.org/10.1016/b978-0-08-054820-3.00006-x>.
- [15] Yingbin Lin and Zhuangjun Fan. “Compositing strategies to enhance the performance of chemiresistive CO₂ gas sensors”. In: *Materials Science in Semiconductor Processing* 107 (Mar. 2020), p. 104820. DOI: 10.1016/j.mssp.2019.104820. URL: <https://doi.org/10.1016/j.mssp.2019.104820>.
- [16] Antonio Tricoli, Marco Righettoni, and Alexandra Teleki. “Semiconductor Gas Sensors: dry synthesis and Application”. In: *Angewandte Chemie International Edition* 49.42 (Aug. 2010), pp. 7632–7659. DOI: 10.1002/anie.200903801. URL: <https://doi.org/10.1002/anie.200903801>.
- [17] Nicolae Bârsan, Michael Hübner, and Udo Weimar. “Conduction mechanisms in SnO₂ based polycrystalline thick film gas sensors exposed to CO and H₂ in different oxygen backgrounds”. In: *Sensors and Actuators B: Chemical* 157.2 (Oct. 2011), pp. 510–517. DOI: 10.1016/j.snb.2011.05.011. URL: <https://doi.org/10.1016/j.snb.2011.05.011>.
- [18] Michael Hübner et al. “Influence of humidity on CO sensing with p-type CuO thick film gas sensors”. In: *Sensors and Actuators B: Chemical* 153.2 (Apr. 2011), pp. 347–353. DOI: 10.1016/j.snb.2010.10.046. URL: <https://doi.org/10.1016/j.snb.2010.10.046>.
- [19] A. Oprea et al. *Basics of semiconducting Metal oxide-based gas sensors*. Jan. 2019, pp. 61–165. DOI: 10.1016/b978-0-12-811224-3.00003-2. URL: <https://doi.org/10.1016/b978-0-12-811224-3.00003-2>.
- [20] Vivekanand Mishra, Rashmi Rashmi, and Sukriti. *Optical gas sensors*. Feb. 2023. DOI: 10.5772/intechopen.108971. URL: <https://doi.org/10.5772/intechopen.108971>.

- [21] H R Shwetha et al. “MEMS based metal oxide semiconductor carbon dioxide gas sensor”. In: *Micro and Nano Engineering* 16 (Aug. 2022), p. 100156. DOI: 10.1016/j.mne.2022.100156. URL: <https://doi.org/10.1016/j.mne.2022.100156>.
- [22] Javier Burgués, Juan Manuel Jiménez-Soto, and Santiago Marco. “Estimation of the limit of detection in semiconductor gas sensors through linearized calibration models”. In: *Analytica Chimica Acta* 1013 (Feb. 2018), pp. 13–25. DOI: 10.1016/j.aca.2018.01.062. URL: <https://doi.org/10.1016/j.aca.2018.01.062>.
- [23] Diana Mardare et al. “Low temperature TiO₂ based gas sensors for CO₂”. In: *Ceramics International* 42.6 (May 2016), pp. 7353–7359. DOI: 10.1016/j.ceramint.2016.01.137. URL: <https://doi.org/10.1016/j.ceramint.2016.01.137>.
- [24] Diana Mardare et al. “The effect of CO₂ gas adsorption on the electrical properties of Fe doped TiO₂ films”. In: *Physica B: Condensed Matter* 524 (Nov. 2017), pp. 17–21. DOI: 10.1016/j.physb.2017.08.029. URL: <https://doi.org/10.1016/j.physb.2017.08.029>.
- [25] Gaoqiang Niu and Fei Wang. “A review of MEMS-based metal oxide semiconductors gas sensor in Mainland China”. In: *Journal of Micromechanics and Microengineering* 32.5 (Mar. 2022), p. 054003. DOI: 10.1088/1361-6439/ac5b98. URL: <https://doi.org/10.1088/1361-6439/ac5b98>.
- [26] *Operating principle □MOS-type gas sensor*. URL: <https://www.figarosensor.com/technicalinfo/principle/mos-type.html>.
- [27] M. Aslam, Chris Gregory, and J.V. Hatfield. “Polyimide membrane for micro-heated gas sensor array”. In: *Sensors and Actuators B: Chemical* 103.1-2 (Sept. 2004), pp. 153–157. DOI: 10.1016/j.snb.2004.04.102. URL: <https://www.sciencedirect.com/science/article/pii/S0925400504002278?via%3Dihub>.
- [28] Fatemeh Bagheri and H. Haratizadeh. “UV-activated CO₂ sensor based on ZnO nanoparticles at low temperatures”. In: *Materials Science in Semiconductor Processing* 141 (Apr. 2022), p. 106422. DOI: 10.1016/j.mssp.2021.106422. URL: <https://www.sciencedirect.com/science/article/pii/S1369800121007538?via%3Dihub>.
- [29] Shravanti Joshi et al. “Modulating interleaved ZnO assembly with CuO nanoleaves for multifunctional performance: perdurable CO₂ gas sensor and visible light catalyst”. In: *Inorganic chemistry frontiers* 4.11 (Jan. 2017), pp. 1848–1861. DOI: 10.1039/c7qi00474e. URL: <https://doi.org/10.1039/c7qi00474e>.
- [30] Tetsuro Seiyama and Shuichi Kagawa. “Study on a detector for gaseous components using semiconductive thin films.” In: *Analytical Chemistry* 38.8 (July 1966), pp. 1069–1073. DOI: 10.1021/ac60240a031. URL: <https://doi.org/10.1021/ac60240a031>.
- [31] Honggen Peng et al. “SNO₂ nano-sheet as an efficient catalyst for CO oxidation”. In: *Chinese Journal of Catalysis* 36.11 (Nov. 2015), pp. 2004–2010. DOI: 10.1016/s1872-2067(15)60926-3. URL: [https://doi.org/10.1016/s1872-2067\(15\)60926-3](https://doi.org/10.1016/s1872-2067(15)60926-3).
- [32] Tetsuro Seiyama et al. “A New Detector for Gaseous Components Using Semiconductive Thin Films.” In: *Analytical Chemistry* 34.11 (Oct. 1962), pp. 1502–1503. DOI: 10.1021/ac60191a001. URL: <https://doi.org/10.1021/ac60191a001>.

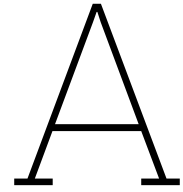
- [33] Dandan Wang et al. “CO₂-sensing properties and mechanism of nano-SnO₂ thick-film sensor”. In: *Sensors and Actuators B: Chemical* 227 (May 2016), pp. 73–84. DOI: 10.1016/j.snb.2015.12.025. URL: <https://doi.org/10.1016/j.snb.2015.12.025>.
- [34] *Scopus Preview - Scopus - Welcome to Scopus*. URL: <https://www.scopus.com/record/display.uri?eid=2-s2.0-34247599382&origin=inward&txGid=ec803b20ea599724326b775a5871e9f2>.
- [35] Padmanathan Karthick Kannan, R. Saraswathi, and John Bosco Balaguru Rayappan. “CO₂ gas sensing properties of DC reactive magnetron sputtered ZnO thin film”. In: *Ceramics International* 40.8 (Sept. 2014), pp. 13115–13122. DOI: 10.1016/j.ceramint.2014.05.011. URL: <https://doi.org/10.1016/j.ceramint.2014.05.011>.
- [36] Yong Xia et al. “In-situ synthesized N-doped ZnO for enhanced CO₂ sensing: Experiments and DFT calculations”. In: *Sensors and Actuators B: Chemical* 357 (Apr. 2022), p. 131359. DOI: 10.1016/j.snb.2022.131359. URL: <https://doi.org/10.1016/j.snb.2022.131359>.
- [37] Fatemeh Bagheri, H. Haratizadeh, and Mohammad H. Ahmadi. “Improving CO₂ sensing and P-N conductivity transition under UV light by chemo-resistive sensor based on ZNO nanoparticles”. In: *Ceramics International* 50.1 (Jan. 2024), pp. 1497–1504. DOI: 10.1016/j.ceramint.2023.10.240. URL: <https://doi.org/10.1016/j.ceramint.2023.10.240>.
- [38] Ajay Kumar Yadav et al. “Highly sensitive CO₂ sensor based on microrods-like La₂O₃ thin film electrode”. In: *RSC Advances* 6.108 (Jan. 2016), pp. 106074–106080. DOI: 10.1039/c6ra22118a. URL: <https://doi.org/10.1039/c6ra22118a>.
- [39] Ganhua Lu et al. “Gas Sensors Based on Tin Oxide Nanoparticles Synthesized from a Mini-Arc Plasma Source”. In: *Journal of Nanomaterials* 2006 (Jan. 2006), pp. 1–7. DOI: 10.1155/jnm/2006/60828. URL: <https://doi.org/10.1155/jnm/2006/60828>.
- [40] A. A. Ефимов et al. “Tin Oxide Nanoparticles Produced by Spark Ablation: Synthesis and Gas Sensing Properties”. In: *Oriental journal of chemistry* 32.6 (Dec. 2016), pp. 2909–2913. DOI: 10.13005/ojc/320609. URL: <https://doi.org/10.13005/ojc/320609>.
- [41] Jincheng Lei et al. “One-Step Fabrication of Nanocrystalline Nanonetwork SnO₂ Gas Sensors by Integrated Multilaser Processing”. In: *Advanced Materials Technologies* 5.8 (June 2020). DOI: 10.1002/admt.202000281. URL: <https://doi.org/10.1002/admt.202000281>.
- [42] G.D. Khuspe et al. “Nanostructured SnO₂ thin films for NO₂ gas sensing applications”. In: *Ceramics International* 39.8 (Dec. 2013), pp. 8673–8679. DOI: 10.1016/j.ceramint.2013.04.047. URL: <https://doi.org/10.1016/j.ceramint.2013.04.047>.
- [43] Rolando T. Candidato et al. “Effects of precursor composition used in solution precursor plasma spray on the properties of ZnO coatings for CO₂ and UV light sensing”. In: *Surface & Coatings Technology* 371 (Aug. 2019), pp. 395–400. DOI: 10.1016/j.surfcoat.2018.10.009. URL: <https://doi.org/10.1016/j.surfcoat.2018.10.009>.

- [44] V. Ambardekar, P.P. Bandyopadhyay, and S.B. Majumder. “Plasma sprayed copper oxide sensor for selective sensing of carbon monoxide”. In: *Materials Chemistry and Physics* 258 (Jan. 2021), p. 123966. DOI: 10.1016/j.matchemphys.2020.123966. URL: <https://doi.org/10.1016/j.matchemphys.2020.123966>.
- [45] N.B. Tanvir et al. “Investigation of CO₂ reaction with copper oxide nanoparticles for room temperature gas sensing”. In: *Journal of materials chemistry. A, Materials for energy and sustainability* 4.14 (Jan. 2016), pp. 5294–5302. DOI: 10.1039/c5ta09089j. URL: <https://doi.org/10.1039/c5ta09089j>.
- [46] Ahmed A. Aboud et al. “CO₂ responses based on pure and doped CeO₂ nano-pellets”. In: *Journal of Materials Research and Technology* 7.1 (Jan. 2018), pp. 14–20. DOI: 10.1016/j.jmrt.2017.03.003. URL: <https://doi.org/10.1016/j.jmrt.2017.03.003>.
- [47] Nishchay A. Isaac et al. “Characterization of Tungsten Oxide Thin Films Produced by Spark Ablation for NO₂ Gas Sensing”. In: *ACS Applied Materials & Interfaces* 8.6 (Feb. 2016), pp. 3933–3939. DOI: 10.1021/acsami.5b11078. URL: <https://doi.org/10.1021/acsami.5b11078>.
- [48] Rajendra G. Desai et al. “Indium sesquiterelluride (In₂Te₃) thin film gas sensor for detection of carbon dioxide”. In: *Sensors and Actuators B: Chemical* 107.2 (June 2005), pp. 523–527. DOI: 10.1016/j.snb.2004.11.011. URL: <https://doi.org/10.1016/j.snb.2004.11.011>.
- [49] Takashi Sugai and T. Matsuzawa. “Rare earth metal-oxide-based CO₂ gas sensor”. In: *Sensors and Actuators B: Chemical* 13.1-3 (May 1993), pp. 480–482. DOI: 10.1016/0925-4005(93)85432-a. URL: [https://doi.org/10.1016/0925-4005\(93\)85432-a](https://doi.org/10.1016/0925-4005(93)85432-a).
- [50] M.Y. Kim et al. “Carbon dioxide sensitivity of La-doped thick film tin oxide gas sensor”. In: *Ceramics International* 38 (Jan. 2012), S657–S660. DOI: 10.1016/j.ceramint.2011.05.129. URL: <https://doi.org/10.1016/j.ceramint.2011.05.129>.
- [51] Ya Xiong et al. “Tin oxide thick film by doping rare earth for detecting traces of CO₂: Operating in oxygen-free atmosphere”. In: *Materials Research Bulletin* 52 (Apr. 2014), pp. 56–64. DOI: 10.1016/j.materresbull.2013.12.057. URL: <https://doi.org/10.1016/j.materresbull.2013.12.057>.
- [52] J. Herrán, G.G. Mandayo, and E. Castaño. “Semiconducting BaTiO₃-CuO mixed oxide thin films for CO₂ detection”. In: *Thin Solid Films* 517.22 (Sept. 2009), pp. 6192–6197. DOI: 10.1016/j.tsf.2009.04.007. URL: <https://doi.org/10.1016/j.tsf.2009.04.007>.
- [53] Shrivanti Joshi et al. “Efficient Heterostructures of Ag@CuO/BaTiO₃ for Low-Temperature CO₂ Gas Detection: Assessing the Role of Nanointerfaces during Sensing by Operando DRIFTS Technique”. In: *ACS Applied Materials & Interfaces* 9.32 (Aug. 2017), pp. 27014–27026. DOI: 10.1021/acsami.7b07051. URL: <https://doi.org/10.1021/acsami.7b07051>.
- [54] Ya Xiong et al. “Effective CO₂ detection based on LaOCl-doped SnO₂ nanofibers: Insight into the role of oxygen in carrier gas”. In: *Sensors and Actuators B: Chemical* 241 (Mar. 2017), pp. 725–734. DOI: 10.1016/j.snb.2016.10.143. URL: <https://doi.org/10.1016/j.snb.2016.10.143>.

- [55] Audrey Chappelle et al. “Improved semiconducting CuO/CuFe₂O₄ nanostructured thin films for CO₂ gas sensing”. In: *Sensors and Actuators B: Chemical* 204 (Dec. 2014), pp. 407–413. DOI: 10.1016/j.snb.2014.07.088. URL: <https://doi.org/10.1016/j.snb.2014.07.088>.
- [56] Irmak Karaduman et al. “CO₂ gas detection properties of a TiO₂/Al₂O₃ heterostructure under UV light irradiation”. In: *Physica Scripta* 90.5 (Apr. 2015), p. 055802. DOI: 10.1088/0031-8949/90/5/055802. URL: <https://doi.org/10.1088/0031-8949/90/5/055802>.
- [57] Mohini Panday, Gaurav Upadhyay, and L.P. Purohit. “Sb incorporated SnO₂ nanostructured thin films for CO₂ gas sensing and humidity sensing applications”. In: *Journal of Alloys and Compounds* 904 (May 2022), p. 164053. DOI: 10.1016/j.jallcom.2022.164053. URL: <https://www.sciencedirect.com/science/article/pii/S0925838822004443>.
- [58] V. Manikandan et al. “A reliable chemiresistive sensor of nickel-doped tin oxide (Ni-SnO₂) for sensing carbon dioxide gas and humidity”. In: *RSC Advances* 10.7 (Jan. 2020), pp. 3796–3804. DOI: 10.1039/c9ra09579a. URL: <https://pubs.rsc.org/en/content/articlelanding/2020/ra/c9ra09579a>.
- [59] Guannan Yang et al. “Towards an improved understanding of the evolution of the size distribution of ultrafine nanoparticles produced by a rapidly quenched vapor source”. In: *Metallurgical and Materials Transactions A* 55.5 (Mar. 2024), pp. 1509–1515. DOI: 10.1007/s11661-024-07340-9. URL: <https://doi.org/10.1007/s11661-024-07340-9>.
- [60] T.V. Pfeiffer, J. Feng, and A. Schmidt-Ott. “New developments in spark production of nanoparticles”. In: *Advanced Powder Technology* 25.1 (Dec. 2013), pp. 56–70. DOI: 10.1016/j.apt.2013.12.005. URL: <https://doi.org/10.1016/j.apt.2013.12.005>.
- [61] *nanoparticle generator, VSP-G1 Nanoparticle Generator*. URL: <https://vsparticle.com/products/vsp-g1-nanoparticle-generator>.
- [62] R.E. Smallman and A.H.W. Ngan. *Characterization and analysis*. Sept. 2013, pp. 159–250. DOI: 10.1016/b978-0-08-098204-5.00005-5. URL: <https://doi.org/10.1016/b978-0-08-098204-5.00005-5>.
- [63] S.J. Rice. *Graphene with Platinum Nanoparticles for Neural Recording and Stimulation*. 2023. URL: <https://repository.tudelft.nl/record/uuid:d2ed52e8-21e2-495f-89f7-d85901d9dfd4>.
- [64] Ta Yang Goh et al. “Performance analysis of image thresholding: Otsu technique”. In: *Measurement* 114 (Sept. 2017), pp. 298–307. DOI: 10.1016/j.measurement.2017.09.052. URL: <https://doi.org/10.1016/j.measurement.2017.09.052>.
- [65] Golnoush Zamiri and F. E. Ghodsi. “The impact of annealing treatment on ethanol gas sensing performance of SnO₂ nanoflakes”. In: *ECS Journal of Solid State Science and Technology* 12.8 (July 2023), p. 087001. DOI: 10.1149/2162-8777/aceaab. URL: <https://doi.org/10.1149/2162-8777/aceaab>.
- [66] Donald A. Neamen. *Semiconductor Physics and Devices*. Irwin Professional Publishing, Jan. 1992.

- [67] P. A. Chernavskii Jr. et al. "Oxidation of metal nanoparticles: Experiment and model". In: *Russian Journal of Physical Chemistry B* 1.4 (2007), pp. 394–411. DOI: 10.1134/S1990793107040082.
- [68] Da Song et al. "Migration mechanism of lattice oxygen: Conversion of CO₂ to CO using NiFe₂O₄ spinel oxygen carrier in chemical looping reactions". In: *Catalysts* 12.10 (Oct. 2022), p. 1181. DOI: 10.3390/catal12101181. URL: <https://doi.org/10.3390/catal12101181>.
- [69] C. Ke et al. "Annealing temperature dependent oxygen vacancy behavior in SnO₂ thin films fabricated by pulsed laser deposition". In: *Current Applied Physics* 11.3 (Dec. 2010), S306–S309. DOI: 10.1016/j.cap.2010.11.067. URL: <https://doi.org/10.1016/j.cap.2010.11.067>.
- [70] Deepa S et al. "Deposition temperature as a crucial process parameter in tuning the CO₂ sensing properties of Spary-Pyrolyzed SnO₂ thin film". In: *ECS Journal of Solid State Science and Technology* 12.11 (Nov. 2023), p. 117005. DOI: 10.1149/2162-8777/ad0ab0. URL: <https://doi.org/10.1149/2162-8777/ad0ab0>.
- [71] A. Oprea et al. "Conduction model of SnO₂ thin films based on conductance and Hall effect measurements". In: *Journal of Applied Physics* 100.3 (Aug. 2006). DOI: 10.1063/1.2229802. URL: <https://doi.org/10.1063/1.2229802>.
- [72] Ireneusz Kocemba and Jacek M. Rynkowski. "The effect of oxygen adsorption on catalytic activity of SnO₂ in CO oxidation". In: *Catalysis Today* 169.1 (Oct. 2010), pp. 192–199. DOI: 10.1016/j.cattod.2010.09.015. URL: <https://doi.org/10.1016/j.cattod.2010.09.015>.
- [73] None Zhao Bo-Shuo et al. "Tungsten oxide nanowire gas sensor preparation and P-type NO₂ sensing properties at room temperature". In: *Acta Physica Sinica* 67.5 (Jan. 2018), p. 058101. DOI: 10.7498/aps.67.20172236. URL: <https://doi.org/10.7498/aps.67.20172236>.
- [74] K. Galatsis et al. "p- and n-type Fe-doped SnO₂ gas sensors fabricated by the mechanochemical processing technique". In: *Sensors and Actuators B Chemical* 93.1-3 (Apr. 2003), pp. 562–565. DOI: 10.1016/S0925-4005(03)00233-8. URL: [https://doi.org/10.1016/S0925-4005\(03\)00233-8](https://doi.org/10.1016/S0925-4005(03)00233-8).
- [75] A. Gurlo et al. "An n- to p-type conductivity transition induced by oxygen adsorption on α -Fe₂O₃". In: *Applied Physics Letters* 85.12 (Sept. 2004), pp. 2280–2282. DOI: 10.1063/1.1794853. URL: <https://doi.org/10.1063/1.1794853>.
- [76] Byeongdeok Yea et al. "Analysis of the sensing mechanism of tin dioxide thin film gas sensors using the change of work function in flammable gas atmosphere". In: *Applied Surface Science* 100-101 (July 1996), pp. 365–369. DOI: 10.1016/0169-4332(96)00243-7. URL: [https://doi.org/10.1016/0169-4332\(96\)00243-7](https://doi.org/10.1016/0169-4332(96)00243-7).
- [77] S. Jayapandi et al. "Reinforced photocatalytic reduction of SnO₂ nanoparticle by La incorporation for efficient photodegradation under visible light irradiation". In: *Journal of Materials Science Materials in Electronics* 30.9 (Mar. 2019), pp. 8479–8492. DOI: 10.1007/s10854-019-01168-5. URL: <https://doi.org/10.1007/s10854-019-01168-5>.

- [78] S.H Sun et al. "Raman scattering study of rutile SnO₂ nanobelts synthesized by thermal evaporation of Sn powders". In: *Chemical Physics Letters* 376.1-2 (July 2003), pp. 103–107. DOI: 10.1016/s0009-2614(03)00965-5. URL: [https://doi.org/10.1016/s0009-2614\(03\)00965-5](https://doi.org/10.1016/s0009-2614(03)00965-5).



Flow Chart

A.1. Part 1: Cleaning Step

A.1.1. CLEANING PROCEDURE: HNO₃ 100% and 65%

Cleaning:

- 10 minutes in fuming nitric acid (Merck: HNO₃ 100%) at ambient temperature.
- Use wet bench "HNO₃ (100%)" and the carrier with the red dot.

QDR:

- Rinse in the Quick Dump Rinser with the standard program until the resistivity is 5 MΩ.

Cleaning:

- 10 minutes in concentrated nitric acid (Merck: HNO₃ 65%) at 110 °C.
- Use wet bench "HNO₃ (65%)" and the carrier with the red dot.

QDR:

- Rinse in the Quick Dump Rinser with the standard program until the resistivity is 5 MΩ.

Drying:

- Use the Semitool "rinsed/dryer" with the standard program, and the white carrier with a red dot.

A.2. Part 2: OXIDATION

A.2.1. OXIDATION

Furnace no: C1 or D1

Table A.1: Program name: WET1000

PROCESS	TEMPERATURE (in °C)	GASSES & FLOWS (in l/min)	TIME (in min- utes)	REMARKS
boat in	600	nitrogen: 6.0	5	
stabilize	600	nitrogen: 6.0	10	
anneal	600	nitrogen: 6.0	15	
heat up	+10 °C/min	nitrogen: 3.0 oxy- gen: 0.3	40	
stabilize	1000	nitrogen: 3.0 oxy- gen: 0.3	2	
oxidation	1000	nitrogen: 2.25 oxy- gen: 3.85	42	Target 300nm oxide
cool down	-7 °C/min	nitrogen: 2.25 oxy- gen: 3.85	60	
boat out	600	nitrogen: 3.0	5	

A.2.2. MEASUREMENT: OXIDE THICKNESS

Use the Woollam measurement system to measure the oxide thickness:
Oxide thickness: 300 nm on the process wafers

A.3. METALLIZATION

A.3.1. COATING AND BAKING

Use the EVG 120 wafertrack to coat the wafers with resist, and follow the instructions specified for this equipment.

The process consists of a treatment with HMDS (hexamethyldisilazane) vapor with nitrogen as a carrier gas, spin coating with AZ NLOF2020 negative photoresist, and a soft bake at 95degC for 90 seconds.

Always check the temperature of the hotplate and the relative humidity (48 ± 2 %) in the room first.

Use coating **Co-nlof2020-3,5um-no EBR** (resist thickness: 3.500 μm).

A.3.2. ALIGNMENT AND EXPOSURE

Processing will be performed on the Suss MA/BA8 and follow the operating instructions from the manual when using this machine.

Mask: metal contacts (glass mask) Exposure time: check logbook (88 mJ equivalent)

A.3.3. DEVELOPMENT

Use the EVG 120 wafertrack to develop the wafers, and follow the instructions specified for this equipment.

The process consists of a post-exposure bake at 115 degC for 90 seconds, followed by a development step using Shipley MF322 developer (double puddle process), and a hard bake at 100 degC for 90 seconds.

Always check the temperature of the hotplates first.

Use development program **Only-X-link Bake**
Use development program **xDens-Dev-Lift-Off**

A.3.4. INSPECTION

Visually inspect the wafers through a microscope, and check openings.

A.3.5. Cr/Au evaporation

Use the CHA evaporator in CR10000 to deposit 10/100 nm of Cr/Au. **Contaminated after this step so use boxes for Au-contaminated wafers.**

A.3.6. LIFT-OFF

Perform lift-off in SAL using NI555 heated bain-marie to 50°C in an ultrasonic bath. Apply ultrasonic till all Au is removed from the areas it should be lifted off. Rinse in DI water for 5 min and dry the wafers using the contaminated chuck.

Use dedicated beakers for contaminated samples

A.3.7. INSPECTION

Visually inspect the wafers through a microscope, and check openings. Put a tissue underneath the wafer.

B

XRD Calculation

B.1. Samples annealed at 450°C

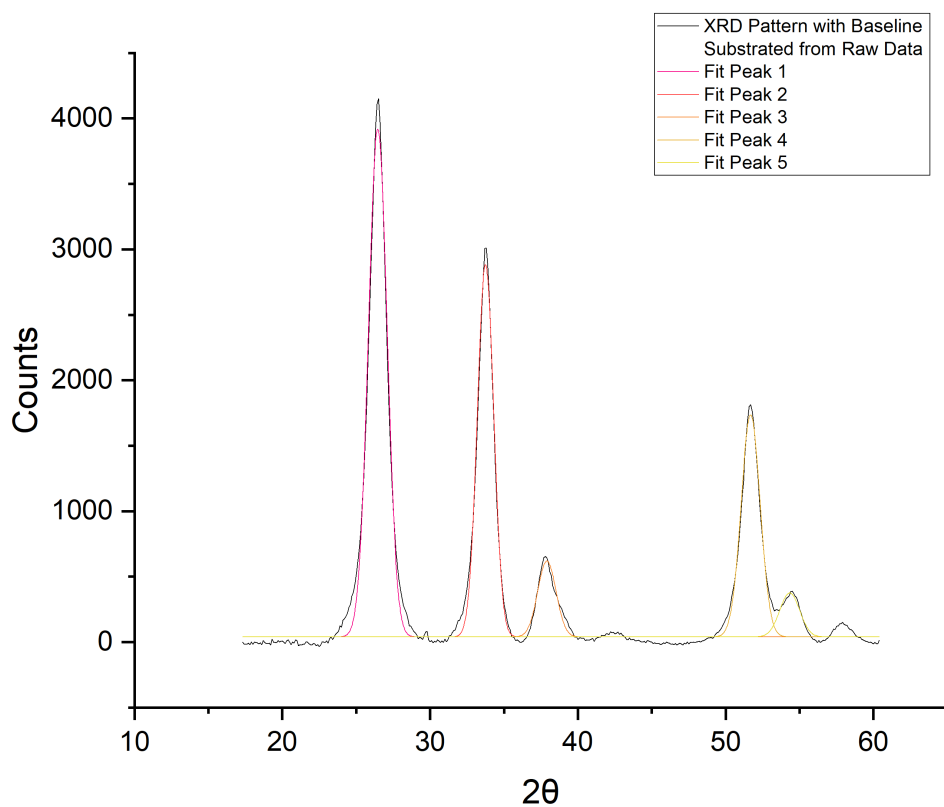
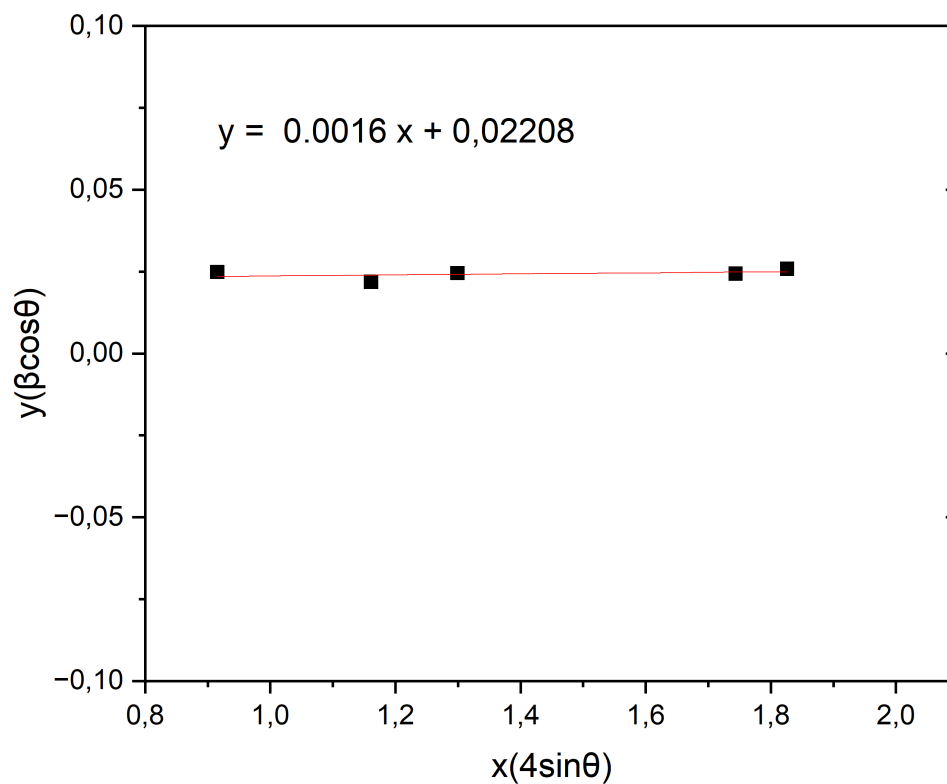


Figure B.1: XRD Pattern with Multiple Peak Fit

Table B.1: T450

S.No	$2\theta/\text{degree}$	$\text{FWHM}(\beta_T)/\text{degree}$	$\beta \cos\theta$	$4\sin\theta$
1	26.45271	1.46383	0.024870944	0.915194697
2	33.74357	1.30871	0.021858132	1.160923923
3	37.8991	1.48709	0.024548003	1.298941927
4	51.68958	1.55283	0.024391207	1.743739101
5	54.32652	1.66256	0.025816825	1.826110037

**Figure B.2:** Linear Fitting Result

According to the Williamson-Hall equation:

$$\beta_T \cos \theta = \xi(4 \sin \theta) + \frac{K\lambda}{D} \quad (3.5)$$

$$D = 6.977\text{nm}$$

B.2. Samples annealed at 600°C

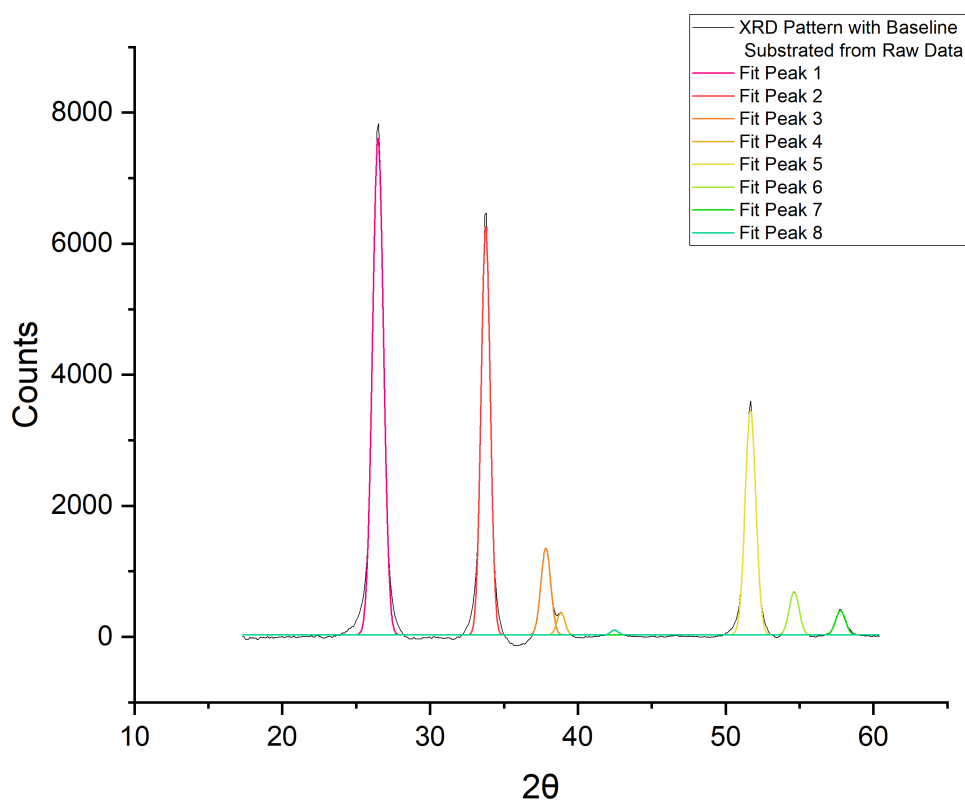


Figure B.3: XRD Pattern with Multiple Peak Fit

Table B.2: T600

S.No	$2\theta/\text{degree}$	$\text{FWHM}(\beta_T)/\text{degree}$	$\beta \cos\theta$	$4\sin\theta$
1	26.46527	0.86382	0.014676202	0.915621488
2	33.75267	0.71733	0.011980589	1.161227896
3	37.83162	0.76943	0.012703862	1.296713862
4	38.85365	0.63666	0.010479185	1.330410791
5	51.68282	0.8548	0.013427226	1.743526731
6	54.6323	0.78981	0.012247615	1.835600046
7	57.76922	0.78458	0.011989954	1.932188843
8	42.47715	0.59986	0.009758443	1.44900874

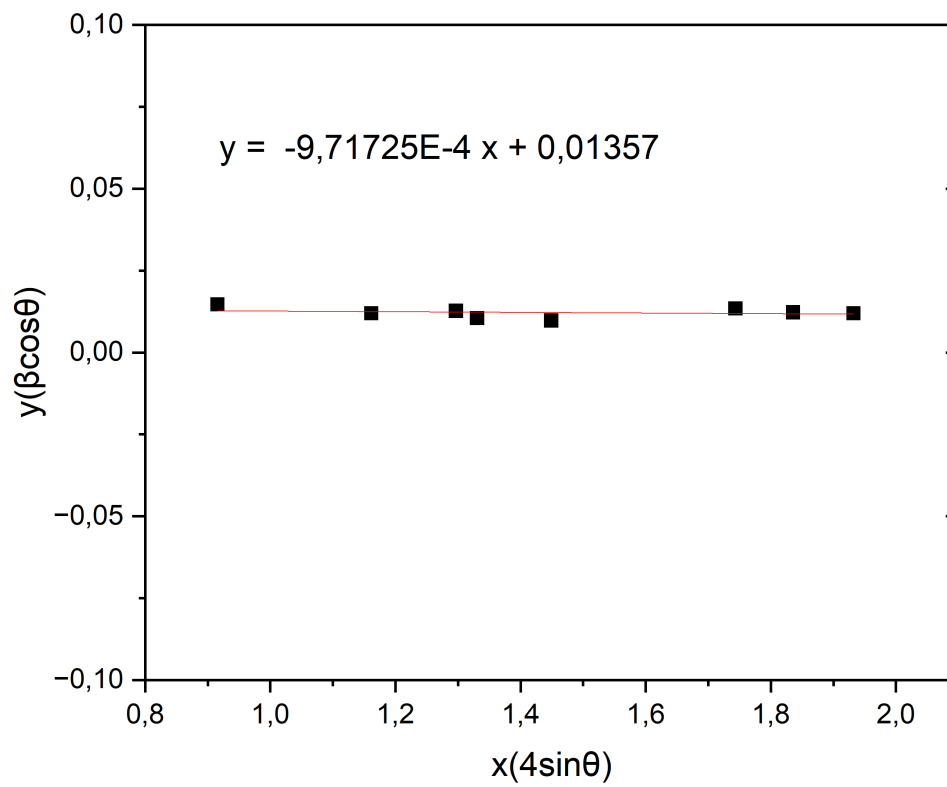


Figure B.4: Linear Fitting Result

According to the Williamson-Hall equation:

$$\beta_T \cos \theta = \xi(4 \sin \theta) + \frac{K\lambda}{D} \quad (3.5)$$

$$D = 11.353nm$$

C

V-I Graph

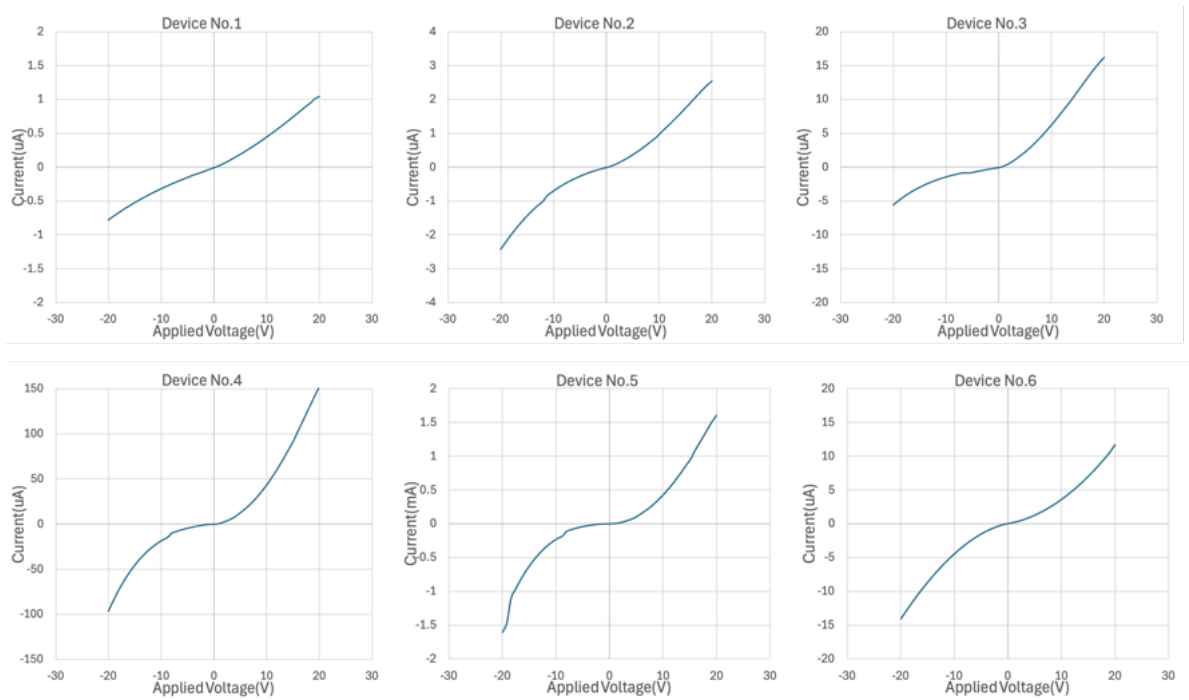


Figure C.1: V-I relation of the device before annealing at 450°C

Appendix C. V-I Graph

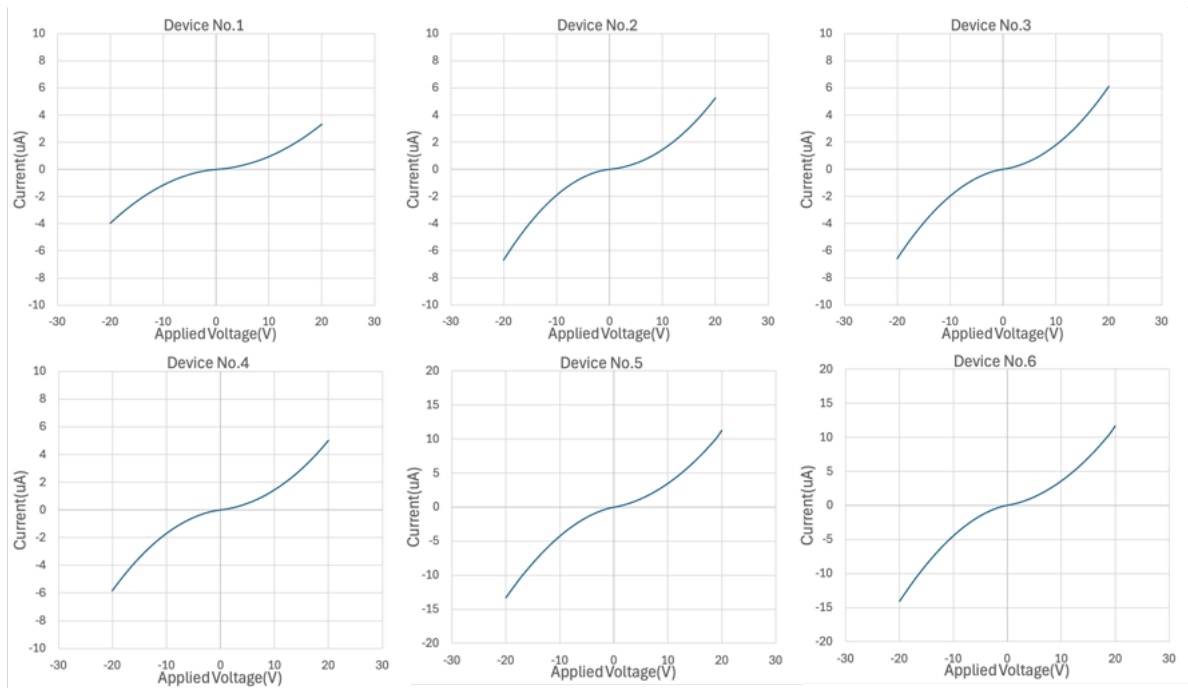


Figure C.2: V-I relation of the device annealed at 450°C

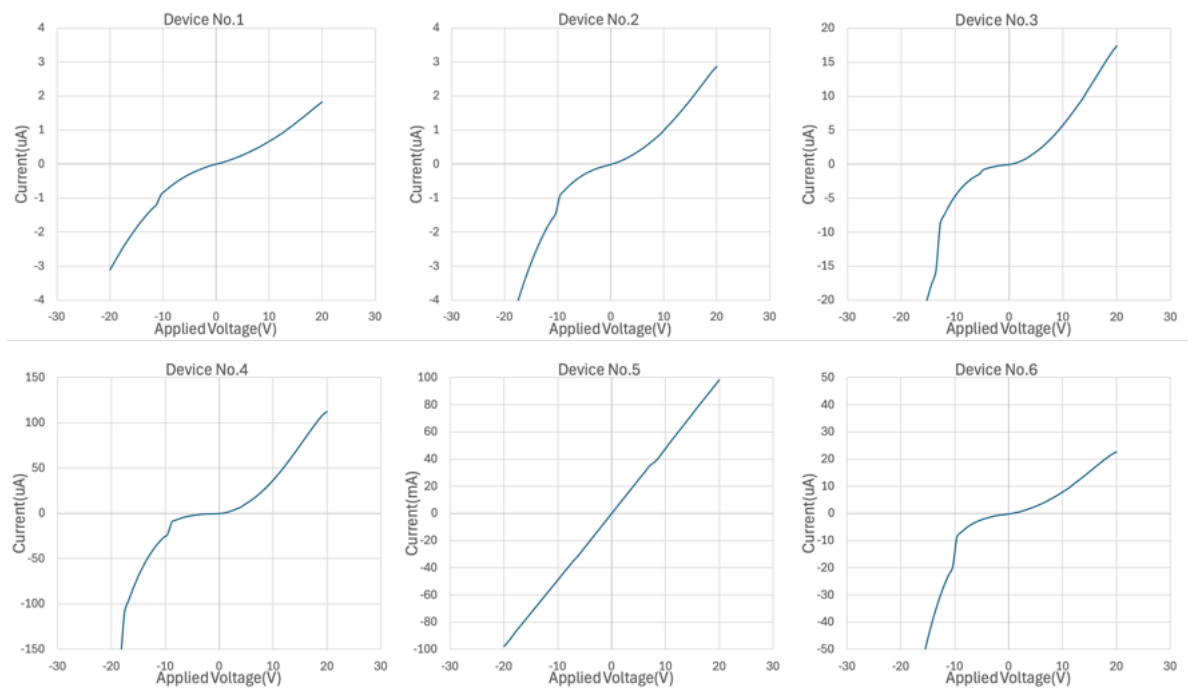


Figure C.3: V-I relation of the device annealed at 600°C

Appendix C. V-I Graph

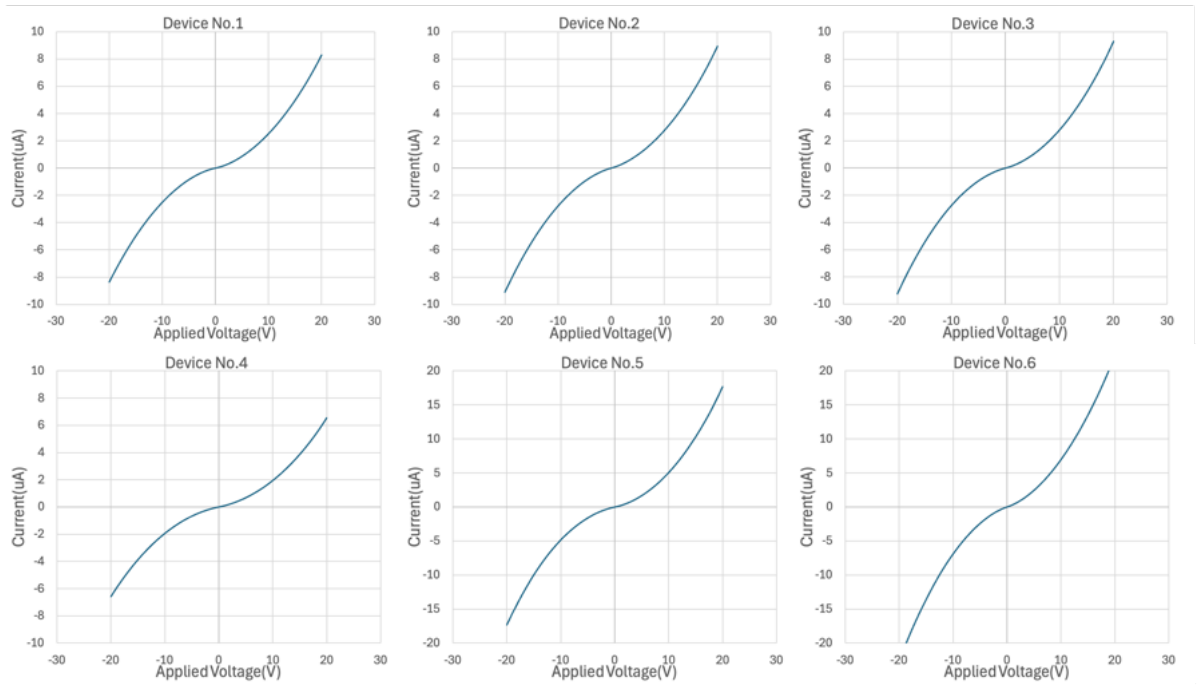


Figure C.4: V-I relation of the device annealed at 600°C

D

Gas Sensing Graphs

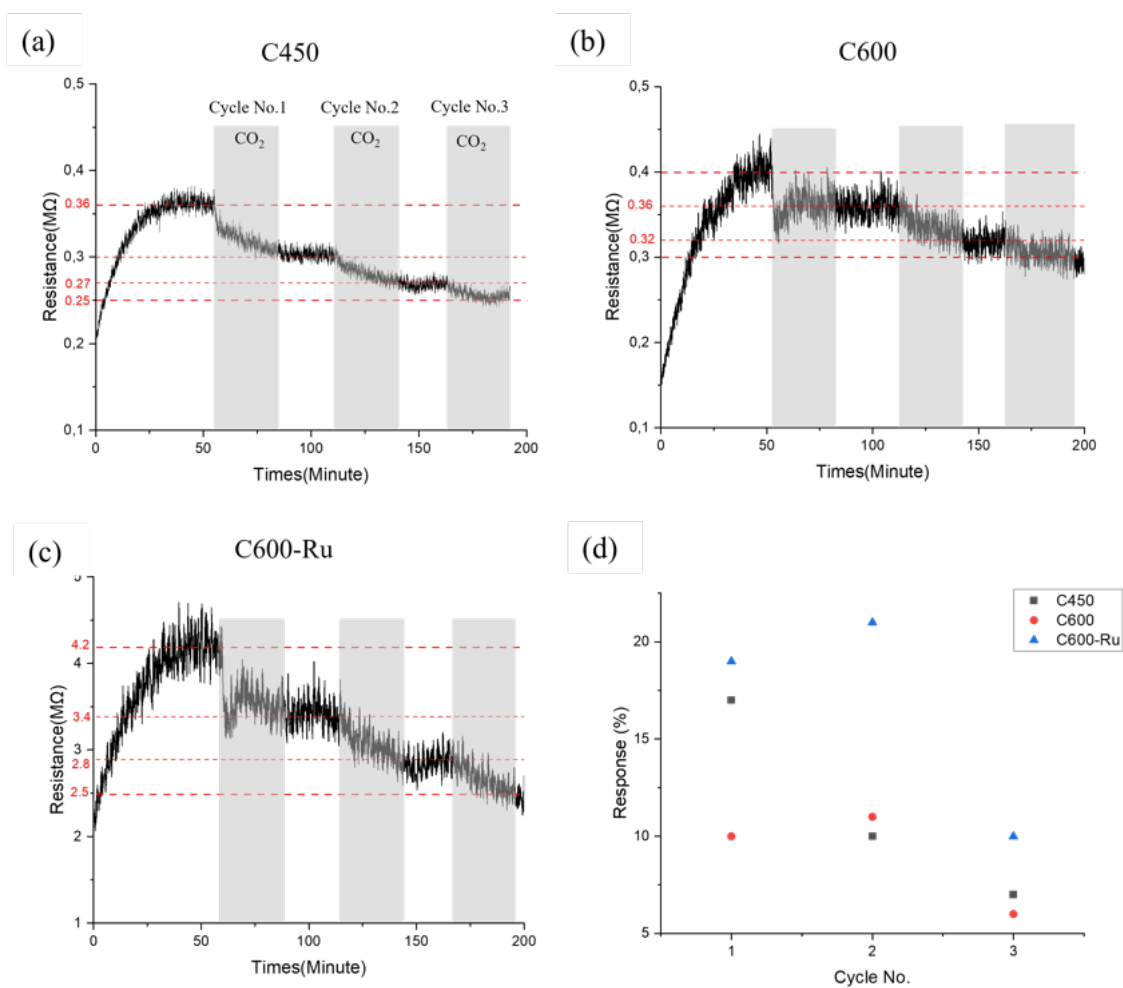


Figure D.1: Response to CO₂ in N₂ atmosphere, Device No.5 (a) C450 (b) C600 (c) C600-Ru (d) Calculated response of these samples

Appendix D. Gas Sensing Graphs

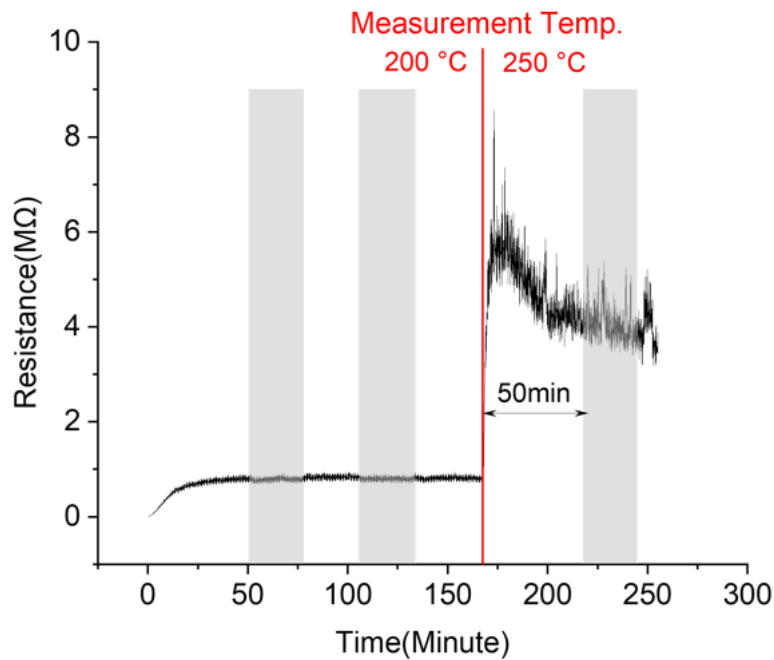


Figure D.2: Sudden increase in noise After high-temperature transition, C450, Device No.2

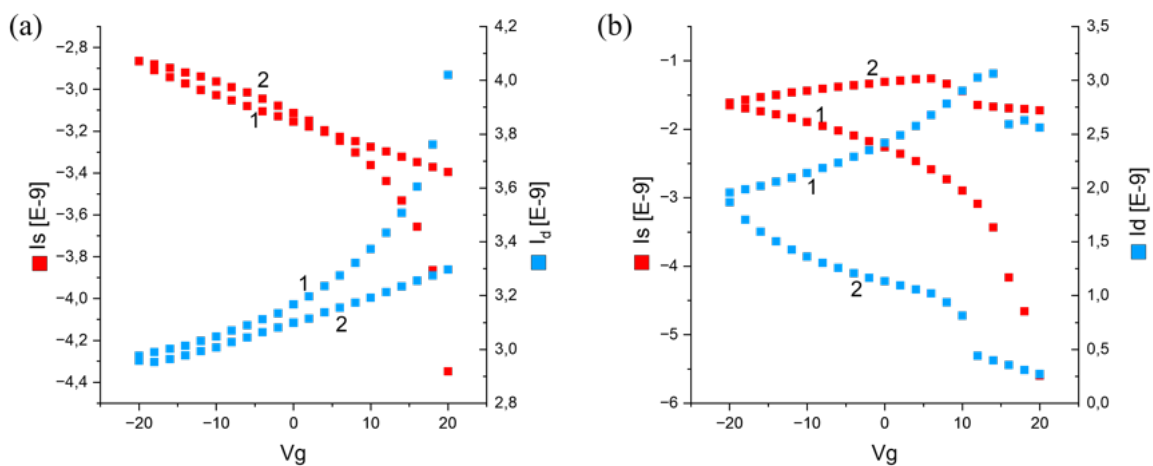


Figure D.3: Gate Voltage Dependence of Source and Drain Currents (a) Case1 (b) Case2 with Hysteresis Effect

Raman scattering is an important characterization method in materials science. It can probe the vibrational efficiency of functional groups, and provide insights into material structure, surface characteristics, and even oxygen vacancies. For nanoscale SnO_2 , vibrational modes can be classified into two categories: intrinsic vibrational modes and those induced by the small grain size effect.

Fig D.4a shows the Raman spectra of C600. The peak around 520 cm^{-1} corresponds to crystalline silicon (c-Si), which is attributed to the substrate, as the sample was deposited on a

Appendix D. Gas Sensing Graphs

single-crystal silicon wafer. Fig D.4b shows the results of Raman scattering of different samples. From this graph, the characteristic peaks at 434 cm^{-1} (E_g) and 618 cm^{-1} (A_{1g}) are observed, which belong to Group A. According to the previous study[77], the vibration mode of group B can be observed at 571 cm^{-1} . However, due to the overwhelming intensity of the Si peak at 520 cm^{-1} , the SnO_2 signal in this region cannot be observed in the spectra.

As reported in [78], the two weak Raman bands observed at 301 cm^{-1} and 670 cm^{-1} are likely associated with the IR-active $E_u(3)$ TO and A_{2u} LO modes, respectively. To verify this, bulk SnO_2 should be characterized and compared. If the Raman spectra of the bulk SnO_2 do not exhibit these two peaks, it would confirm that these peaks are not intrinsic to the bulk material but are instead related to surface effects, defects, or nanoscale phenomena specific to the sample under study.

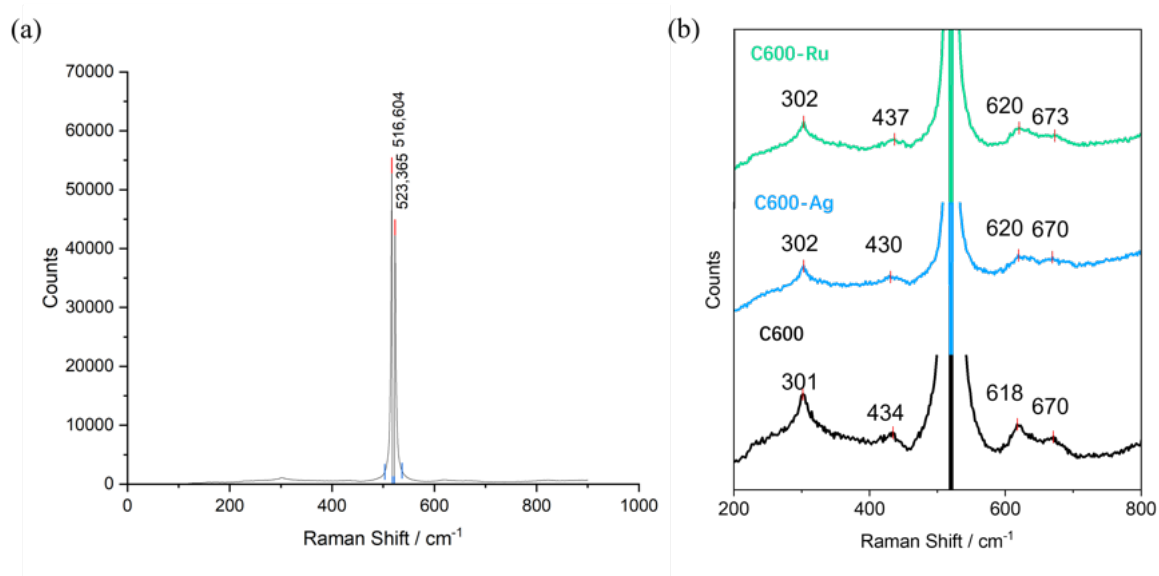


Figure D.4: Raman spectra of pure and Ag, Ru decorated SnO_2 sensing layers